

NORTHWESTERN UNIVERSITY

Development and Applications of a Computational Method for Analyzing Biological
Tubes and Cells

A DISSERTATION

SUBMITTED TO THE GRADUATE SCHOOL
IN PARTIAL FULFILLMENT OF THE REQUIREMENTS

for the degree

DOCTOR OF PHILOSOPHY

Field of Interdepartmental Biological Sciences

By

Ran Yang

EVANSTON, ILLINOIS

September 2019

Abstract

Biological tubes are essential for animal survival, and their functions are highly dependent on tube shape. Analyzing the contributions of cell shape and organization to the morphogenesis of small tubes has been hampered by the limitations of existing programs in quantifying cell geometry on highly curved tubular surfaces and calculating tube-specific parameters. I developed a computational tool called QuBiT (Quantitative Tool for Biological Tubes) and used it to analyze morphogenesis during embryonic *Drosophila* trachea development. Analysis in wildtype tracheal dorsal trunks (DT) found previously unknown anterior-to-posterior gradients of cell orientation and aspect ratio as well as periodicity in the organization of cells in the main tube. Furthermore, computational modeling of tracheal expansion suggests that cell intercalation and/or rearrangement occurs but is not necessary to maintain the integrity of the DT. Analysis of tracheal mutants revealed unexpected findings, including interactions between Src42 and FoxO, Uif, and the Na⁺/K⁺ ATPase, suggesting that Src42 is a central regulator of tube size. These results demonstrate the importance of a computational tool for analyzing the morphogenesis of small diameter biological tubes and are a great asset to elucidating the biomolecular and biophysical mechanisms of tube size regulation.

Acknowledgements

I would like to thank my advisor, Dr. Greg Beitel, for his encouragement, patience, and guidance; for his positivity and never giving up; and simply for giving me a chance.

I would like to thank Lily, for pushing me, challenging me, and helping me grow as a person.

Finally, I want to thank my parents and my sister for their unconditional support.

Table of Contents

Abstract	2
Acknowledgements	3
Chapter 1: Introduction	7
The origins and mechanistic diversity of tube formation	11
A closer look: Development of the fly trachea	17
Computational modeling to better understand tube development	25
Chapter 2: Development and Functions of QuBiT	29
Overview	30
Collection of image stack data	32
Surface mapping and defining tube centerlines	32
Cell mapping	33
Tube unrolling	36
3D modeling	38
Methods of data analysis	40
Chapter 3: Insights in wildtype tracheae	42
Overview	43
DT tube and cell parameters exhibit anterior-posterior gradients	44
Many dorsal trunk cell properties have an anterior-to-posterior gradient	45
DT cell properties have segmentally repeating variations	48

	5
A simple cell expansion model suggests cell rearrangement during DT expansion	.50
The distribution of dorsal trunk cell connectivity does not change during tube expansion.....	54
The distribution of dorsal trunk cell connectivity is not impacted by side branches	.56
The number of cells per cross-section changes during tube expansion.....	58
Tube unrolling reveals unexpected patterns of Uif localization.....	61
Chapter 4: Src42 and dDAAM mutants impact tube structure and cell geometry	64
Introduction to Src42	65
Src42 acts in conjunction with other systems to regulate cell orientation.....	66
Analysis of early stage tracheae in Src42 mutants shows unusual cell apical surface profiles	71
Introduction to dDAAM	74
dDAAM likely functions in parallel to Src42.....	75
The lumen disconnects from the apical surface in posterior dDAAM tubes.....	79
Chapter 5: Src42 as a central regulator: FoxO and the Na ⁺ /K ⁺ ATPase.....	82
Introduction to FoxO	83
FoxO controls tube length but not cell parameters	84
FoxO functions downstream of Src42 to regulate growth	87
Introduction to the Na ⁺ /K ⁺ ATPase.....	90
The ATP α mutant disrupts localization of the apical marker Uif.....	91
Nrv2 tubes appear equally convoluted as ATP α tubes, but are much shorter.....	94

	6
Analysis of cells in the Nrv2,Src42 double mutant suggests Src42 is upstream of Nrv2	97
Chapter 6: Discussion.....	100
Fusion cells restrict cell geometries and tube shape	101
Uif is an apical component whose localization also relies on D-V patterning.....	101
Apical cell surfaces are transiently reshaped due to the flow of the aECM / Tube expansion correlates with cell rearrangement.....	104
Src42 as a central regulator of tube size.....	106
Significance and future directions.....	108
References.....	111
Appendix.....	124
Validation of QuBiT functions and methods in other tubular systems: the hindgut and salivary gland	124
Cell structures in the DT are similar to those seen in known cell rearrangement paradigms	127
Preliminary analyses of Crumbs in tube size control.....	128
Laser ablation experiments suggest the trachea is under tension during early development, but not as the tube grows	134

Table of Figures

Fig. 1.1: Origins of tube formation in mammals.	12
Fig. 1.2: Development of the zebrafish gut.	14
Fig. 1.3: Overview of fly salivary gland development.....	15
Fig. 1.4: Overview of trachea development.	19
Fig. 1.5: Specification and formation of branches in the trachea.	19
Fig. 1.6: Physical forces shape the DT.	22
Fig. 1.7: Epithelial polarity proteins are one of many components of tracheal size control	23
Fig. 2.1: Visual representation of the workflow QuBiT.	31
Fig. 2.2: Sample segmentation of tracheal tubes using Ilastik.....	34
Fig. 2.3: Sample output of the segmented tube and calculated centerline in 3D.....	34
Fig. 2.4: Cell plotting.	35
Fig. 2.5: Tube unrolling algorithm.	37
Fig. 2.6: Sample output of tube unrolling after watershedding.	38
Fig. 2.7: Schematic of 3D modeling in QuBiT.....	40
Fig. 3.1: w^{1118} tube and cell measurements.....	46
Fig. 3.2: Tenectin mutants have bulgy tracheal segments.....	51
Fig. 3.3: The theory of a simple tube expansion model.	51

Fig. 3.4: Tube expansion occurs through computational unrolling and rerolling.....52

Fig. 3.5: Expansion of wildtype tubes.....53

Fig. 3.6: Theory of connectivity and cells per cross-section (CPC) as indicators of rearrangement.....55

Fig. 3.7: Cell connectivity distributions for w^{1118}57

Fig. 3.8: Cells per cross-section (CPC) for w^{1118}60

Fig. 3.9: Representative unrolled tube data for w^{1118}63

Fig. 4.1: Src42 tube and cell measurements.....67

Fig. 4.2: Src42 mutants disrupt Uif.....69

Fig. 4.3: Representative unrolled tube data for Src42[26-1].....70

Fig. 4.4: Src42 tube and cell measurements at stages 14 and 16.....73

Fig. 4.5: dDAAM tube and cell measurements.....77

Fig. 4.6: Representative unrolled tube data for dDAAM mutant alleles.79

Fig. 4.7: The lumen dissociates from the apical surface in posterior of dDAAM mutants.....81

Fig. 5.1: FoxO tube and cell measurements.....85

Fig. 5.2: Representative unrolled tube data for FoxO.....86

Fig. 5.3: FoxO,Src42 double mutant tube and cell measurements.88

Fig. 5.4: Representative unrolled tube data for FoxO/Src42.89

Fig. 5.5: ATP α tube data.....	92
Fig. 5.6: Representative unrolled tube data for ATP α [LNFS].	93
Fig. 5.7: Nrv2 tube data.....	95
Fig. 5.8: Representative unrolled tube data for Nrv2[2.1].....	96
Fig. 5.9: Nrv2,Src42 tube measurements.....	98
Fig. 5.10: Preliminary Nrv2,Src42 cell measurements.....	99
Fig. 6.1: Schematic of Uif banding in the DT.....	103
Fig. 6.2: Concept: Various arrangements of a set of building blocks can result in the same macroscopic structure.....	106
Fig. 6.3: Molecular pathways and mechanisms of tube size control.....	107
Fig. A.1: Processing of other tubes in the fly embryo.....	126
Fig. A.2: Voronoi diagram of a w ¹¹¹⁸ unrolled embryo.....	128
Fig. A.3: A basic overview of Crb and its potential target, the Hippo network, for regulating tube size.....	130
Fig. A.4: Mislocalization of Crb in the shrub mutant causes tube elongation.	131
Fig. A.5: Crb constructs and tube length measurements.	132
Fig. A.6: Crb tube cross-section measurements.	133
Fig. A.7: Laser ablation of wildtype trachea suggests the DT is under tension early in development.	135

Chapter 1: Introduction

Though they may simply seem like hollow cylinders at first glance, tubes and tube-like structures are designed, created, and maintained through many complex interactions in order to achieve the correct shapes and sizes and to perform specific functions. We rely on both man-made and naturally occurring tubes for our daily needs, from water and gas delivery to our homes to nutrient and waste exchange in our lungs. The marked difference in the architectures of these tubes is no coincidence. For example, the pipes delivering our drinking water must not be permeable to water, whereas the alveoli and capillaries in our bodies must allow the exchange of gases and nutrients with neighboring tissues. Our water lines must be wide enough to allow transport of large volumes of water, whereas alveoli and capillaries are narrow tubes designed to maximize surface area and thus the efficiency of nutrient and waste exchange.

While industrial-grade pipes can generally be made to order by using different materials such as polyethylene or galvanized metals, or molds of various sizes, the molecular machinery that specifies and produces biological tubes is more complex and nebulous. These naturally occurring networks have a wide range of parameters including size, shape, and connectivity that must be reproducible in each individual of an entire species.

Biological tubes that do not achieve or maintain the correct dimensions or network structures can have fatal consequence, such as polycystic kidney disease, where genetic mutations in polycystin-1, a cell cycle and calcium ion channel regulator (Hughes et al., 1995; Torres et al., 2007), causes renal tubules to dilate and form cysts. In addition to genetic predispositions to misregulated tubes, physical obstructions can have just as severe of an impact, such as in atherosclerosis, where plaque buildup in arteries increases blood pressure and limits delivery of oxygen and other nutrients to downstream sites. Improving our understanding of the molecular mechanisms of biological tube development and maintenance will undoubtedly help in risk assessment, diagnosis, treatment and prevention of these diseases.

The origins and mechanistic diversity of tube formation

Studies on biological tubes originated in neural tube formation in chicks, and a simplified overview is shown in Fig. 1.1. A distinct series of mechanisms is required for proper neural tube formation; misregulation of this important developmental event can result in devastating diseases such as spina bifida. In chick, the established neural plate cells undergo shape changes from cuboidal to more columnar cells (Keller et al., 1992). Cells at opposite ends of the plate, called the neural folds, push together, causing the

prospective neural tube to fold inward, aided by molecular signaling between the neural plate and notochord (Smith and Schoenwolf, 1989). The neural folds continue to migrate until the ends meet and the prospective neural epithelium and non-neural epithelium each close. Though the mechanisms of neural tube closure are the least understood, the end result is a morphological change: a planar cell sheet becomes a closed tube. However, later studies of tube formation in other organisms show that the aforementioned series of mechanisms cannot be generalized.

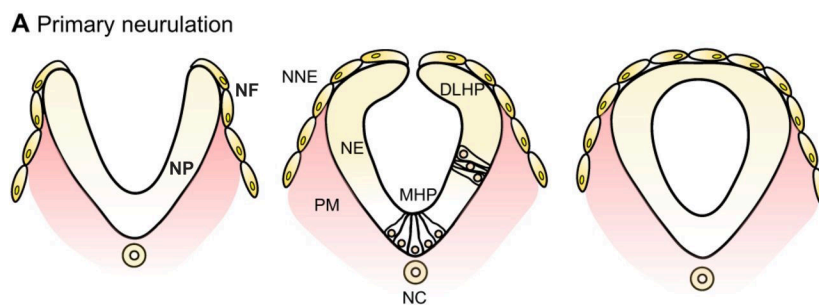


Fig. 1.1: Origins of tube formation in mammals. A simplified scheme of neural tube closure in mammals such as chick and mouse. Many distinct and complex mechanisms are required, including cell migration, cell shape changes, establishment of polarity, and closure of epithelial tissue. Relevant abbreviations: NF, neural fold; NP, neural plate; NNE, non-neural epithelium; NE, neural epithelium; NC, notochord. Adapted from (Nikolopoulou et al., 2017).

A more recent understanding of both the chemical signals and mechanical forces required to form a tube is demonstrated in *de novo* zebrafish gut formation (Navis and Bagnat, 2015). Misregulated gut development can result in a series of nonfunctional, disjointed lumens, speaking to the importance of consistent and proper regulation. As shown in Fig. 1.2, initially disordered gut cells secrete fluid-filled sacs that merge to form the lumen through the disappearance of apical cell junctions, implying a series of mechanisms distinct from neural tube formation such as a delayed establishment of polarity, apical cell contact remodeling on the tube circumference, and luminal expansion and fusion. The molecular signals in the zebrafish gut are also distinct from generic neural tube closure in vertebrates. For example, while Rab11 has been shown to be essential for PCP-mediated apical constriction in neural tube closure (Ossipova et al., 2014), Rab11 in zebrafish has a wide-spread apical distribution and is instead necessary for fusion of disjointed lumens (Alvers et al., 2014).

It is evident that a combination of chemical signals and mechanical forces drives tube development, but even within a single organism, the methods of tube formation can vary greatly. The model organism used in this project, *Drosophila melanogaster*, is also well-studied with several distinct tube control mechanisms in, for example, the salivary gland, hindgut, and trachea.

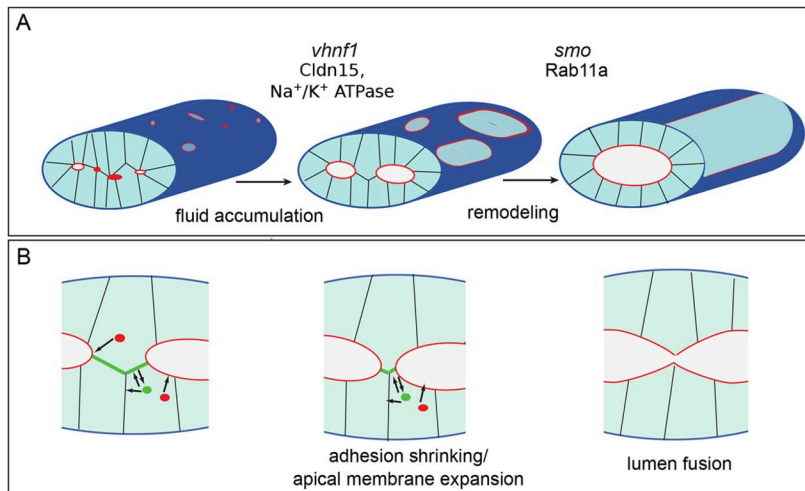


Fig. 1.2: Development of the zebrafish gut. Initially disordered cells establish apical/basal polarity and secrete fluid-filled sacs that fuse through cell junction shrinking in order to form the mature gut. Adapted from (Alvers et al., 2014).

The fly salivary gland (SG) is a relatively short and simple tube structure with no branching and only two distinct cell types. An overview of its development is shown in Fig. 1.3. Salivary gland development begins when Sex combs reduced (*Scr*) specifies the apical expansion through *Crumbs* and *klarscht* (*klar*) signaling (Myat and Andrew, 2002), before the gland realigns to muscle cells of the body wall, which requires further apical elongation, cell shape changes, and cell rearrangement (Blake et al., 1999). At the same

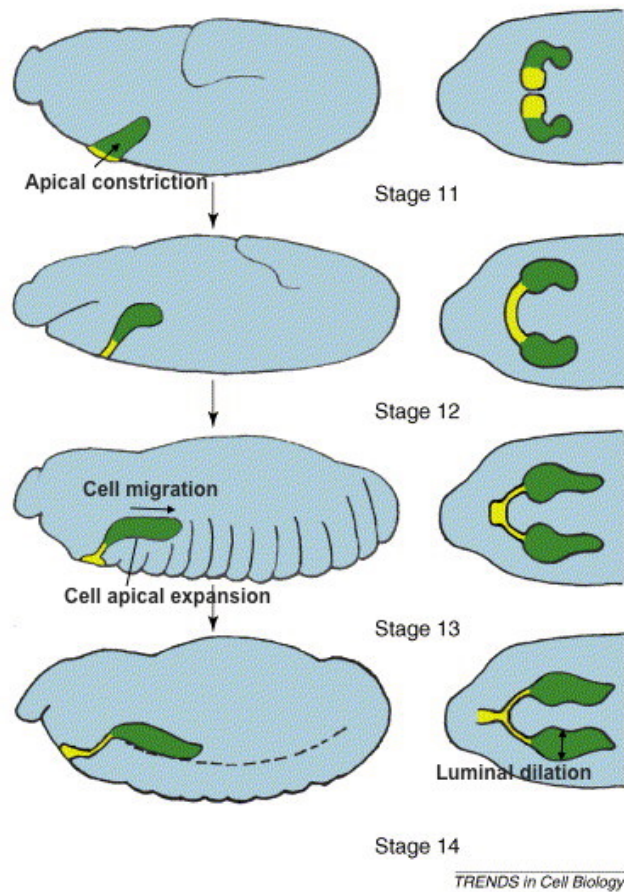


Fig. 1.3: Overview of fly salivary gland development depicting several key mechanisms of tube formation. Stage 11: Apical constriction signals the start of tube formation. Stages 12-14: Apical expansion elongates the tube in the secretory cell region (green) while cell migration carries secretory cells to the correct location and the tube dilates to the correct size. Adapted from (Abrams et al., 2013).

time, expansion of the SG lumen is controlled by Pak1-regulated apicobasal E-cad levels (Pirraglia et al., 2010) and Rho GTPase-regulated apicobasal actin distribution and polymerization (Xu et al., 2011).

The fly hindgut develops similarly to the SG, but with some distinct differences. Like the SG, the hindgut primordium invaginates by apical constriction, which is driven by GPCR-mediated actomyosin contraction (Costa et al., 1994; Morize et al., 1998). However, unlike in the SG, cell shapes in the hindgut change from columnar to cuboidal and squamous in the large and small intestine respectively, implying the importance of this distinction, though extent of impact of cell shape mutants such as *raw*, *ribbon* (Blake et al., 1998), *lines*, and *drumstick* (Iwaki et al., 2001) is uncertain. Elongation of the hindgut is driven by cell rearrangement (Iwaki et al., 2001; Singer et al., 1996) rather than simple apical expansion of the secretory cells in the SG. While cell rearrangement is known to be regulated by PCP/Wnt11 in vertebrates including zebrafish (Heisenberg et al., 2000), chick (Ouko et al., 2004), mice (Sinha et al., 2015), and human (Gao et al., 2017), the importance and mechanisms of cell rearrangement in the fly hindgut are less clear (Iwaki et al., 2001). Nevertheless, the fly SG and hindgut (and trachea, which will be described below) are tubular structures that demonstrate the nuances of tube development even within a single organism.

A closer look: Development of the fly trachea

While few studies have attempted to understand tube development in the SG and hindgut, the fly trachea has been the subject of greater investigation in tube size control and is the model used in this study. While a lot is known about the chemical and physical mechanisms that regulate tracheal development, our knowledge is far from complete. A brief diagram depicting key stages of tracheal development is shown in Fig. 1.4. The tracheal system is the gas exchange organ of the fly and thus functions as a lung, but in branch structure it more resembles a vascular system because it is a ramifying network that directly delivers oxygen to specific tissues. Tracheal tubes are epithelial monolayers approximately the size of small capillaries or kidney tubules in mammals, but there are no associated muscle cells, pericytes, or other accessory cells that are known to contribute to tracheal tube size control. Thus, tracheal tube size directly results from interactions of the tracheal cells with each other and with a secreted apical extracellular matrix (aECM) that transiently fills the tube lumens as they expand during their initial development.

The tracheal primordia in each embryo begin as 10 distinct pairs of placodes (Campos-Ortega and Hartenstein, 1997) (Fig. 4a) which are specified by the transcription factor

Trachealess (Trh), a “master” regulator of downstream tracheal genes (Isaac and Andrew, 1996; Wilk et al., 1996). A wave of EGFR establishes planar cell polarity in the placodes towards the invagination site and stimulates the formation of supracellular myosin cables at the tracheal pits (Nishimura et al., 2007). In a parallel pathway, subapical accumulation of Crumbs contributes to apical constriction by recruiting moesin (Moe) and organizing the actomyosin complex (Letizia et al., 2011). The mechanical forces of the actomyosin network on the tracheal placodes, which have been weakened due to cell rounding during the single round of mitosis at the beginning of invagination, leads to a rapid cascade of tracheal cells internalizing into the sac-like tracheal primordia (Kondo and Hayashi, 2013).

The cells in each primordium then migrate to form branches in response to various signals (Fig. 1.4b and 1.5). The tip cells that will eventually lead branch migration are initially selected from each primordium through Delta/Notch inhibition (Chihara and Hayashi, 2000; Llimargas, 2000) The extension of each branch is then regulated through FGF gradients: the branch cells express the receptor, *breathless (btl)*, while the target tissues such as the dorsal epidermis and intestine express the FGF ligand, *branchless (bnl)* (Du et al., 2017; Ohshiro et al., 2002; Sutherland et al., 1996) While many cells in

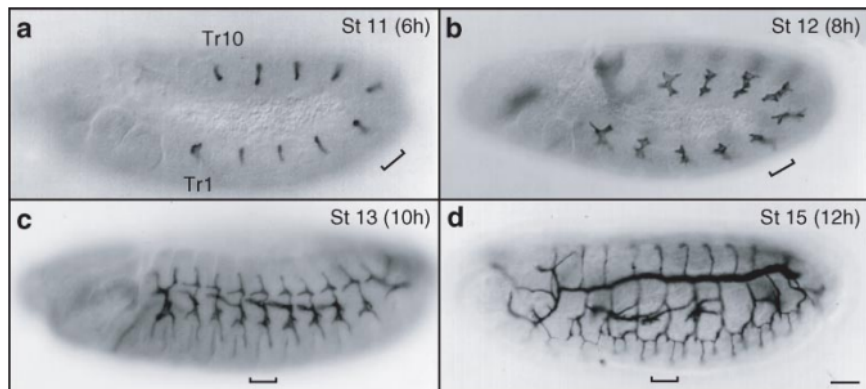


Fig. 1.4: Overview of trachea development. A robust set of morphogenetic events turns the 10 individual tracheal placodes (a) into a series of branched networks (b-c) that join together to form the full trachea (d). Adapted from (Ghabrial et al., 2003).

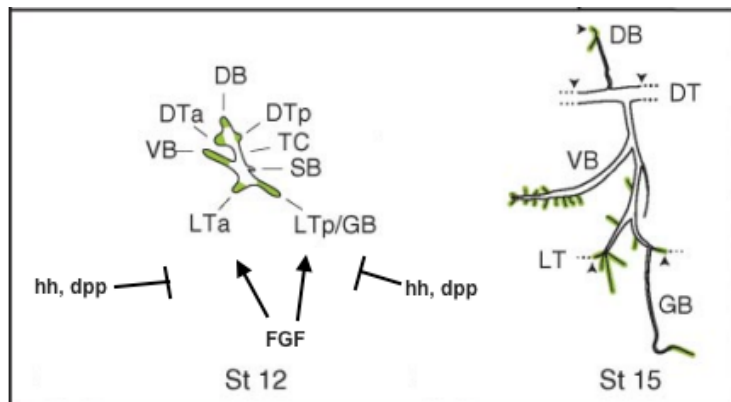


Fig. 1.5: Specification and formation of branches in the fly trachea. These events occur independently in each primordium before the DT segments fuse to form a continuous tube. Branch outgrowth is regulated by FGF and its downstream components while lateral inhibitors such as hedgehog and dpp gradients limit growth to each thoracic segment. Adapted from Ghabrial et al., 2003.

each branch express FGFR, only the tip cells respond to the migratory cue; the remainder of the stalk follows the tip rather than the FGF gradient (Ghabrial and Krasnow, 2006; Lebreton and Casanova, 2014). At the same time, stripes of hedgehog signaling and gradients of dpp are used to limit branch migration within each thoracic and abdominal segment, ensuring the correct arrangement of branches (Kato et al., 2004).

The tip cells of the anterior and posterior dorsal trunk (DT) branches have a unique problem to solve: they must join with neighboring DT branches in order to form a continuous DT tube. Within these tip cells, Wingless (wg) specifies the fusion cell fate (Miao and Hayashi, 2016), which plays an important role in ensuring the continuity of the DT. Following tip cell migration, the adhesion of fusion cells from adjacent tracheal segments is driven by E-cad (Samakovlis et al., 1996; Tanaka-Matakatsu et al., 1996). The DT lumen at fusion points is then created by secretion of Golgi vesicles at the cell-cell interface (Kato et al., 2016) while ARF-like-3 GTPase-mediated fusion of plasma membranes creates the characteristic washer-like shape of fusion cells (Jiang and Crews, 2007; Kakiyama et al., 2008).

After tracheal segments connect, the tube expands and elongates using several parallel mechanisms (Fig. 1.4d and 1.6). First, secretion of chitinous matrix produced by chitin synthases *kkv* and *mummy* (Araujo et al., 2005; Devine et al., 2005; Tønning et al., 2005) is controlled by *sar1*, a small GTPase that regulates ER to Golgi trafficking (Tsarouhas et al., 2007). Chitin accumulation is thought to supply the mechanical force for tube expansion, while the responding accumulation of F-actin at the apical cell surfaces in rings orthogonal to the tube axis opposes the expansion force of the secreted chitin (Kondo et al., 2007; Matusek et al., 2006; Ozturk-Colak et al., 2016). Due to the viscoelastic nature of the aECM (Dong et al., 2014; Forster et al., 2010), these opposing forces can establish proper tube size. However, secretion of chitin alone isn't sufficient to address tube inflation. The expansion forces of the chitinous matrix must also coincide with apical expansion of cell membranes, and it is unclear whether expanding apical cell membranes contributes to additional chitin secretion or if expansion forces of increased chitin secretion cause cells to create more apical membrane.

Many studies on genetic mutations that impact tracheal size have focused on the dorsal trunk because it is easier to measure than the side branches and more is understood about the signaling pathways that contribute to its growth. The summation of a relatively large body of work has suggested that dorsal trunk length and diameter are

independently controlled, evidenced by mutations that impact either or both parameters. A subset of these results is shown in Fig. 1.7. Mutations that only affect length but not diameter include that of the ESCRT-III subunit Shrub/Vps32 (Dong et al., 2014) and epithelial polarity proteins Yurt and Scrib (Laprise et al., 2006), all of which cause mislocalization of the apical polarity protein Crumbs, an important but mechanistically poorly understood tube size control factor. In parallel, chitin

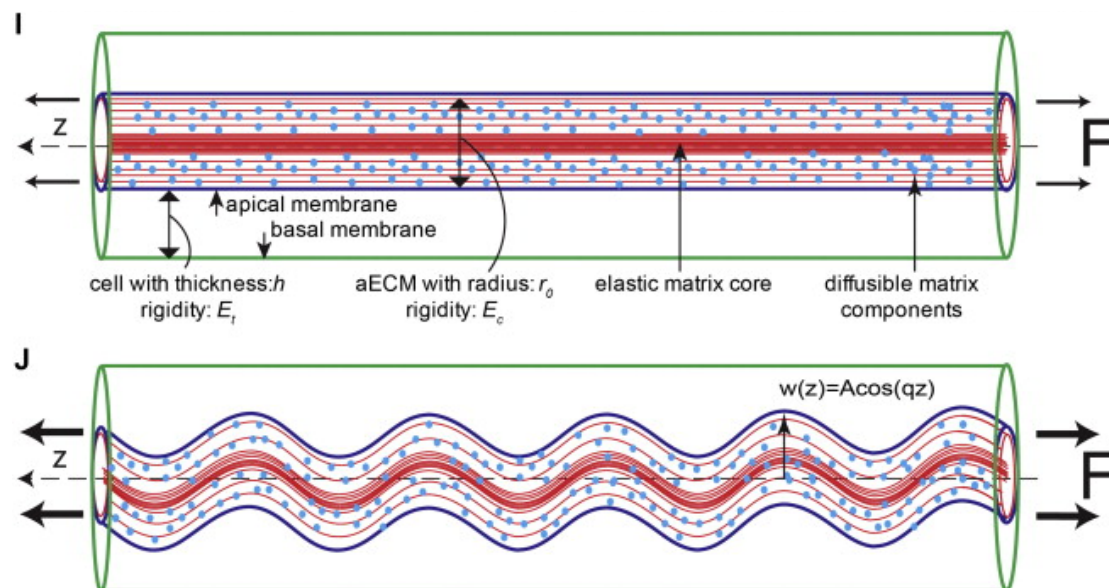


Fig. 1.6: Physical forces shape the DT. The elasticity of the chitinous ECM and expansion of the apical membrane supply opposing forces that result in the characteristic wavy tube. Adapted from (Dong et al., 2014).

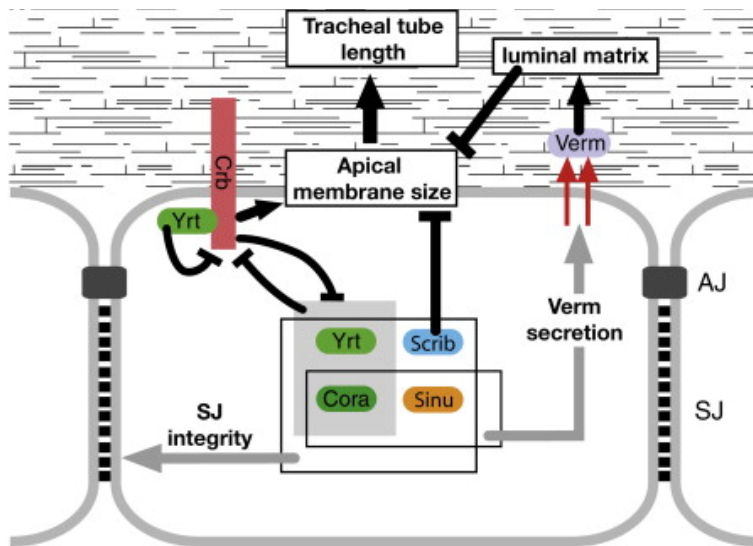


Fig. 1.7: Epithelial polarity proteins are one of many components of tracheal size control and can act through apical membrane expansion or matrix production. Adapted from Laprise et al., 2010.

deacetylases Serp and Verm restrict tube elongation (Luschnig et al., 2006; Wang et al., 2006), likely by changing the elasticity of the aECM by regulating the turnover of chitin to chitosan (Dong et al. 2014). A second group of mutations affect tube diameter but not length by disruption of chitin production (Araujo et al., 2005; Devine et al., 2005), organization (Moussian et al., 2005), or secretion through COPI (Grieder et al., 2008) and COPII (Forster et al., 2010; Norum et al., 2010) vesicles. Finally, previous studies have found septate junction mutations affect both tube length and diameter, independently of their other well-known function as paracellular barriers. These include claudins such as megatrachea (Behr et al., 2003), sinuous (Wu et al., 2004), and kune-kune (Nelson et al., 2010); Na⁺/K⁺ ATPase components Nrv2 and ATPa (Paul and Beitel,

2003); and other septate junction components such as coracle (Laprise et al., 2010) and gliotactin (Genova and Fehon, 2003).

Once the trachea reaches its final size and structure, taenidial rings form (Matusek et al., 2006; Ozturk-Colak et al., 2016) and the luminal matrix is degraded (Behr et al., 2007; Tsarouhas et al., 2007), allowing for gaseous inflation of the tube.

Despite the large body of literature of tube size regulation, there are many more aspects that are not understood. For example, although the apical transmembrane protein uninflatable is a key component of tracheal inflation (Zhang and Ward, 2009), the mechanism by which the lumen is cleared of fluid and inflated with air is still unclear. The importance of precisely measured and reproducible tube shapes and sizes is apparent by the multitude of signaling factors described above, but we are only beginning to piece together the physical mechanisms and constraints that allow this high degree of consistency across many individuals of a species.

Computational modeling to better understand tube development

Computational modeling is becoming more widely used as a tool to investigate biological phenomena, particularly for complex systems such as tubes that cannot be reduced to discrete points or simple shapes. For example, (Dong et al., 2014) demonstrated *in silico* that sinusoidal deformation of a cylindrical tube can occur due to the synthesis of apical membranes creating an expansion force that acts on a viscoelastic aECM (Fig. 1.6). Furthermore, while the number of sinusoidal turns per tracheal segment can vary depending on the elasticity of the aECM, side branches and/or fusion cells appear to anchor the DT at discrete locations, even in the most convoluted mutants. Although this restriction was not included in the model, it produced similar results to observations *in vivo*, demonstrating the power of computational modeling in better understanding biological phenomena.

The currently available computational tools to examine biological tubes such as the fly trachea remain limited. The best toolkits designed for quantifying epithelia work best on planar and pseudo-planar surfaces, whereas tubes have a much higher degree of curvature and require a different method of analyzing the tube surface or cell shapes. The most relevant program available is Imaris, which has been shown to be capable of

isolating single cells in the fly trachea in 3D in (Forster and Luschnig, 2012), but relied on custom Matlab code to manipulate and quantify the results. Other programs exist such as EDGE4D (Khan et al., 2014) and MorphoGraphX (Barbier de Reuille et al., 2015), and while these programs are powerful tools for analyzing most planar and pseudo-planar epithelia, they are insufficient to process and quantify the parameters necessary for tubes.

In order to bridge our understanding of the genetic factors to the contribution of mechanical forces that control tube size, I developed a program called QuBiT (Quantitation Tool for Biological Tubes) which is tailored, but not limited, to measuring narrow tubes such as the fly trachea. I used a publicly available, well-known, and well-documented platform in Matlab (Mathworks), which offers a large degree of accessibility, ease of maintenance, and extensibility. Tube-specific functions of QuBiT include tracing a tube's centerline and mapping branches, which has the additional utility of normalizing measurements between samples; and projecting tube surface data as a 2D image to better visualize object relations that are not as apparent through conventional image processing methods such as partial max projections. Full details on the development and capabilities of QuBiT are discussed in Chapter 2.

Through the use of QuBiT, my project is to understand the mechanisms of tube size control using the trachea in *Drosophila melanogaster* as a model. This is a well-studied model organism with many established tools and protocols. Many genetic factors that control tube development in flies such as FGF signaling (discussed above) and planar cell polarity components (Chung et al., 2009) are conserved in higher order organisms (reviewed in (Cross and Claesson-Welsh, 2001) and (Fanto and McNeill, 2004), respectively), opening the possibility that the physical mechanisms tied to those genes may also be conserved. I used a simple expansion model to show that although cell shape changes occur during tube inflation, this phenomenon is not necessary to preserve the integrity of the trachea. Instead, it is possible that changes to the structure of the aECM during tube expansion, such as axial rearrangement of chitin fibers due to the increasing tube length, causes the overlying apical cell faces to transiently change shape.

Finally, I set out to expand on previous studies on the fly trachea and identify previously unknown or unexplained phenomena. For example, (Nelson et al., 2012) have observed cell orientation changes in Src42 mutants, the only documented mutant line that supports the idea of cell shape changes causing tube elongation, but it's unclear whether cell orientation changes are the cause or a byproduct of tube elongation. I also

show distinct localizations of Uif, an apical transmembrane protein, around the DT circumference when it was previously assumed to be uniform. And while (Kumichel and Knust, 2014) observed elevated levels of Crumbs, an apical marker, in the boundary cells of the fly hindgut, I show that Uif has a reduced presence in the same cells, suggesting differential contribution of apical polarity factors in different tissues.

The overall goal of my work is to improve our understanding of tube size control mechanisms by tying classical genetic pathways together with physical mechanisms or forces.

Chapter 2: Development and Functions of QuBiT

This chapter demonstrates the capabilities of QuBiT, the Matlab-based tool of which I was the primary developer. E. Li contributed to code for the tube measurement modules and testing and verification of QuBiT, while M. Mani provided additional guidance on theoretical approaches.

The majority of this chapter has been published in: Yang, Li, Kwon, Mani, and Beitel.

Development 2019 146: dev172759 doi: 10.1242/dev.172759.

Overview

As a testbed for developing QuBiT and to identify novel biological processes, I used QuBiT to characterize the early development of the *Drosophila* trachea system, which is one of the best-studied systems of tubular epithelia (Fig. 1.4, reviewed in (Manning, 1993; Samakovlis et al., 1996)).

To maximize maintainability, accessibility, and extensibility of a tool for epithelial tube analysis, I developed QuBiT using commonly available and well supported software platforms rather than develop entirely new programs. The work flow is schematized in Fig. 2.1. Image stacks are generated by confocal microscopy using settings that produce cuboidal voxels. Image segmentation is performed on the entire stack using Ilastik, a general-purpose image segmentation program (Kreshuk et al., 2011). Segmented images are then analyzed using custom-written code in Matlab (open source available at <http://github.com/gjbeitel/QuBiT>). Tube analysis proceeds by segmenting the boundary of the tube lumen and creating a skeleton, which enables robust calculations of parameters of interest, including length, surface area, and cross-sectional area. Separately, cell junctions are masked onto the tube surface, resulting in apical cell surfaces that can directly be analyzed for parameters such as size and orientation. While

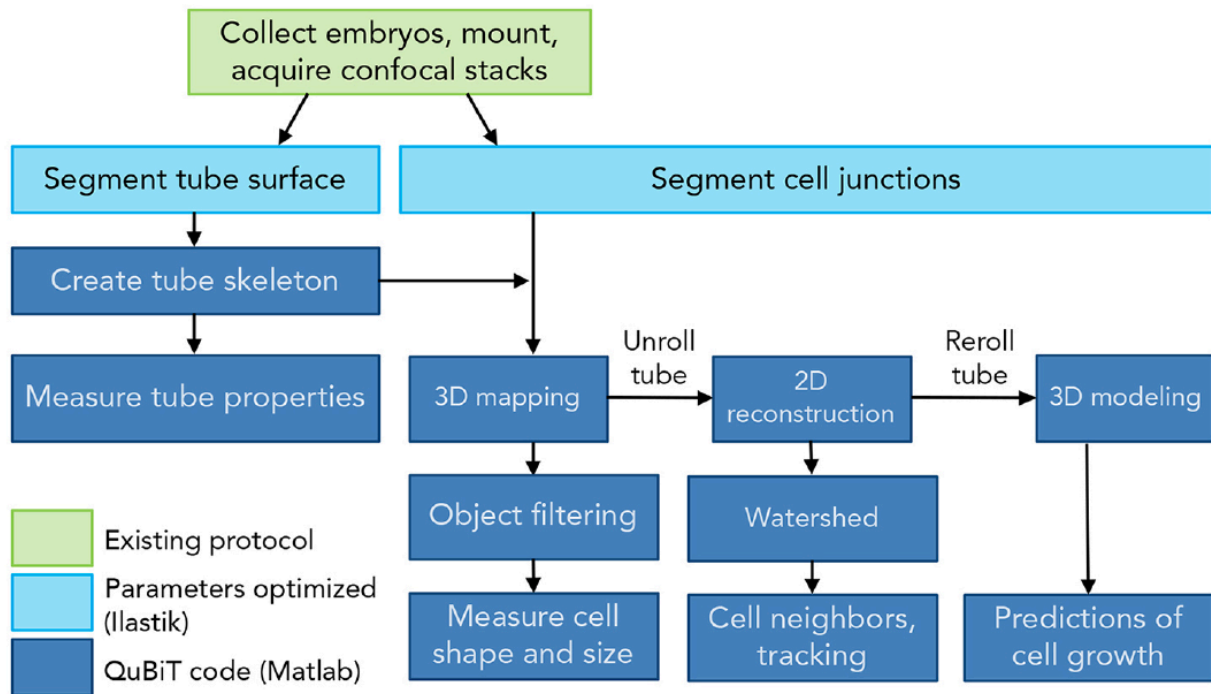


Fig. 2.1: Visual representation of the workflow QuBiT. For this project, segmentation of confocal image stacks was performed using Ilastik, but any segmentation software that can extract ROIs is compatible with QuBiT. Tube parameters are calculated separately from cell parameters, which rely on a reconstruction of the tube surface, one of the unique functions of QuBiT over other epithelial analysis software. Additionally, QuBiT has the ability to model cells on the tube surface as 2D “projections” through the unrolling algorithm and to model cell growth as a function of tube growth.

this approach does not yield a full 3-D reconstruction of the entire cell bodies that comprise a tube, it focuses on the apico-lateral junctions and regions that control tracheal cell shape and tube size (Beitel and Krasnow, 2000; Laprise et al., 2010; Sollier et al., 2015; Wodarz et al., 1995), and greatly simplifies the reconstruction problem.

Collection of image stack data

QuBiT is designed to analyze images collected with cuboidal voxels containing either tube surface or junctional information with enough resolution for the desired analysis. Basic length measurements were obtained using image stacks of entire whole-mount embryos collected using a 40X oil objective with a $0.38\mu\text{m}$ voxel size. Approximately 75 optical sections were collected per embryo. For cell parameter analyses, images were collected using a 100X oil objective with $0.15\mu\text{m}$ voxels, requiring around 200 slices.

Surface mapping and defining tube centerlines

QuBiT defines a tube surface using markers that either visualize the cell luminal/apical surface or the luminal contents themselves. For this work, the apical marker Uninflatable (Uif) (Zhang and Ward, 2009) and the aECM marker Vermiform (Verm) (Wang et al., 2006) enabled extraction of the tracheal system from surface epidermal staining using the Carving module in Ilastik (sample input and output in Fig. 2.2). The segmented data were then imported to Matlab, where a marching cubes algorithm (Cline et al., 1987; Hassouna and Farag, 2007) defines the centerlines of the main and side branches (Fig. 2.3). The tube centerlines, which are not calculated by other epithelia analysis software,

are of critical importance because centerlines define the lengths of tube segments, mark branch intersection points that define tube segments, are the local reference for determining cell orientation, and are necessary for calculating orthogonal planes used to quantify tube parameters including diameter, cross-sectional area and surface area (sample results in Fig. 3.1). To allow rapid investigation of different parameters without recalculation, computed results from the segmented data are stored with the image stack. For determining tracheal tube parameters, 10 cross-sections were taken per segment, which samples the tube approximately once every 15 voxels or 2.3 μm .

Cell mapping

To map cells onto the tube surface, QuBiT uses information from apico-lateral junctions. For the tracheal system, claudin Kune-Kune was used as a maker of septate junctions as was previously done (Nelson et al., 2010) because Kune staining gives a more continuous signal along the lengths of junctions than the E-cadherin staining, which improves segmentation.

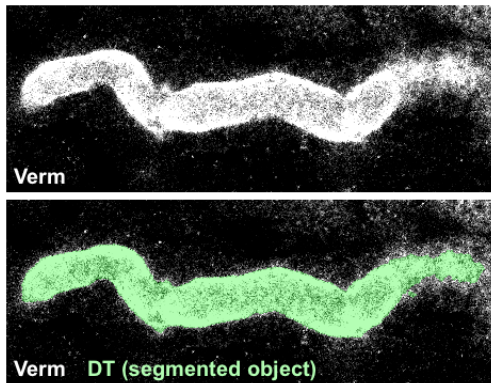


Fig. 2.2: Sample segmentation of tracheal tubes using Ilastik. The DT extracted from the image stack based on optimized segmentation parameters is highlighted in green. Image from a single XY slice.

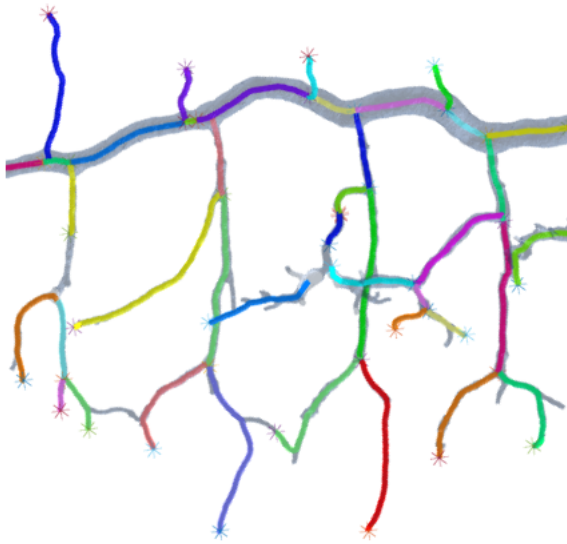


Fig. 2.3: Sample output of the segmented tube and calculated centerline in 3D. The filled tube (gray) is overlaid with centerline segments (individually colored lines), which intersect at nodes (asterisks). Line segments are indexed and joined when specifying the tube ROI. Although not used in this study, centerlines in side branches are shown here to demonstrate the capabilities of this feature. Left-right is anterior-posterior; top-bottom is dorsal-ventral.

Junctional segmentation was performed using the Pixel Classification tool in Ilastik with similar results to tube segmentation. The data were imported into Matlab and masked and inverted the junctions on the tube surface to obtain cell surfaces. A 1:1 comparison of the raw image stack to the resulting apical cell surfaces in 3D is shown in Fig. 2.4 and assisted in validating the cell quantification modules of QuBiT. I then calculated cell parameters that included area, cell orientation and aspect ratio (sample results in Fig.

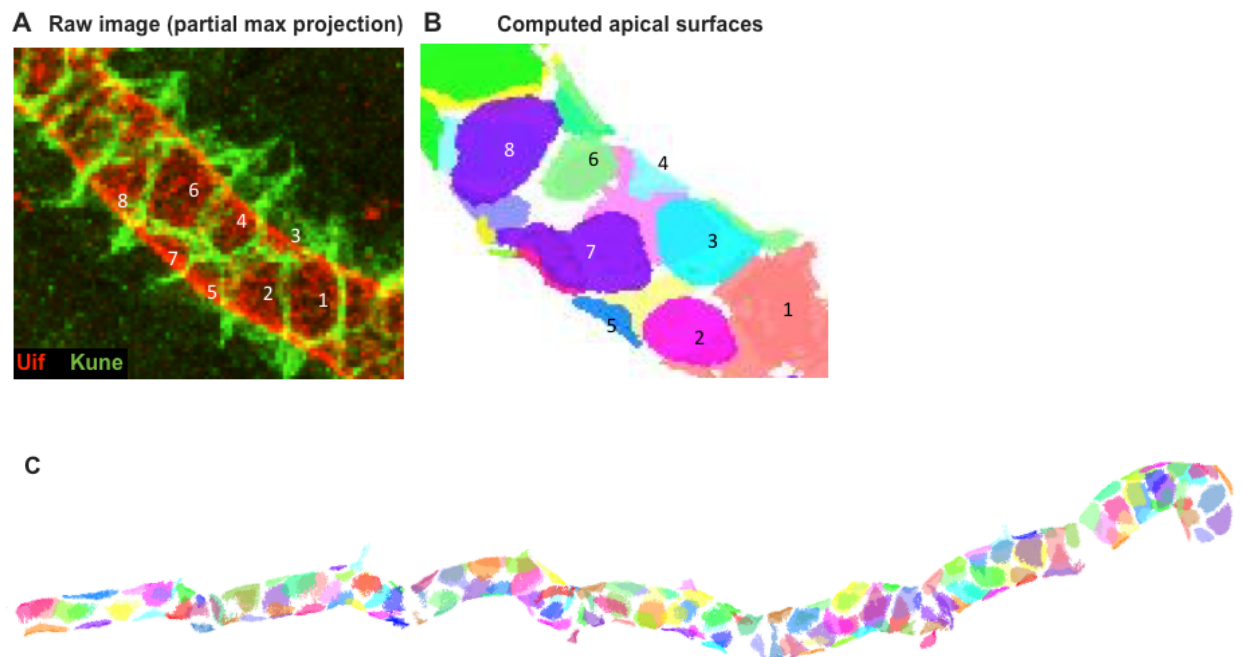


Fig. 2.4: Cell plotting. (A) Apical cell surfaces were created by inverting the cell junction signal (green, Kune) on the tube surface (red, Uif). The matching apical cell surfaces rendered in Matlab are shown in (B). (C) Sample output of cells from a whole image stack, after filtering. Left-right is anterior-posterior.

3.1). Because the small cell size, narrow diameter and junctional organization of the tracheal dorsal trunk leads to unresolvable segmentation errors, I used several parameters to filter the tracheal cell data. I applied a radial filter to exclude cells on dorsal branches and transverse connectives, an axial position filter to remove cells outside of regions of interest on the dorsal trunk, and a size filter to exclude improbably small or large cells.

Tube unrolling

To provide a planar representation of the cells that allows direct application of a broad array of existing 2D analysis tools, QuBiT can computationally unroll and flatten tubes. To do this, the exact cross-section is calculated using the orthogonal plane to the local centerline at regular voxel-sized intervals along the length of the dorsal trunk. The cell junction data is then extracted from projections radiating from the centerpoint in each orthogonal plane and write the data on a 2D plane (Fig. 2.5).

As an example of an operation that is much easier to perform in 2D, I used watershed segmentation to reduce cell junction widths to single pixels (Fig. 2.6). This creates a more accurate representation of cell interfaces and enables analysis of parameters such

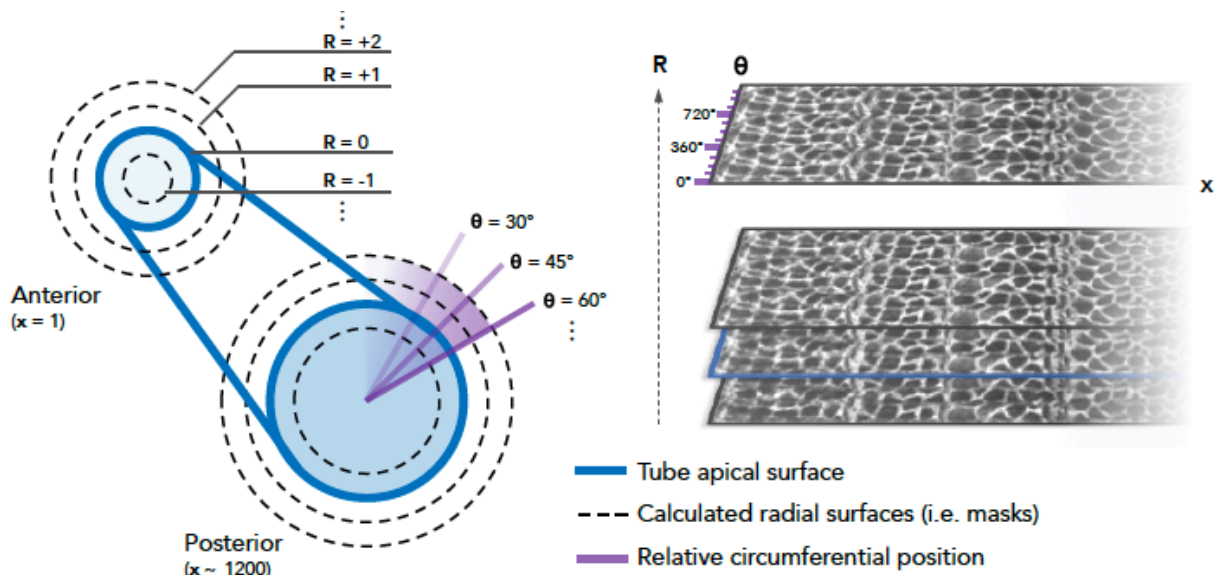


Fig. 2.5: Tube unrolling algorithm. (Left) A model diagram depicting QuBiT's method of calculating unrolled images. The segmented apical surface of the tube is outlined in blue. Masks (dashed lines) corresponding to different depths (R) relative to the apical surface were created by uniform dilation. At each cross-section along the length of the tube (x) the data from the source image was pulled from each mask at interval angles (θ). For the trachea, an interval of 4° was usually sufficient. (Right) The resulting image stacks visualizes the translation of data from the 3D model.

as cell connectivity (the number of cells any given cell touches) and the number of cells in a tube cross section, which were utilized in the analysis of the tracheal system below. In future work, 2D projections could be used to track tracheal cells through time more easily than in 3D, which is important in determining changes in cell arrangements.

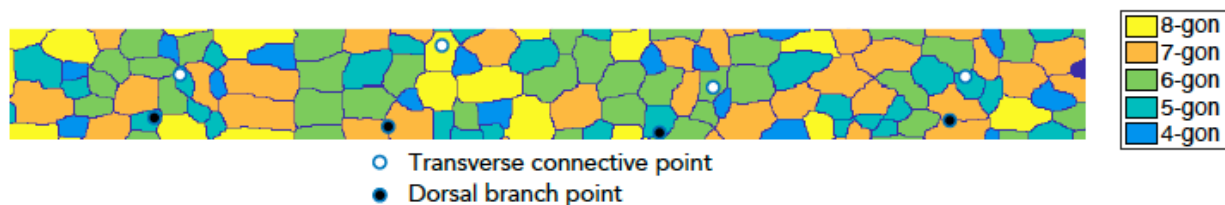


Fig. 2.6: Sample output of tube unrolling after watershedding, demonstrating the utility of this module. Apical cell surfaces are individually outlined and color-coded by their numbers of neighbors; branch points where the TC and DB intersect the DT are mapped. Left-right is anterior-posterior; vertical axis represents the tube circumference.

3D modeling

The process used in QuBiT to unroll a tube can also be utilized to recreate a tube from a 2D projection (Fig. 2.7). As an example of how this can be employed, I used tube unrolling and rerolling to test for evidence of active cell rearrangements during tracheal expansion. Embryonic stage 14 tracheal tubes were computationally expanded to the size of stage 16 tubes, and then compared the 3D parameters of the computed and actual stage 16 apical cell surfaces.

Tubes were computationally expanded by projecting the raw-unrolled 2D stage 14 cell data back onto 3D tube surfaces with corresponding lengths and radii of stage 16 tubes. To do this, the number of pixels was increased along the long (X) axis of each 2D projection proportionally to our measured changes in tube length using nearest neighbor interpolation. Then at each position along the model tube axis, the 2D image was sampled for cell surfaces and wrote the data on the orthogonal (YZ) circumference with corresponding radius based on stage 16 tube radii, which was normalized with respect to axial position. This resulted in a re-creation of stage 14 cell surfaces after tube inflation to stage 16 with no other changes to cell geometry or topology. One limitation of the resulting model is that the projected tube is perfectly straight, whereas the original tubes had small irregularities, which introduces a small amount of error. However, because of the asymmetric expansion along the length of the tube, the alternative approach of expanding along a curved path would result in over and or under expansion of some regions, which would also result in slight deviations. To determine whether systematic errors were introduced, I compared the effect of unrolling and rerolling stage 14 and 16 tubes. For both stages, there was excellent agreement between the original and rerolled tubes, with most parameters differing by no more than 6%, which is sufficient for the analyses in described below.

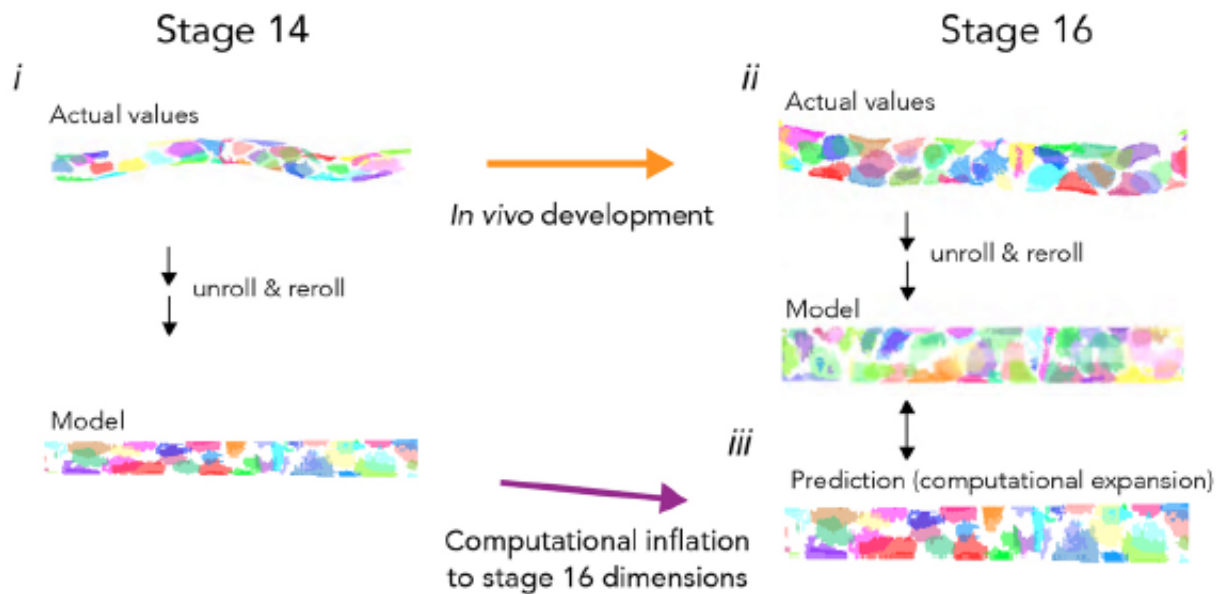


Fig. 2.7: Schematic of 3D modeling in QuBiT. Apical cell surface data were modeled on a conical tube at two distinct developmental stages of the trachea, (i) stage 14 and (ii) stage 16. (iii) The stage 14 model tube was then computationally inflated to match measured stage 16 tube parameters while retaining stage 14 cell proportions and topology, allowing a direct comparison between the predicted stage 16 cell parameters and the actual stage 16 cell parameters.

Methods of data analysis

For statistical analysis of tube parameters, QuBiT takes advantage of the extensive tools of Matlab's framework to allow users to perform statistical analyses on individual tubes, and also on multiple independent tubes simultaneously, without the need to export the

data into other analysis packages. Notably, for tubular systems with reproducible features, QuBiT has the ability to track, align, and compare identifiable features. In the case of the trachea, individual dorsal trunk segments were aligned rather than just normalizing to length along the tube. As detailed below, this enables calculations that reveal tracheal cell parameters differ not just between segments, but also within segments.

Chapter 3: Insights in wildtype tracheae

In this chapter, I show using wildtype tracheae that the outputs of QuBiT are robust and reproducible and that several features of even wildtype tracheae were not known or appreciated until they were uncovered by this work. I collected, processed, and analyzed all of the data presented in this chapter.

The majority of this chapter has been published in: Yang, Li, Kwon, Mani, and Beitel.

Development 2019 146: dev172759 doi: 10.1242/dev.172759.

Overview

I used wildtype (w^{1118}) tracheae as the basis for designing, testing, and verifying QuBiT. In addition to agreeing with the results of previously published data (which will be described below), the use of QuBiT produced several unexpected results that had never been characterized. These include: (1) anterior-to-posterior (A-P) gradients are present in many cell characteristics, including orientation and aspect ratio, (2) there exists a periodicity at the tube segment level to these characteristics within the A-P gradient, (3) inferred cell intercalation during development dampens an A-P gradient of the number of the number of cells per cross section of the tube, but these intercalation events do not change the connectivity distributions of tracheal cells, (4) cell connectivity distributions in the main tracheal tube are not influenced by the complex shapes of, or possible stresses on, cells that interface the side branches with the dorsal trunk. These results will be elaborated below and demonstrate both the utility of QuBiT for analyzing small diameter tubular epithelia, and the importance of quantitative analysis in understanding the cell biology of tubular epithelia.

DT tube and cell parameters exhibit anterior-posterior gradients

The work on fly embryonic trachea in this project was done at two distinct stages, 14 and 16. During this 2.5-hour window, a burst of luminal secretion rapidly inflates the trachea (Tsarouhas et al., 2007), doubling tube diameter and increasing tube length by about 15%, thus making these stages easily distinguishable through quantifiable metrics. Measurements through QuBiT verified that the dorsal trunk length increased by $13.7 \pm 1.3\%$ (Fig. 3.1A) and were not statistically different from manual length measurements of the same embryos ($250 \pm 18 \mu\text{m}$ by hand in Volocity vs. $263 \pm 6.9 \mu\text{m}$ using QuBiT at stage 16, $p = 0.17$, two-sample t-test). However, having the confidence of accurate measurements by QuBiT had the advantage of automatically generating measurements on each individual segment that allowed a more detailed analysis of the sizes growth of tracheal tubes than had previously been performed. For example, while it be expected that the individual dorsal trunk segments all expand equally, most of the dorsal trunk growth resulted from increased length of posterior segments DT4 through DT9 ($+22 \pm 8\%$), while the remaining anterior segments lengthened only slightly (Fig. 3.1A). Interestingly, anterior segments are generally longer than posterior segments, despite anterior segments having fewer cells (e.g. ~ 21 in DT3 vs. ~ 28 in DT9 (Robbins et al., 2014)). These results predict that anterior and posterior cells have either different

arrangements and/or shapes in their respective segments, which, as described below, is indeed the case.

Many dorsal trunk cell properties have an anterior-to-posterior gradient

To investigate how the shapes of the tracheal cells might contribute to control of tube size, I measured shape parameters of tracheal cell apical surfaces at stages 14 and 16 (Fig. 3.1D-F). I focused on the apical surface because previous work has indicated that tracheal size is regulated at the apical cell surfaces (Laprise et al., 2010; Nelson et al., 2012; Olivares-Castineira and Llimargas, 2017; Robbins et al., 2014), while the shape of basolateral surface is not regulated (Beitel and Krasnow, 2000).

I first examined how the apical area of individual tracheal cells changes as a function of segmental location and stage. Before tracheal tube expansion at stage 14, tracheal cells in all segments have similar apical areas (Fig. 3.1D, blue line), and though there is some variability within each segment, there is no apparent A-P gradient. During tube expansion, the area of all tracheal cells increases ($p < 10^{-47}$, comparing stage 14 to stage 16, paired t-test), but posterior cell area increases somewhat more, resulting in a shallow

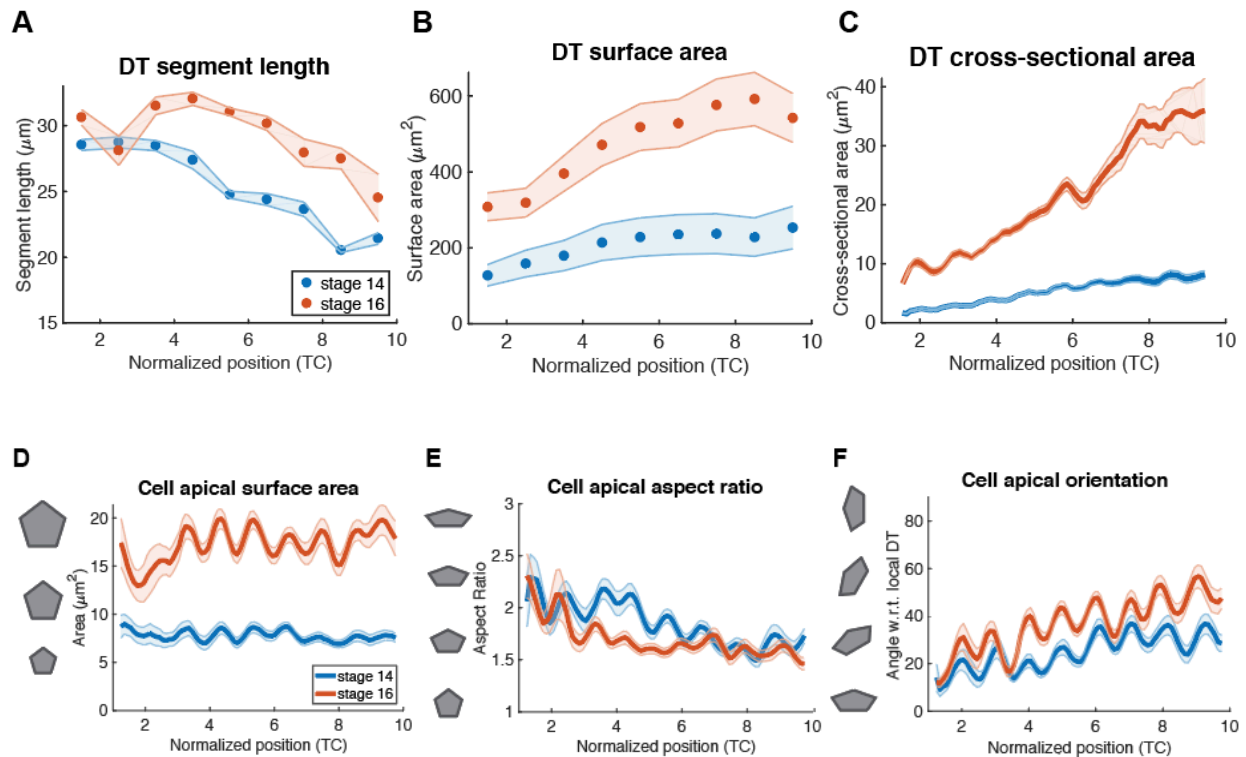


Fig. 3.1: w^{1118} tube and cell measurements ($n=6$ tubes for each genotype; $n=692$ cells and $n=854$ cells were identified at stages 14 and 16 respectively, resulting in approximately 75% of expected cell recovery). DT measurements of (A) segment length, (B) segment surface area, and (C) cross-sectional area relative to the A-P position on the tube axis. Apical cell surfaces were measured for their (D) surface area, (E) aspect ratio, and (F) orientations.

A-P cell apical area gradient (Fig. 3.1D). This shallow gradient is in marked contrast to the much more pronounced and uniform A-P gradient in anterior vs. posterior segment surface area where the A-P difference is almost 2-fold (Fig. 3.1B). The discrepancy

between the fairly uniform cell area and graded segment surface area predominantly results from posterior segments being both shorter (Fig. 3.1A) and having more cells than anterior cells (~21 cells in DT3 vs. ~28 cells in DT9) (Samakovlis et al., 1996).

I next investigated apical cell shapes by calculating their aspect ratios (Fig. 3.1E). In contrast to the mostly uniform cell area of tracheal cells, the shape of tracheal cells is not uniform. Anterior cells have higher aspect ratios than posterior cells ($p < 10^{-3}$ at both stages 14 and 16, unpaired t-test of DT2 vs DT10), but overall, aspect ratio does not change significantly during development ($p = 0.21$, paired t-test).

As with cell size and aspect ratio, cell orientation also shows an unexpected A-P gradient (Fig. 3.1F). It was previously shown from an analysis of a small number of cells that the long axes of tracheal cell apical surfaces in tracheal segment 8 (DT8) are not aligned with the long axis of the tracheal tube, but instead lie at an approximately $42 \pm 21^\circ$ angle at stage 16 on average (Forster and Luschign, 2012; Nelson et al., 2012). In excellent agreement with these previous measurements, I found that the average cell orientation in DT8 was $37 \pm 12^\circ$. However, when measuring cell orientations in all tracheal segments, I found that anterior cells tend to be oriented along the trunk axis with an average angle of $28 \pm 5^\circ$, whereas posterior cells tend to be oriented along the circumference of the tube with an average angle of $46 \pm 4^\circ$ (unpaired t-test using DT2 against DT9 at stage 16,

$p < 10^{-4}$). The gradient also exists at stage 14 ($p < 10^{-3}$) and cell orientations differ significantly between stages 14 and 16 ($p < 10^{-14}$, paired t-test).

DT cell properties have segmentally repeating variations

Despite tube surface area increasing fairly linearly from anterior to posterior (Fig. 3.1B), apical cell areas and aspect ratios at stage 16 show a strongly periodic pattern, with cell area and aspect ratio having local minima close to the points where the transverse connectives join the dorsal trunk, and local maxima at the middle of a segment (Fig. 3.1D and 3.1E). Cell orientation also shows a sinusoidal pattern, but the phase is opposite to those of surface area and aspect ratio, with orientation having local maxima where the transverse connective (TC) branches connect to the DT (Fig. 3.1F). This sinusoidal pattern is robust with respect to the window size used to calculate average cell apical surface area along the tube, with the periodicity being clearly visible with window sizes ranging from at least 0.6 to 0.3 of a segment. Notably, the sinusoidal pattern corresponds to the physical organization of the trachea. The dorsal trunk is comprised of nine distinct segments that derive from nine clusters of epidermal cells during development. Rather than the tube being a continuous cobblestone of cells, the cobblestone pattern is punctuated by pairs of thin, washer-like cells called “fusion cells”

that join adjacent segments just posterior to where the transverse connectives branch from the dorsal trunk. DT cells close to the fusion cells have reduced apical sizes relative to DT cells more distant from fusion cells.

One explanation for this segmental sinusoidal periodicity could be that the fusion cells constrain tube growth such that the tube is wider between fusion points. However, WT stage 16 DT tubes do not show constrictions at the fusion cells, and the plotted measurements of tube cross-section area and radius do not show segmental periodicity (Fig. 3.1C). Thus, the differential areas of cells close to or further away from fusion appear arise from differences between the cells and/or difference in the local luminal environment. As no periodicity has been observed in luminal proteins or organization, it then seems likely that the DT cells closer to fusion cells expand their surface area less in response to secreted luminal contents than do DT cells in the middle of the segment. Consistent with this hypothesis, uniform overexpression of the glycoprotein tenectin in the DT using the *btl*-Gal4 driver results in tracheal segments in which the diameter of the tube increases more between fusion cells than at fusion cells, with the change in diameter along the segment being a smooth curve rather than a step at the fusion cell (Fig. 3.2).

A simple cell expansion model suggests cell rearrangement during DT expansion

Given that expansion of the tracheal length and diameter is highly asymmetric, with length and diameter increasing by 13% and 100% respectively, I asked if the changes in cell size, aspect ratio, and orientation could result simply from an inflation of the tube, as if one were to inflate a cylindrical balloon with cell apical surfaces drawn on the surface. This is an appropriate model for the tracheal system because there is no change in cell number during tracheal development (Samakovlis et al., 1996); therefore changes in tube size must result from changes in cell shape and/or cell arrangement. As described above, QuBiT was used to computationally expand stage 14 tubes, and consequently the cells that make up the tube, to their respective stage 16 sizes (Fig. 3.3). I then analyzed the cell shape and orientation parameters of the resulting “computationally expanded” cells (3.4iii) and compared them to cells from stage 14 and to 16 tubes that had been similarly unrolled and rerolled, but without computational expansion (3.4i and 3.4ii, respectively, termed “model”).

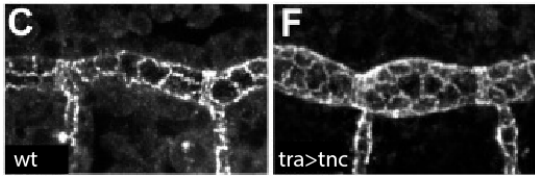


Fig. 3.2: Tenectin mutants have bulgy tracheal segments, unlike wildtype tubes, which have a relatively smooth A-P gradient of tube radius. However, in tenectin mutants, the fusion cell regions appear to be “tied down” and don’t change in diameter relative to their wildtype counterparts, suggesting their morphologies are fixed. Adapted from (Syed et al., 2012).

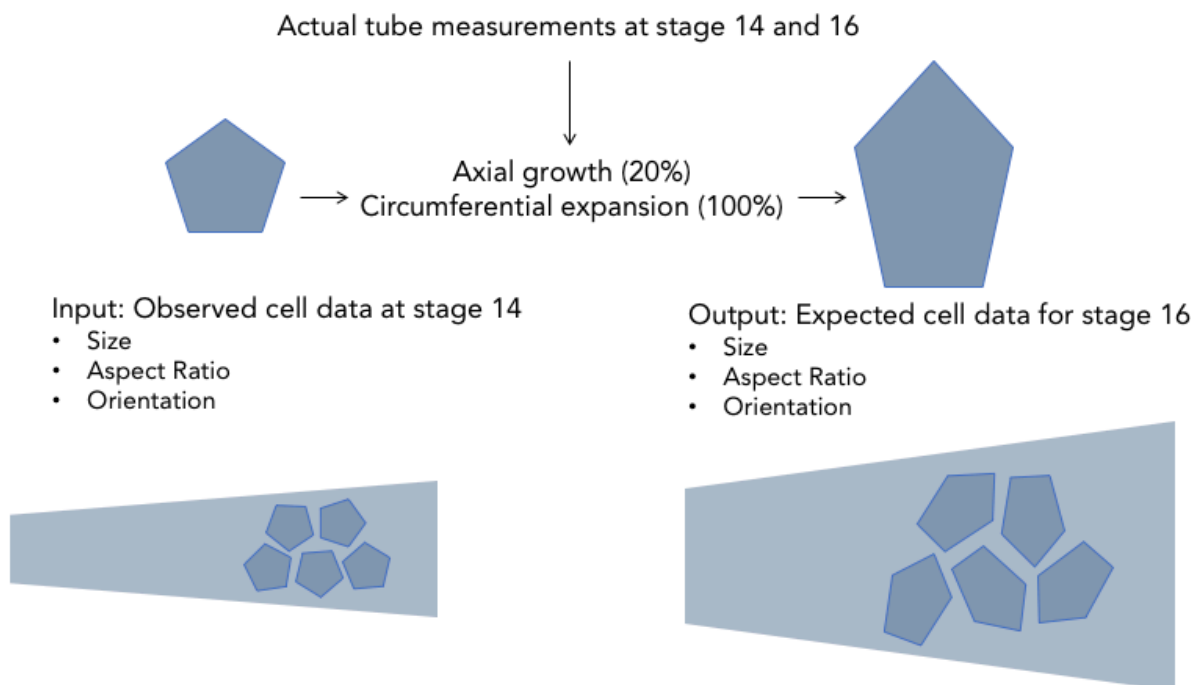


Fig. 3.3: The theory of a simple tube expansion model. The apical cell surfaces can be computationally “grown” from their observed stage 14 shapes to their predicted stage 16 shapes based only on measurements of DT sizes at the two developmental stages.

As an internal control, I first examined cell apical area (Fig. 3.5A). Apical area in the computationally expanded tube and actual stage 16 data were comparable, ($p = 0.15$, paired t-test), with the computational model still showing the strong segmental periodicity observed in the actual data. Interestingly, cell aspect ratio (Fig. 3.5B) and orientation (Fig. 3.5C) were also comparable between in vivo stage 16 data and

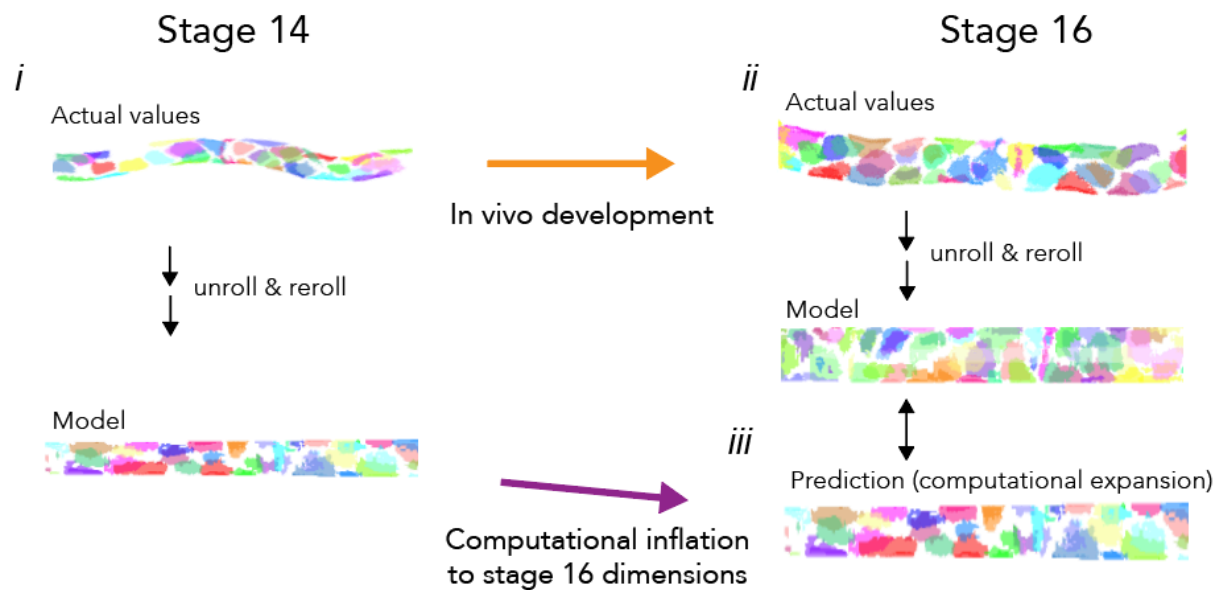


Fig. 3.4: Tube expansion (as theorized in Fig. 3.3) occurs through computational unrolling and rerolling, which are necessary steps to maintain comparability between datasets. Model: apical cell surfaces on a truncated cone (using radii from real measurements). Prediction: models inflated to stage 16 parameters.

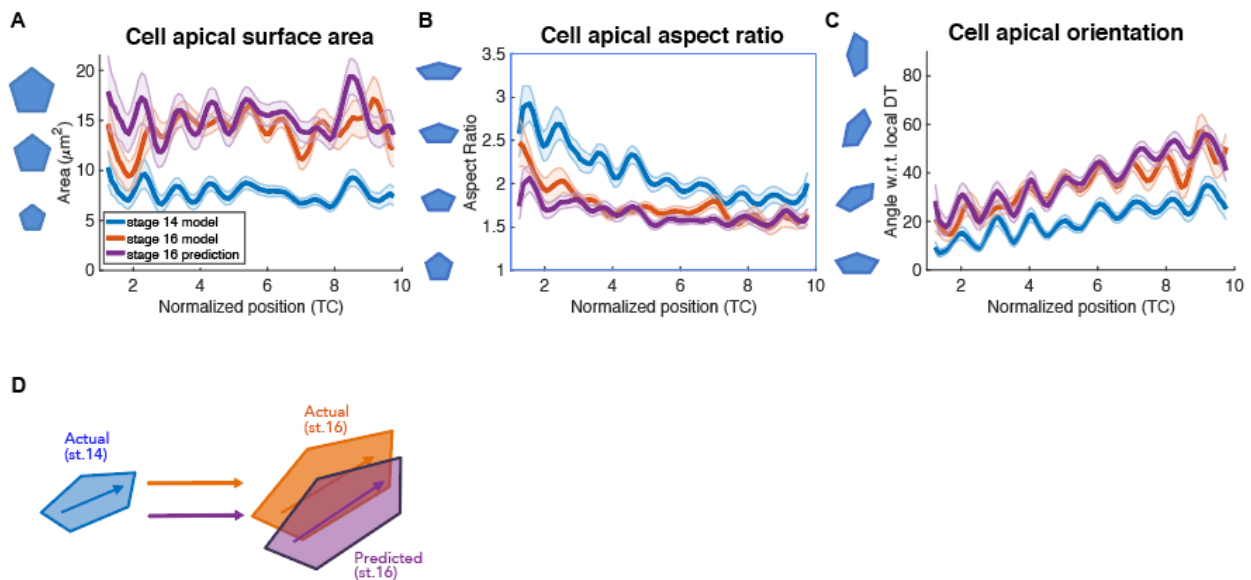


Fig. 3.5: Expansion of wildtype tubes. All of the apical cell parameters measured (A) surface area, (B) aspect ratio, or (C) orientation are in agreement with the predicted profiles. (D) A visual representation of the result. The apical cell shape changes during tracheal inflation can be explained purely by tube expansion stretching out cells.

computationally expanded tubes ($p = 0.09$ and 0.31 respectively, paired t-test), indicating that changes in cell apical shape during tracheal growth are consistent with tracheal cells passively expanding their apical surfaces in response to inflation of the lumen.

The distribution of dorsal trunk cell connectivity does not change during tube expansion

If tracheal cells simply expanded their apical surface areas in response to lumen inflation, in the simplest case there would be no changes in the cell organization, and the connections between cells would remain static. However, previous work has demonstrated that cell intercalation occurs during tracheal DT growth (Forster and Luschnig, 2012). To test whether QuBiT can find evidence of such intercalations, and to investigate the possible effects of such intercalation, I used QuBiT to measure two quantifiable parameters of cell organization (Fig. 3.6): the number of connections each tracheal cell has with neighboring cells (cell connectivity, demonstrated in Fig. 2.6) and the number of cells per tube cross section (CPC).

Cell connectivity can refer to both the number of cells that a given cell shares contacts with, as well as the specific connections a cell has with neighboring cells. Because data from discrete timepoints is analyzed as opposed to time-lapse images, I focused on the number of contacts that tracheal cells have and how that parameter changes along the

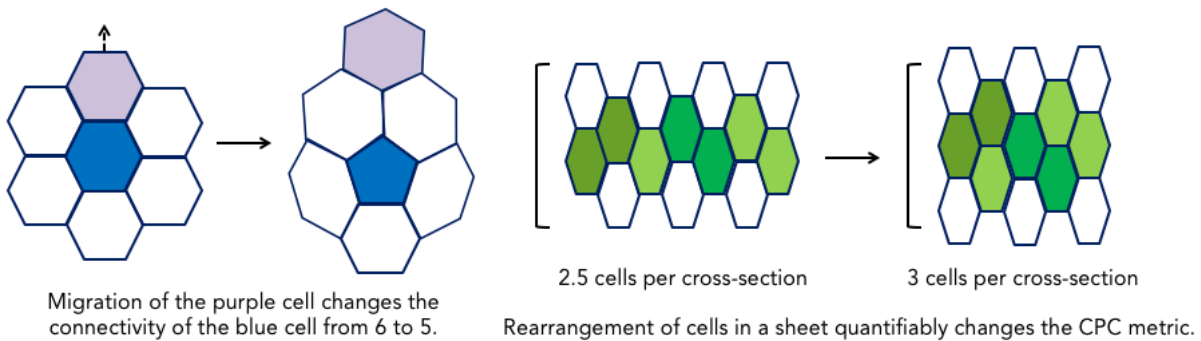


Fig. 3.6: Theory of connectivity and cells per cross-section (CPC) as indicators of rearrangement. (A) Cell migration or rearrangement can change connectivity by creating or removing junctions, such as during neighbor exchange events. It should be noted that while changes in connectivity necessarily indicate rearrangement, the reverse isn't always true; migration can occur with no net change in connectivity, such as during T1-T2-T3 transitions (Tada and Heisenberg, 2012). (B) Larger-scale rearrangement of cells in planar tissue can also alter CPC, such as during germband extension in *Drosophila* (see, for example, (Collinet et al., 2015; Fernandez-Gonzalez et al., 2009)).

length of the dorsal trunk and during development. Changes in the distribution in the number of contacts cells have is indicative of migration or other rearrangement events. However, as detailed below, an unchanging connectivity distribution does not demonstrate an absence of cell rearrangement.

To quantify cell connectivity in the trachea, I used QuBiT's capabilities to unroll the tube to create 2D representations of tracheal cells. I then quantified and visualized cell-cell connectivity using watershed segmentation (Fig. 3.7, degrees of connectivity coded by color). Stage 14 and 16 tracheae are predominantly composed of a mix of pentagons and hexagons (Fig. 3.7, blue and green bars). There was no obvious clustering of any particular type of polygon at either stage, and the distribution of polygon types is quite uniform along the length of the tube.

The distribution of dorsal trunk cell connectivity is not impacted by side branches

I also took advantage of QuBiT's ability to accurately map tube branch points to ask whether there were any particular patterns of connectivity associated with the points where the side branches of the DB or TC exit the dorsal trunk. No obvious patterns of cell connectivity, or organization of surrounding cell connectivity were observed in 2D

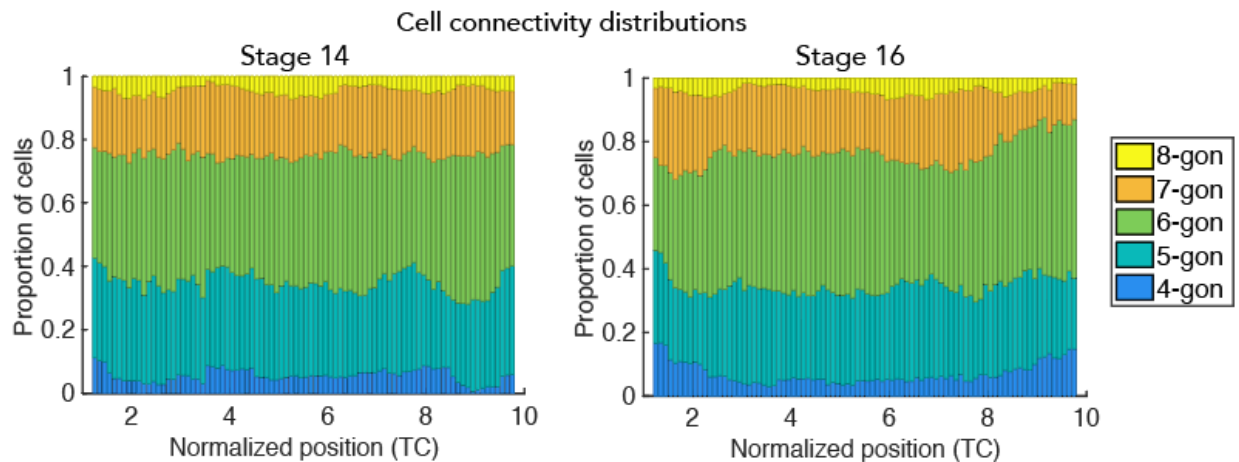


Fig. 3.7: Cell connectivity distributions for w^{1118} , which were generated using watershed segmentation of unrolled tubes. No obvious patterns of connectivity are present and the distributions of cell types are not significantly distinguishable between the two measured stages.

maps of tracheal tubes, indicating that neither the complex shapes of the individual cells that contribute to both the dorsal trunk and the side branches nor any forces resulting from tension on the side branches significantly impact the connectivity surrounding dorsal trunk cells.

Importantly, there was no significant change in the distribution of polygons between stages 14 and 16 (Fig. 3.7, $p = 0.23$, χ^2 test). Thus, it appears that there is little or no change in cell connectivity during tube expansion. This result is consistent with intercalation events occurring infrequently enough that they cause little change to the

overall connectivity, but is also consistent with the occurrence of intercalation events conserving their cell connectivity, such as occurs in the T1-T2-T3 transitions and rosette formation in epithelial sheets that drive cell intercalation during convergent extension in zebrafish (Sepich et al., 2000; Tada and Heisenberg, 2012), flies (Blankenship et al., 2006; Irvine and Wieschaus, 1994; Munjal et al., 2015; Pare et al., 2014; Simoes Sde et al., 2014; Zallen and Wieschaus, 2004), and vertebrates (Lienkamp et al., 2012). I further investigated these two possibilities below.

The number of cells per cross-section changes during tube expansion

To distinguish between a paucity of cell rearrangements versus active changes in cell organization that conserve cell connectivity, I determined the number of cells per cross-section (CPC) of the tube. Infrequent cell intercalations should not significantly change the CPC, but in a tube, even intercalation events that conserve cell connectivity would lead to changes in the number of cells per tube cross section if they occurred with significant frequency. The 2D diagram outputs of the unrolling algorithm were used to examine the number of cells in orthogonal cross-sections of the dorsal trunk at stages 14 and 16 (Fig. 3.8A), which yields two notable observations.

First, similar to the patterns observed for cell aspect ratio, orientation and area, a sinusoidal pattern of the number of DT CPC also emerges (Fig. 3.8C). Second, in contrast to the lack of change in connectivity distributions during development, the DT CPC changes from stage 14 to 16, most notably in the anterior and posterior ($p < 10^{-3}$ from TC1 to TC4 and $p < 10^{-10}$ from TC7 to TC10, paired t-test). Critically, since the simple tube expansion model preserves the organization of tracheal cells, the CPC in the computationally expanded stage 16 tube is the same as the original stage 14 tube and is also statistically different from measured stage 16 tubes. Thus, while a simple apical expansion model was sufficient to account for the changes in cell parameters during dorsal trunk expansion, QuBiT results indicate that cell intercalation events are actually common during tracheal maturation. QuBiT's ability to predict the existence of cell intercalation events demonstrates that it can be used to reveal developmental changes in cell organization even in circumstances where live imaging of tube morphogenesis is not feasible.

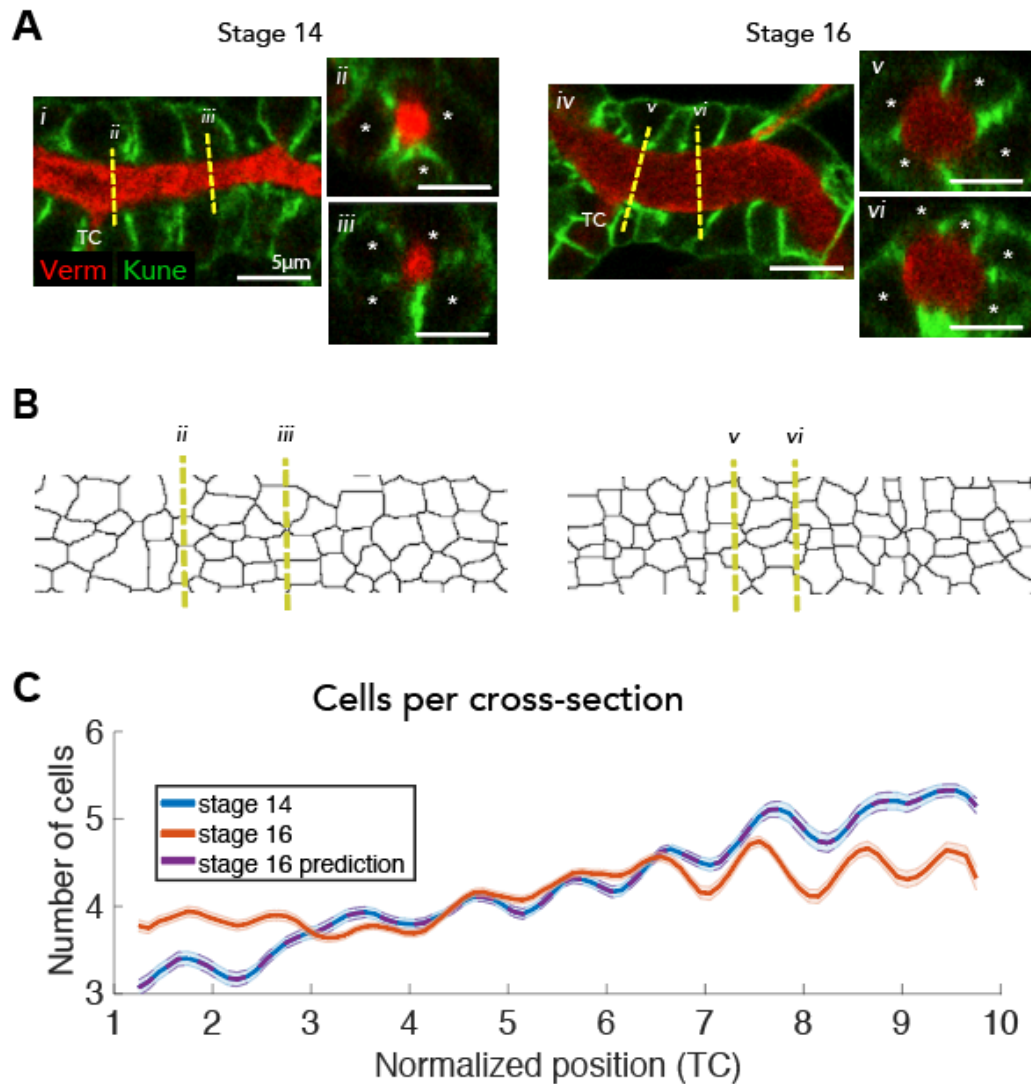


Fig. 3.8: Cells per cross-section (CPC) for w^{1118} . (A) Representative raw images of a single z-slice and their cross-sections (dashed yellow lines) at stages 14 (i-iii) and 16 (iv-vi) that correspond to the unrolled maps in (B). (C) CPC changes between stage 14 (blue line) and 16 (orange line) tracheae, which indicates that cell intercalation events are occurring. The change in CPC is not predicted by the model of the tracheal cell apical surface passively expanding in response to luminal inflation (purple line). A sinusoidal pattern of CPC is superimposed on an A-P gradient, with a period coinciding with each tracheal segment.

Tube unrolling reveals unexpected patterns of Uif localization

In addition to using tube unrolling to examine cell connectivity, I used unrolling to simultaneously visualize the entire DT tube surface and visually search for patterns in the organization of the apical marker Uif in WT stage 16 trachea (Fig. 3.9A). Surprisingly, whereas Uif was thought to be a uniform marker of the tracheal apical surface, in the unrolled projections it is immediately apparent that the tube surface has previously unrecognized A-P “bands” of Uif signal, twice per circumference, that are elevated compared to the rest of the tube and that are not interrupted by the washer-like fusion cells that disrupt cuticle pattern at this stage (Fig. 3.9B, yellow arrowheads). Notably, these bands are in register with the TCs and DB branch exit points with one band being aligned with the DB exits and the other with TC exits (Fig. 3.9B, white and black circles indicate TC and DB exits, respectively).

To verify these observations, I examined unrolled images at various depths (ranging from $R = [-6$ to $+10]$, the equivalent of $[-1\mu\text{m}$ to $+1.5\mu\text{m}]$) from the segmented apical surface and found the same phenomenon at any surface level (data not shown). The banding does not result from a technical artifact such as imaging depth because no such banding is visible in the junctional staining channel (Fig. 3.9C), but banding is visible in

tube cross sections generated by the Volocity program (Fig. 3.9E, yellow arrowheads). Moreover, the dimmest regions do not correspond to the deepest sections. Closer examination reveals that the Uif bands have a supracellular organization that is contiguous across cells. While transitions from high to low Uif levels can happen at cell-cell boundary (Fig. 3.9D insets, dots), many cells show discrete regions of high and low Uif levels on a single apical surface (Fig. 3.9D insets, arrowheads). The biological significance of these Uif bands will be investigated in future studies, but as the existence of Uif bands is not obvious in conventional confocal projections (Fig. 3.9A) or slices (Fig. 3.9F) and has not previously been recognized despite the common use of Uif as a marker, these findings highlight the benefits of using QuBiT to analyze biological tubes.

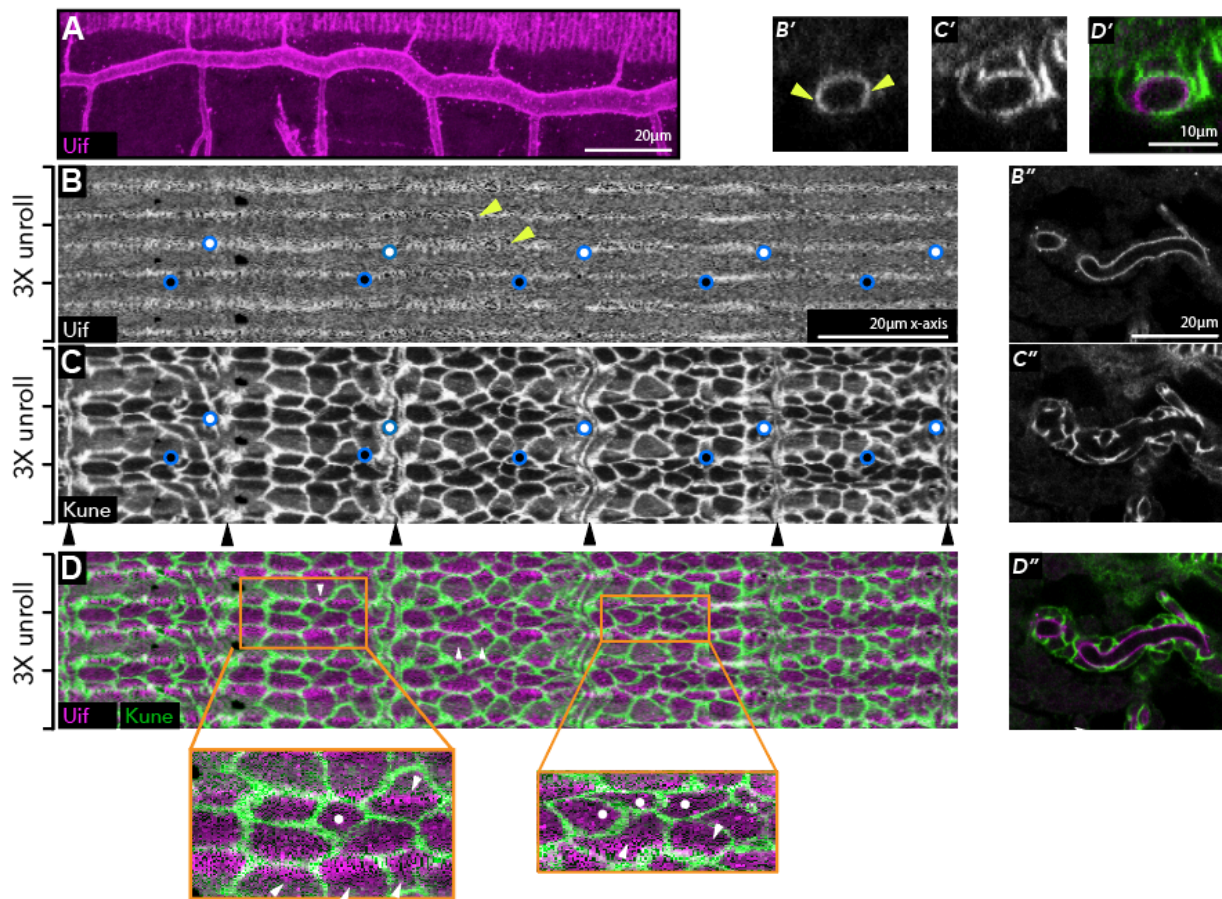


Fig. 3.9: Representative unrolled tube data for w1118 ($n=6$ tubes). (A) Partial max projection of the DT. (B) Unrolled Uif channel at $R=-1$. White and black dots represent branch points where the TC and DB respectively intersect the DT. Yellow arrowheads indicate regions where the Uif distribution is not uniform about the circumference of the tube. (C) Unrolled Kune channel at $R=+1$. Black arrowheads indicate fusion cell regions. (D) Merge. Insets show a small subset of cells. White dots denote cells whose junctions overlap the Uif bands, while arrowheads denote bands of Uif that extend through the centers of cells, suggesting that concentrations of the apical marker are cell-autonomous. (B'-D') Representative cross-sectional (Y-Z) slices of the confocal images of their respective channels.

Chapter 4: Src42 and dDAAM mutants impact tube structure and cell geometry

In this chapter, Src42 and dDAAM are shown to influence many tracheal parameters, including tube length and cell orientation. The results here are in agreement with previous findings, but this work yielded unexpected results, including a potential interaction between Src42 and Uif and detachment of the lumen from the apical surface in dDAAM mutants. Y.-J. Kwon built the dDAAM^{IK} allele using CRISPR. Half of the datasets of Src42 and all of the dDAAM datasets were collected by Y.-J. Kwon. Collection of the remaining datasets and all computational processing and data analysis was done by me.

Only Fig. 4.1 has been published in: Yang, Li, Kwon, Mani, and Beitel. Development 2019 146: dev172759 doi: 10.1242/dev.172759. The remaining results and discussions are included here to provide a clearer understanding of the roles of Src42 and dDAAM in tube size control and may be considered for publication in the future.

Introduction to Src42

The other tracheal mutant that has been previously been studied with quantitative tools is Src42 (Forster and Luschnig, 2012; Nelson et al., 2012), which proved to be useful as additional validation for QuBiT and, more importantly, the molecular basis for further understanding tube size control mechanisms. Src is a non-receptor tyrosine kinase with known roles in many cellular functions, including cell growth and proliferation (Pedraza et al., 2004), migration (Somogyi and Rorth, 2004; Sun et al., 2019), and apoptosis (Pedraza et al., 2004; Poon et al., 2018). Additionally, a small set of studies have shown that Src-family kinases Src, Fyn, and Yes are also involved in regulating tube development in mammalian endothelial cells as well as in the *Drosophila* trachea, but the field is mostly unexplored. In mammals, the Src family likely functions downstream of receptor tyrosine kinases such as VEGF (Werdich and Penn, 2005) and PDGF (Marx et al., 2001) to facilitate tube formation in retinal and vascular endothelia, respectively. Recently, apical polarization and maintenance of Src has been shown to be necessary for both vasculogenesis and angiogenesis (Kim et al., 2017).

Flies have two Src orthologues: Src42 and Src64, though they can have non-overlapping functions (Laberge et al., 2005). Src42 mutants have been shown to have a direct effect on tube size control, causing the DT to become shorter and, more interestingly, apical cell surfaces to increase their angle of orientation with respect to the DT axis (Forster and Luschnig, 2012; Nelson et al., 2012). The effects of these mutants can be rescued by driving wildtype Src42 in the trachea, and overexpression of constitutively active Src42 creates longer tubes with diminished cell angles. Because Src42 mutations are epistatic to all known mutants that cause tube elongation, Src42 appears to act downstream of other tube size control factors, including septate junction components such as Nrv2 and aECM components such as Verm (Nelson et al., 2012). These data point to Src42 as an important regulator of tube size.

Src42 acts in conjunction with other systems to regulate cell orientation

As Src42 is the only *Drosophila* mutant whose apical cell orientation that has been independently analyzed (Forster and Luschnig, 2012; Nelson et al., 2012), I first verified these results using QuBiT. Analysis using QuBiT confirmed that compared to WT, Src42 DTs are 24% shorter ($p < 10^{-3}$, Fig 4.1A) and 13% larger in diameter ($p = 0.01$). DT cell apical surface area is reduced by ~28% ($p < 10^{-30}$, Fig. 4.1D), but cell apical aspect ratio

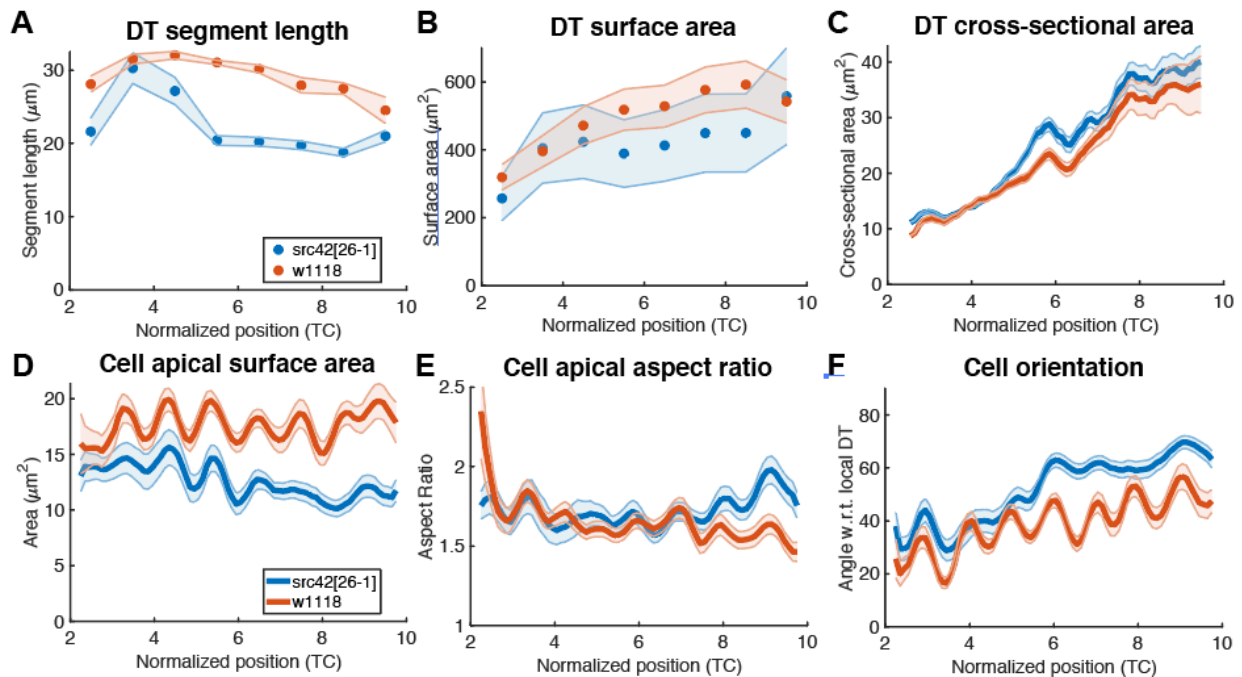


Fig. 4.1: Src42 tube and cell measurements ($n=6$ tubes, 754 segmented cells resulting in 78% cell recovery). DT measurements of (A) segment length, (B) segment surface area, and (C) cross-sectional area relative to the A-P position on the tube axis. Apical cell surfaces were measured for their (D) surface area, (E) aspect ratio, and (F) orientations.

is largely unchanged (Fig. 4.1E). Importantly, the cell apical orientations determined by QuBiT for *Src42²⁶⁻¹* in segment 8 are in good agreement with previous studies by (Forster and Luschnig, 2012; Nelson et al., 2012). (this report: $60 \pm 23^\circ$; Nelson et al., 2012: $66 \pm 28^\circ$; Forster and Luschnig, 2012: $73 \pm 12^\circ$), and are oriented more circumferentially than in WT ($+13 \pm 36^\circ$; $+24 \pm 36^\circ$; and $+11 \pm 21^\circ$, respectively). However, the order-of-magnitude higher

throughput of QuBiT extends the previous analyses by showing that although the intra-segment orientation gradient appears dampened, the overall A-P cell apical orientation gradient is still present in *Src42²⁶⁻¹* mutants (Fig. 4.1F). Since loss of *Src42* does not “lock” all tracheal cell apical surfaces in a strongly orthogonal orientation, *Src42* is unlikely to directly control tracheal cell apical orientation. Instead, normal activity of *Src42* may bias the orientation of cell apical surfaces whose orientation is predominantly determined by a *Src42*-independent mechanism.

Further analysis of *Src42* mutant tubes yielded several unexpected results. First, the luminal marker *Verm* had to be used to outline the trachea instead of the apical marker *Uif* due to poor *Uif* staining, particularly in the posterior DT, of these mutants (Fig. 4.2). Though it is possible that the *Src42* regulation of apical character in mouse (Kim et al., 2017) is conserved in flies, *Src42* has not previously been shown to interact with *Uif* or any other apical determinants, and this would be the first evidence of such an interaction.

Second, *Src42* mutants have increased non-uniformity of apical cell size. The wildtype apical cell surface fields generally have less variability (Fig. 3.9C) than those of *Src42*, and interestingly, the largest cell surfaces in *Src42* coincide with the weakest levels of

Kune (Fig. 4.3C). This phenomenon is not seen in the Verm channel, indicating it is specific to cell junctions. Finally, SJ levels are greatly reduced in the tube cross-sections (Fig. 4.3C') such that they appear to be condensed into spots around the tube surface rather than protruding radially (compare to Fig. 3.9C'). Taken together, these results

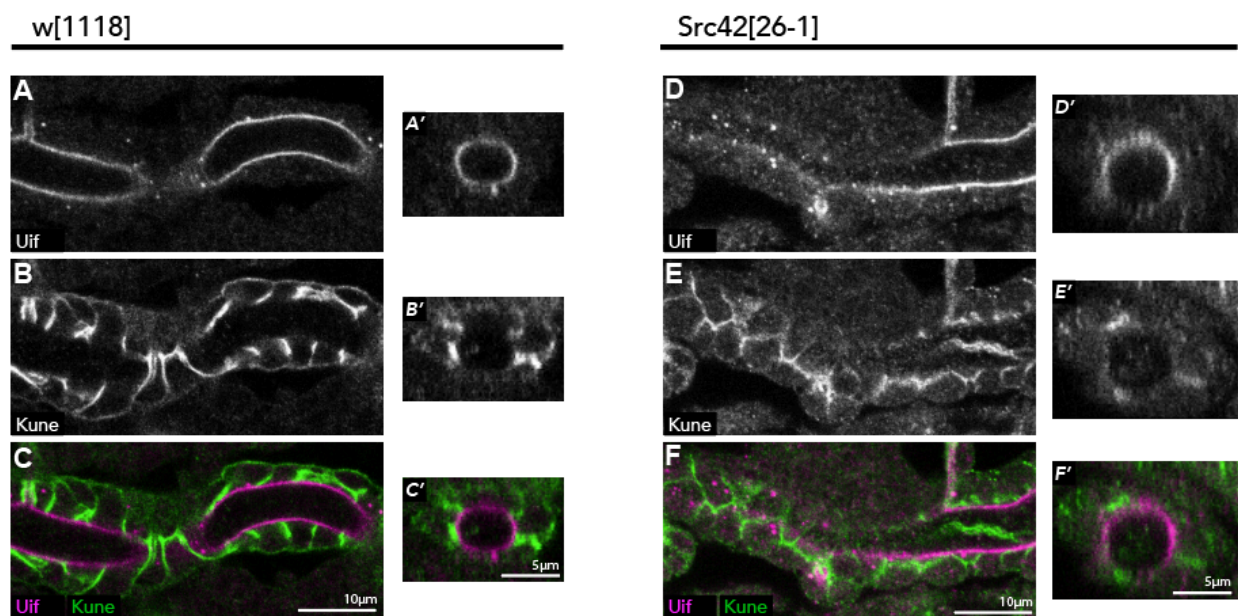


Fig. 4.2: Src42 mutants disrupt Uif. Representative confocal slices in (A-C) w1118 (n=9 tubes) and (D-F) Src42[26-1] (n=6 tubes). Although there is some variability in signal intensity, Uif nonetheless encompasses the entire trachea in wildtype embryos (A,A'), whereas in Src42 mutant, the outline of the DT is compromised due to the dissociation of Uif from the apical surface (D,D'), resulting in failure to further process this data. Additionally, the strong SJ staining in wildtype (B,B') is disrupted in Src42 (E,E'), but apical cell surfaces remain discernable. (C,C',F,F') Merged images of each genotype.

Src42[26-1]

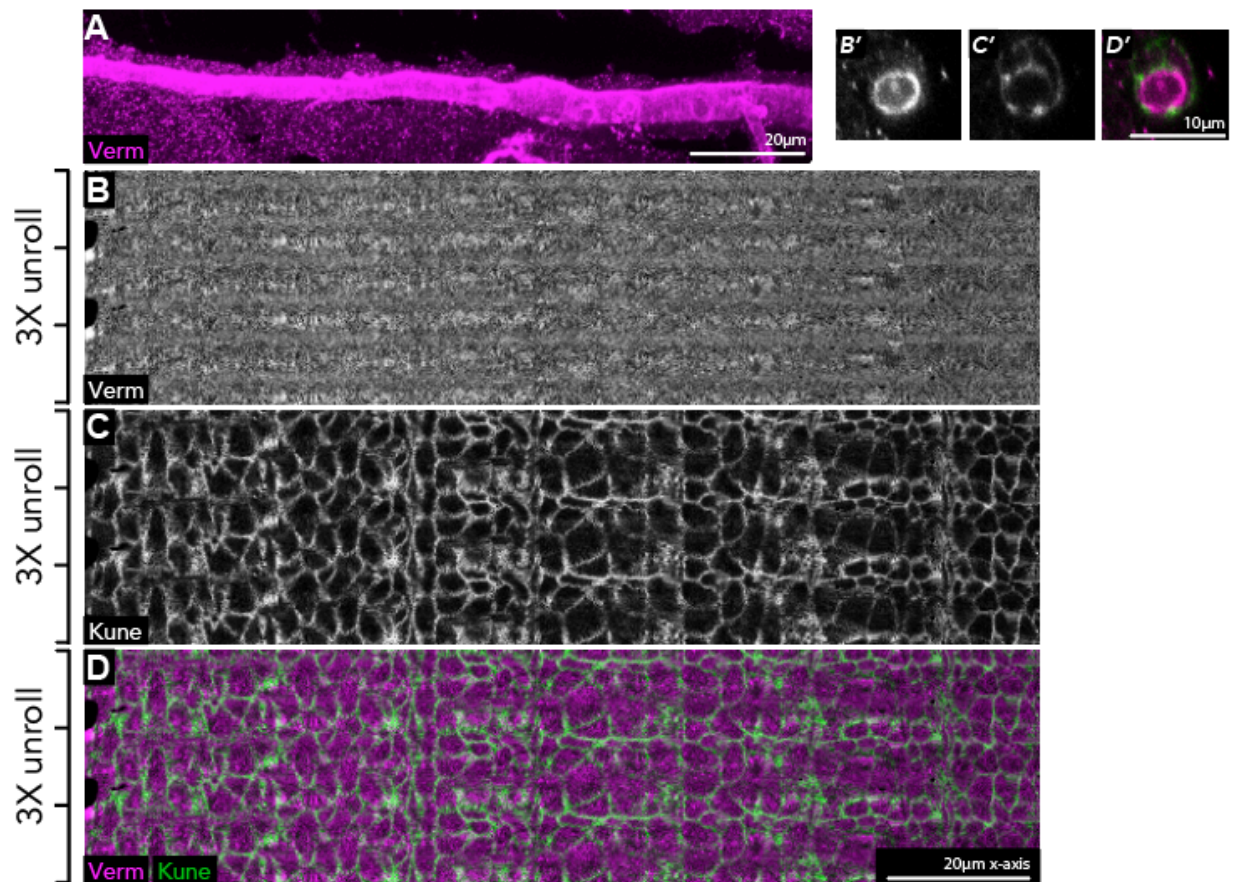


Fig. 4.3: Representative unrolled tube data for Src42[26-1] (n=9 tubes). (A) Partial max projection of the DT. (B) Unrolled Verm channel at R=-1. (C) Unrolled Kune channel at R=+1. (D) Merge. (B'-D') Representative cross-sectional (Y-Z) slices of the confocal images of their respective channels.

suggest a novel interaction of Src42 with SJ components which may also correlate to disruption of apical polarity factors. This possibility will be further discussed in Chapter 5.

Analysis of early stage tracheae in Src42 mutants shows unusual cell apical surface profiles

In addition to quantifying Src42²⁶⁻¹ embryos at stage 16, I measured these mutants at stage 14 to determine the origins of their mutant phenotypes. Src42 mutant tubes remain roughly the same length throughout development (Fig. 4.4A) on the individual segment level and nearly all of the increase in DT surface area (Fig. 4.4B) is due to radial expansion (Fig. 4.4C) and not tube elongation.

Analysis of Src42 apical cell surfaces yielded further interesting observations. First, the cell apical aspect ratio profile in stage 14 Src42 mutants appears to have a sinusoidal periodicity of two tracheal segments as opposed to one in all other mutants and wildtype (Fig. 4.4E, green line, which repeats in TC3-5; TC5-7; TC7-9). This periodicity appears to be rectified to a single segment by stage 16 (Fig. 4.4E, blue line). The cause

and biological significance for this difference in this particular mutant and developmental stage is unclear. Second, the cell orientation defects in the posterior DT where the sinusoidal pattern is disrupted (Fig. 4.1F) are not yet present at the early stage in Src42 mutants: the cell orientation profile is regularly sinusoidal (Fig. 4.4F, green line) except perhaps in the posterior-most DT segment. It is possible that disruption of cell orientation occurs in a wave beginning at the posterior, which coincides with the largest eventual increase in tube diameter. As Src42 is not known to directly regulate A-P patterning, one possible explanation is that the increase in tube diameter and/or surface area transiently causes misalignment of cells in Src42 mutants due to changes in the underlying aECM (see main text).

Src42[26-1]

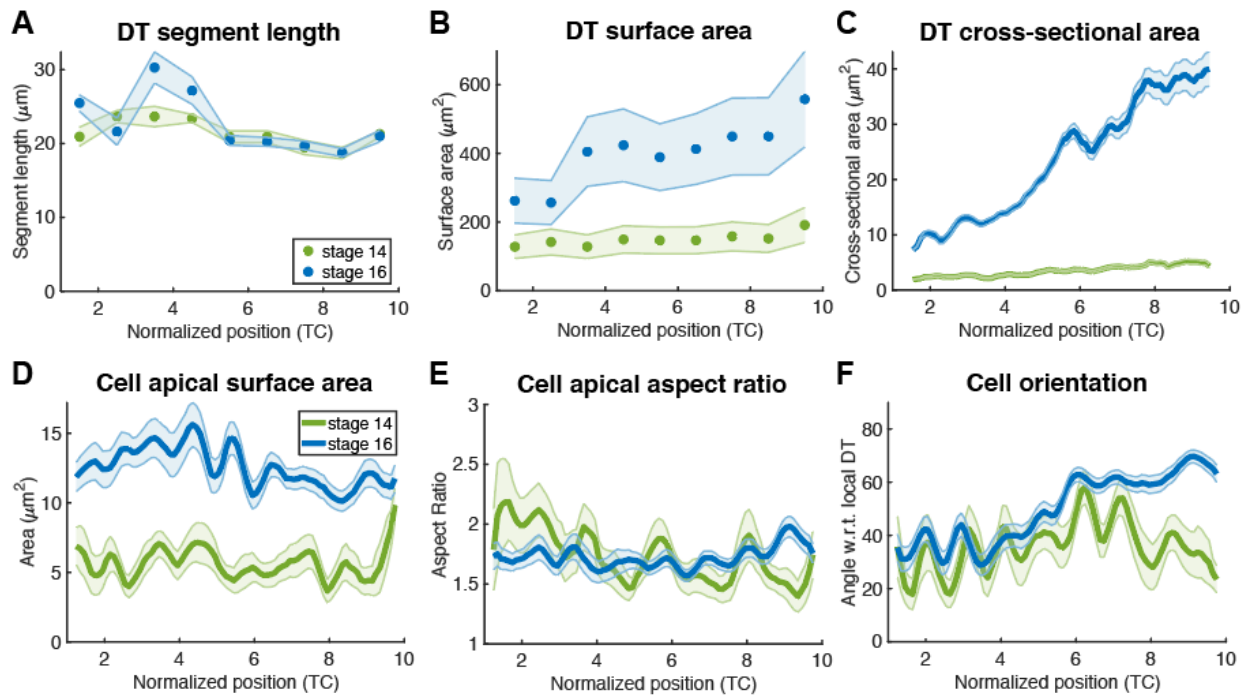


Fig. 4.4: Src42 tube and cell measurements at stages 14 and 16. ($n=6$ tubes each). DT measurements of (A) segment length, (B) segment surface area, and (C) cross-sectional area relative to the A-P position on the tube axis. Apical cell surfaces were measured for their (D) surface area, (E) aspect ratio, and (F) orientations.

Introduction to dDAAM

DAAM (Dishevelled-associated activator of morphogenesis) is a diaphanous-related formin known to interact with Src in mammals (Aspenstrom et al., 2006). In flies, dDAAM maintains taenidial folds and actin ring formation in the trachea (Ozturk-Colak et al., 2016), and like Src42, appears to act downstream of or in parallel to other tracheal size control pathways (Nelson et al., 2012).

This study was performed with two dDAAM alleles. dDAAM^{ex68} is a loss of function allele, resulting in shorter than normal actin cables that are cross-linked rather than parallel and causing the tracheae in these mutants to collapse (Matusek et al., 2006). dDAAM^K was made by my colleague in the lab, James Kwon, involving a 2-amino acid substitution in the actin binding domain of an otherwise wildtype allele that resulted in collapsed actin ring formation. As the effects of either allele on tube and cell measurements (Fig. 4.5) and unrolled images (Fig. 4.6) are consistent, they will be described together simply as dDAAM.

dDAAM likely functions in parallel to Src42

As shown previously (Nelson et al., 2012), dDAAM mutants are shorter than their wildtype counterparts (Fig. 4.5A), though they appear to compensate for the reduced axial length by increasing the tube radius, resulting in a total surface area that is indistinguishable from wildtype (Fig. 4.5B,C). Thus, both Src42 and dDAAM fall under the category of mutations that impact both tube length and diameter along with many SJ moments, the importance of which will be discussed in Chapter 5. Though it is a plausible hypothesis that tube surface area may also be independently regulated and preserved to maintain proper levels of nutrient and waste exchange, it is also possible that the consistency of surface area in dDAAM mutants is a coincidental byproduct of length and diameter change.

Unlike in Src42, dDAAM cell properties are mostly consistent with those of wildtype cells, with dDAAM^{ex68} cell size values being slightly smaller than in dDAAM^{IK} (Fig. 4.5D) due to greater inconsistency of Kune levels resulting in bias toward smaller cells (Fig. 4.6G, red arrowheads). More interestingly, the sinusoidal patterns observed in cell properties persist in dDAAM mutants for apical cell size (Fig. 4.5E) and orientation (Fig. 4.5F). The latter is particularly noteworthy, as Src42 cell orientations lose their sinusoidal

pattern in the posterior half of the DT (Fig. 4.1F). These results imply that dDAAM does not fully function downstream of Src42, but more likely functions in parallel to it. Furthermore, given that the relative axial locations of the peaks and troughs remain constant and with a periodicity of a DT metamere, it is reasonable to assume that there are segmental boundaries that restrict cell geometries, with one likely candidate being the fusion cell region.

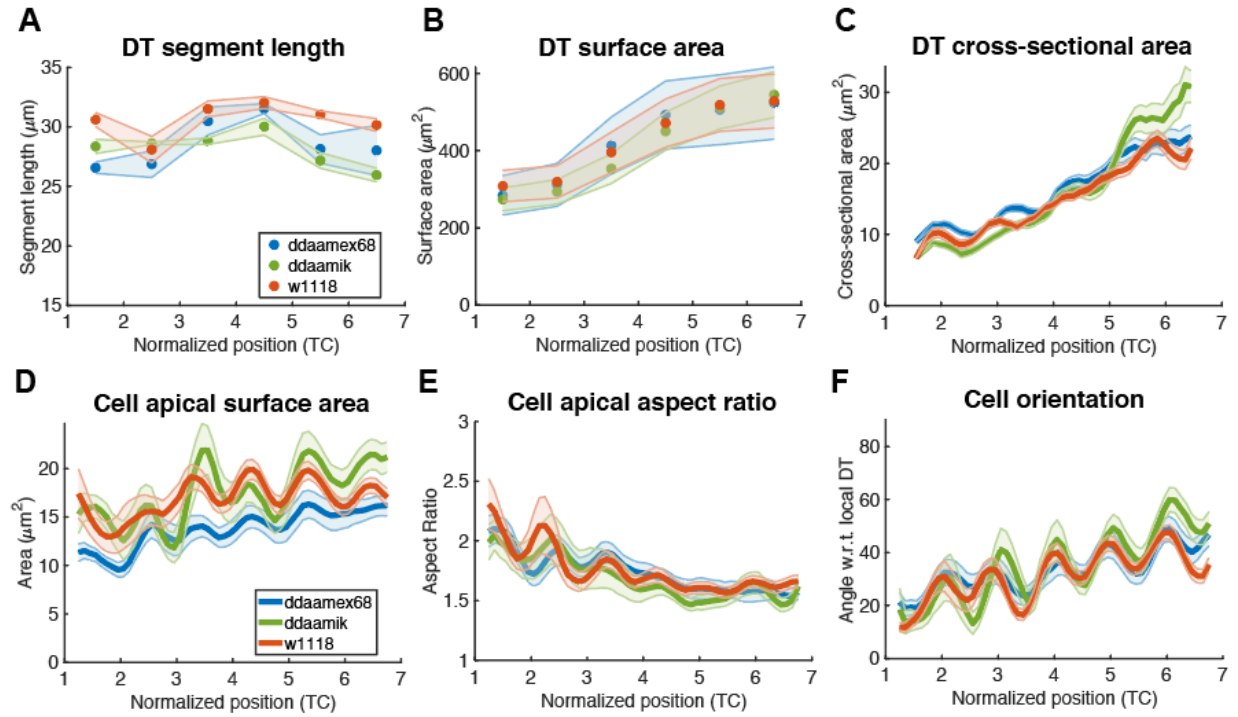
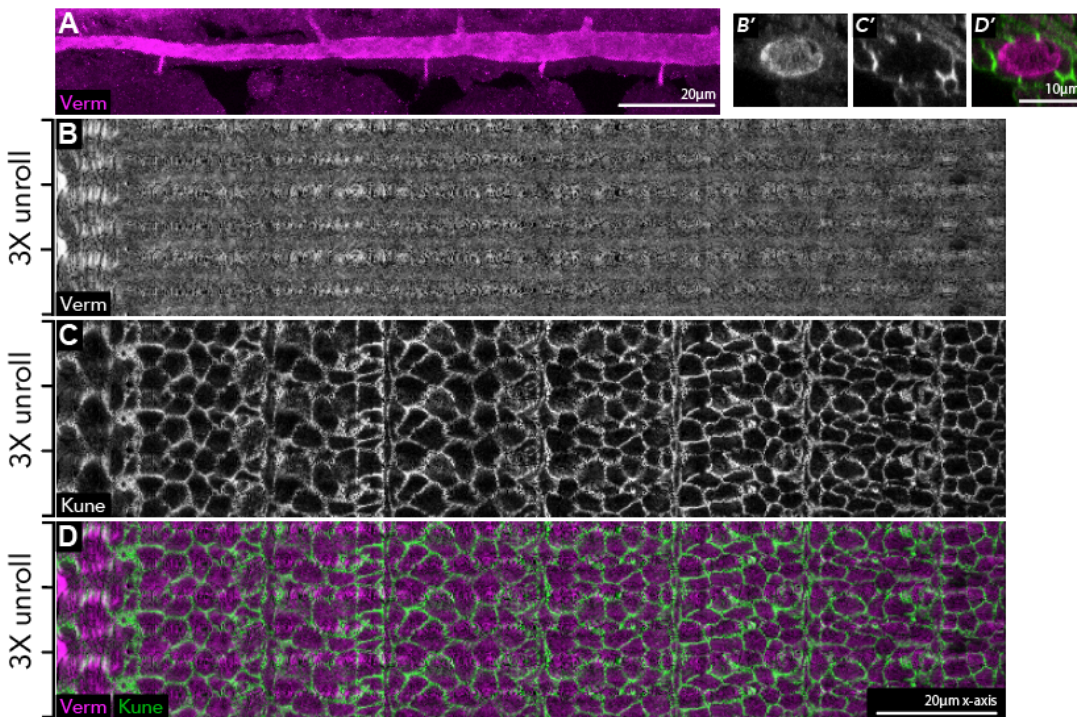


Fig. 4.5: dDAAM tube and cell measurements ($n=6$ tubes for each genotype). DT measurements of (A) segment length, (B) segment surface area, and (C) cross-sectional area relative to the A-P position on the tube axis. Apical cell surfaces were measured for their (D) surface area, (E) aspect ratio, and (F) orientations. Due to disruption of Verm staining in these mutants, data posterior of DT7 are not available.

dDAAM[IK]



dDAAM[ex68]

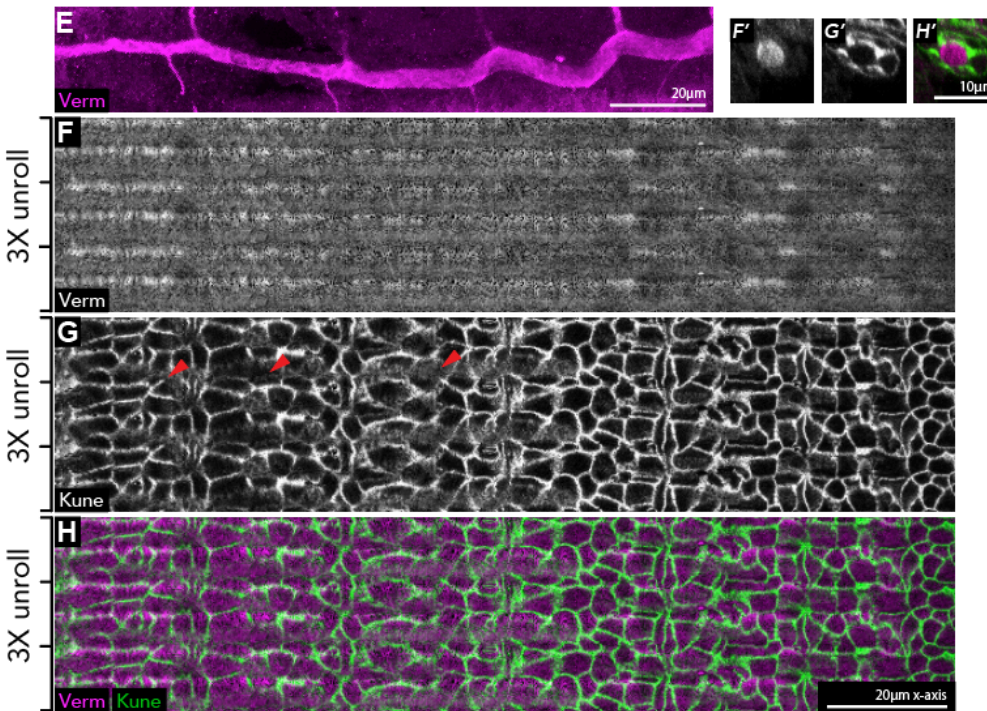


Fig. 4.6 (on previous page): Representative unrolled tube data for dDAAM mutant alleles (A-D) IK and (E-H) ex68 (n=4 tubes for each genotype; additional datasets are available but not analyzed). (A,E) Partial max projection of the DT. (B,F) Unrolled Verm channel at R=-1. (C,G) Unrolled Kune channel at R=+1. Red arrowheads in (G) denote regions of blurred Kune, which disrupts attempts at cell segmentation. (D,H) Merge. (B'-D',F'-H') Representative cross-sectional (Y-Z) slices of the confocal images of their respective channels.

The lumen disconnects from the apical surface in posterior dDAAM tubes

The lumen of the DT appears to pull away from the apical surface in the posterior DT of dDAAM mutants (Fig 4.7A,D), resulting in poor apical cell segmentation DT7-10 (cell recovery <40% in this region). Notably, Src42 mutants have a similar though much weaker effect that predominantly occurs in DT10 only, which does not interfere with cell quantification. Although most of the available dDAAM data were obtained from anterior of DT7, I was able to “segment” one dataset of dDAAM^{IK} that contained the full DT by manual correction of Verm. Plotting this particular posterior dataset (TC4-10) individually against other anterior datasets (TC1-7) does not cause any disagreements where they overlap (TC4-7) (data not shown), supporting the validity of these measurements. This dataset proved valuable as it not only allowed direct comparison of

QuBiT results to previously published work that only measured metamere 8 (Nelson et al., 2012), but revealed additional unique characteristics of dDAAM mutants.

As with the entire DT, metamere 8 alone is also shorter in dDAAM than in wildtype. This result is in agreement with QuBiT measurements on a single tube of dDAAM^{IK} (data not shown). Interestingly, although apical surface area and aspect ratio remained comparable to wildtype throughout the entire DT (Fig. 4.7D,E) and cell angles were well matched to wildtype in DT1-7, posterior (DT7-10) apical cell surfaces were oriented more orthogonally to the tube axis and the sinusoidal pattern was disrupted (Fig. 4.7F), reflecting the results seen in the posterior segments of Src42 mutants. These results suggest that dDAAM mutants, and to a lesser degree, Src42 mutants, have a greater disrupting effect on posterior patterning of the DT. Given that there is no clear boundary of effect and that dDAAM and Src42 are not known to be involved in anterior-posterior segmental patterning, it is more likely that the mutants themselves are not directly responsible for this phenomenon, but the way they physically influence or change tube architecture and/or lumen characteristics causes the lumen to retract when the diameter of the tube becomes too large. Thus, it is likely that dDAAM and Src42 do not directly specify tube parameters such as length or diameter but alter the physical forces and/or constraints that establish proper tube organization.

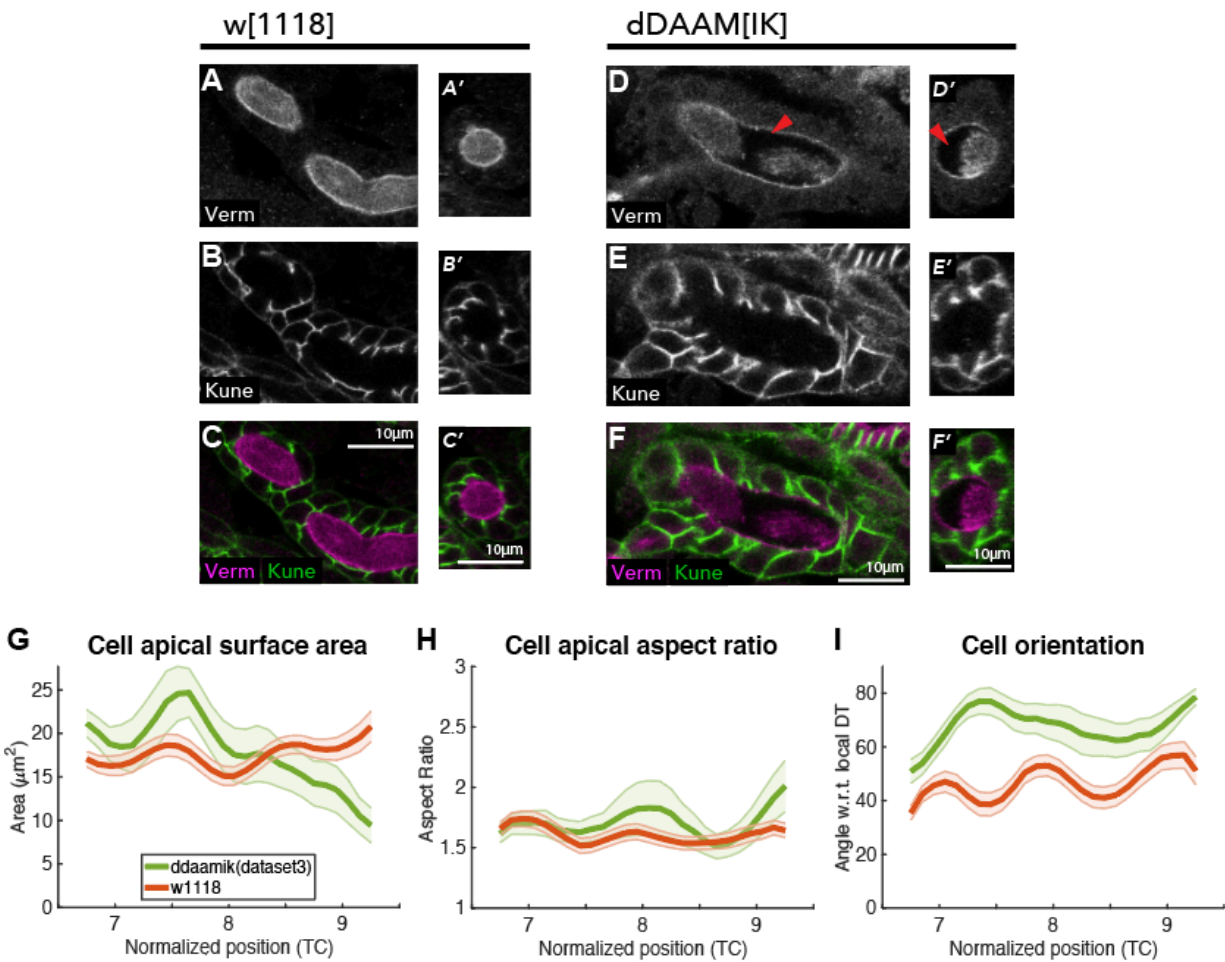


Fig. 4.7: The lumen dissociates from the apical surface in posterior of *dDAAM* mutants. Representative confocal slices in (A-C) *w¹¹¹⁸* (n=9 tubes) and (D-F) *dDAAM[IK]* (n=1 tube; n=19 cells per segment resulting in 68% cell recovery). (A'-F') Orthogonal cross-sections. (A,D) Verm staining. The detachment of the lumen from the apical surface in *dDAAM[IK]* is denoted by red arrowheads in (D,D'), while the (B,E) SJ marker remains unaffected. Despite this limitation, manual segmentation of this particular dataset yielded quantifiable results for apical cell surfaces, which were measured by (G) surface area, (H) aspect ratio, and (I) orientations and plotted against the average results for *w¹¹¹⁸*.

Chapter 5: Src42 as a central regulator: FoxO and the Na⁺/K⁺

ATPase

The work described in this chapter provides evidence that Src42 may have a more centralized role in tube size control through its interactions with many distinct pathways, including the transcription factor family, FoxO, and a septate junction component, the Na⁺/K⁺ ATPase. Y.-J. Kwon created the double mutant lines used in this work and collected most of the confocal data. The remaining confocal data, image processing, and data analysis were done by me.

Only the ATP α data in Figs. 5.5 and 5.6 have been published in: Yang, Li, Kwon, Mani, and Beitel. *Development* 2019 146: dev172759 doi: 10.1242/dev.172759. All work pertaining to FoxO and Nrv2 has been included here for a more thorough analysis and are in consideration for publication in the near future.

Introduction to FoxO

Forkhead-O (FoxO) is a subfamily of Forkhead transcription factors that is well-known to induce apoptosis in response to stress (Burgering and Kops, 2002; Kayal et al., 2010; Lu et al., 2013; Martins et al., 2016; Yamamura et al., 2006), but more recent work suggests FoxO has additional roles in the regulation of tube development. Overactivation of FoxO in mouse embryos is known to cause neural tube defects due to excessive apoptosis (Yang et al., 2013) as well as stimulate angiogenesis by activation of VEGF (Yoo and Kwon, 2013). The only FoxO ortholog in flies, dFoxO is known to be a direct activator of Yan, which regulates tracheal sprouting, similar to angiogenesis (Roukens et al., 2010).

FoxO has a high degree of conservation in mammals and flies in terms of both its functions and pathways. Notably, a small body of literature suggests FoxO acts in a conserved pathway with Src, which is known to regulate tube size (Chapter 4). Mouse fibroblasts treated with a Src-family-specific inhibitor leads to increased nuclear localization and activation of FoxO, suggesting FoxO acts downstream of Src. Likewise, in larval fatbodies of flies, Src42 loss-of-function mutations permit dFoxO localization to

the nucleus, where transcription of downstream targets of dFoxO is induced. The reverse is also true: ectopic activation of Src42 in the larval fatbody decreases nuclear dFoxO levels (Bulow et al., 2014). It is possible that Src42 may indirectly regulate dFoxO via derepression of Ras-activated Cnk (Laberge et al., 2005), which has previously been shown to directly phosphorylate FoxO in mammalian cell culture (Fritz et al., 2010). However, the connection between Src and FoxO remains largely uncertain.

As the mechanism by which Src42 regulates tube size is unknown, FoxO is an attractive potential transcriptional mechanism by which Src42 could perform its tube size control. To test the link between Src42 and FoxO, I processed both FoxO mutant and FoxO,Src42 double mutant data using QuBiT.

FoxO controls tube length but not cell parameters

FoxO mutants are slightly shorter than wildtype (Fig. 5.1A), with slightly reduced overall surface area (Fig. 5.1B) and minimal changes to tube diameter (Fig. 5.1C). As expected, FoxO mutant cells are smaller than their wildtype counterparts (Fig. 5.1D) such that the total tube surface area is in agreement with the cell apical surface area multiplied by the

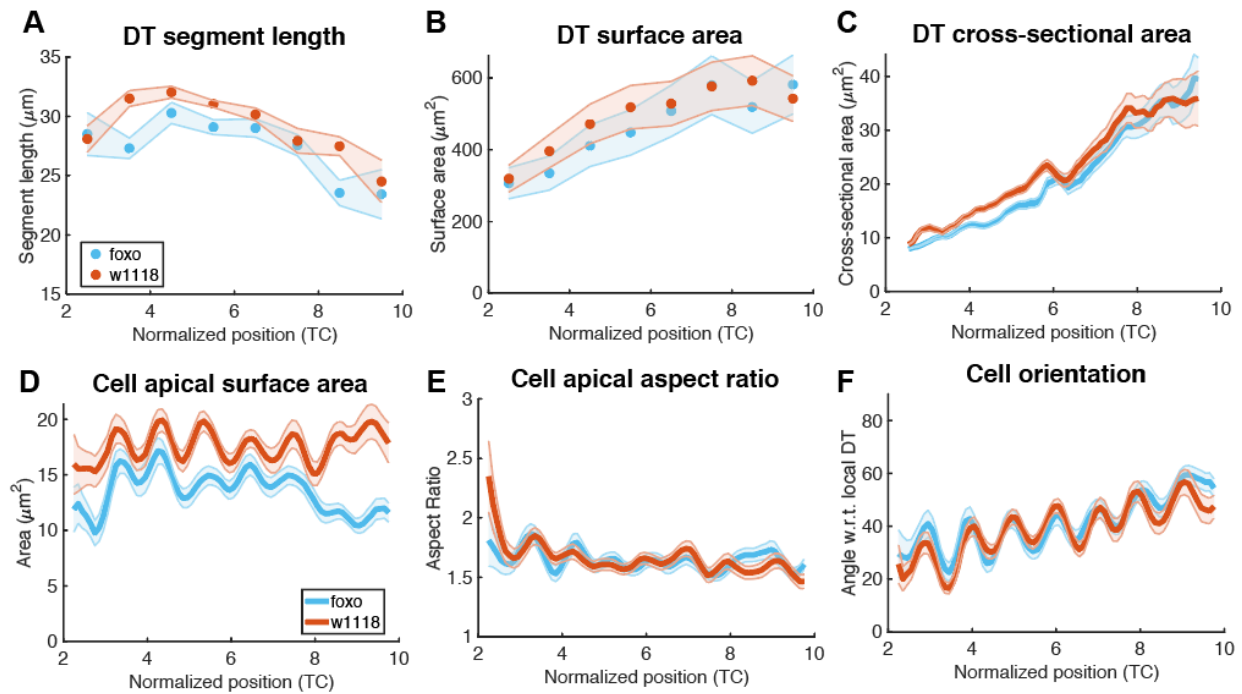


Fig. 5.1: FoxO tube and cell measurements. ($n=6$ tubes for each genotype). DT measurements of (A) segment length, (B) segment surface area, and (C) cross-sectional area relative to the A-P position on the tube axis. Apical cell surfaces were measured for their (D) surface area, (E) aspect ratio, and (F) orientations.

cell count. However, both cell apical aspect ratio and orientation parameters are nearly identical to wildtype (Fig. 5.1E,F), the latter of which will become important when comparing to Src42 below. Unrolling a FoxO tube results in similar cell characteristics to wildtype images (compare Fig. 5.2C,D to Fig. 3.9C,D). These data suggest that FoxO

FoxO

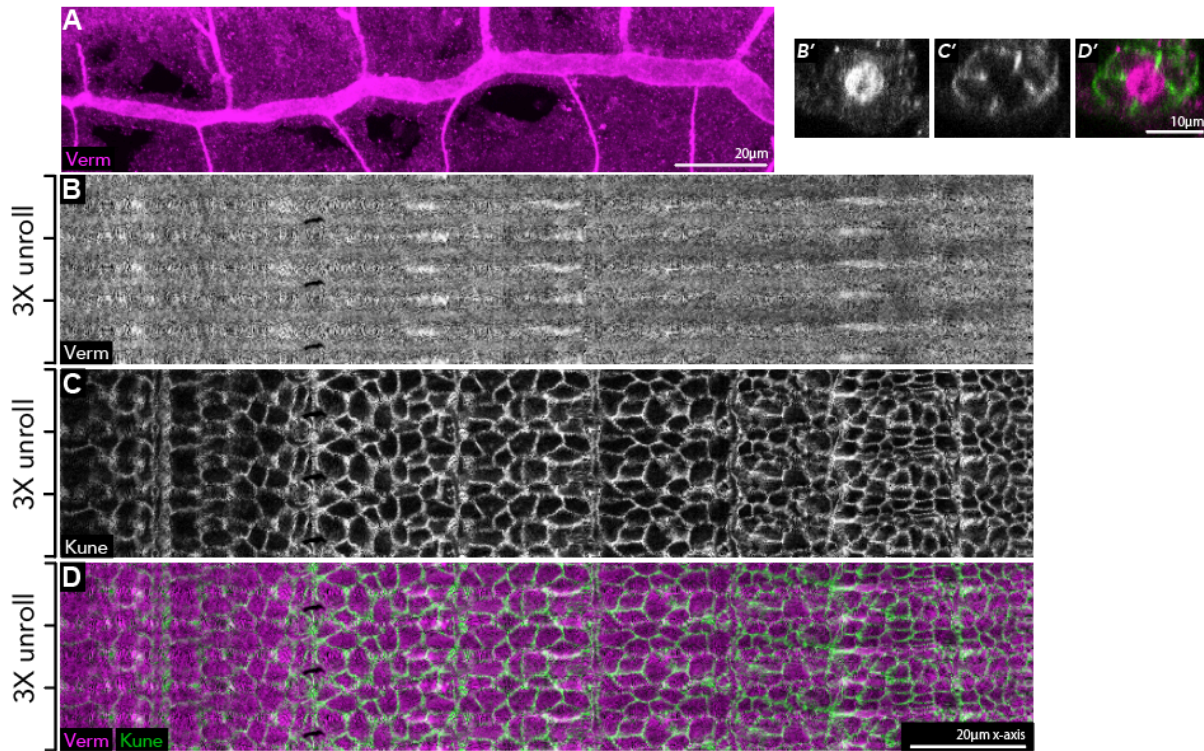


Fig. 5.2: Representative unrolled tube data for FoxO (n=3 tubes; additional datasets are available but not analyzed). (A) Partial max projection of the DT. (B) Unrolled Uif channel at R=-1. (C) Unrolled Kune channel at R=+1. (D) Merge. (B'-D') Representative cross-sectional (Y-Z) slices of the confocal images of their respective channels.

does not contribute to tracheal cell shapes, but it is likely that the mechanism by which FoxO regulates tube length results in a proportional downscaling of the apical cell surface.

Src42 functions downstream or in parallel of FoxO to regulate growth

I analyzed FoxO,Src42 double mutants to determine the epistatic interaction between FoxO and Src42 in tracheal size control. As FoxO is previously known to be downstream of Src42, the double mutant is expected to have FoxO characteristics. However, this does not appear to be the case in the fly trachea for the quantified parameters in this study. The double mutant has a tube length that is intermediate of either mutant alone ($p < 10^{-3}$) (Fig. 5.3A) and appears to exacerbate the increase in tube diameter of Src42 mutants (Fig. 5.3C). FoxO,Src42 double mutants also have increased apical cell surface areas, particularly between TC4 and TC6, compared to either mutant alone (Fig. 5.3D) though the reason for the localization of this effect is unclear. However, the most striking evidence is seen in apical cell orientations: FoxO,Src42 cell orientations are highly reminiscent of those of the Src42 mutant alone ($p = 0.14$ compared to Src42; $p < 10^{-20}$ compared to FoxO), with posterior dampening of the sinusoidal trajectory and increase in cell angle (Fig. 5.3F). Interestingly, while unrolled tubes of the Src42 mutant showed weak but consistent variability of the Kune marker in the posterior DT (Fig. 4.3C), the Kune marker in FoxO,Src42 double mutants was uniform (Fig. 5.4C). Additionally, the posterior lumen of the double mutants appears to retract from the apical surface (data not shown), similar to the effect seen in Src42 and, more strongly, in dDAAM. These

data support the hypothesis that Src42 may control tube architecture and/or luminal characteristics, through the FoxO pathway, but in contrast to previously established epistatic relation, these data suggest that Src42 is likely to function downstream or in parallel of FoxO in tracheal size control.

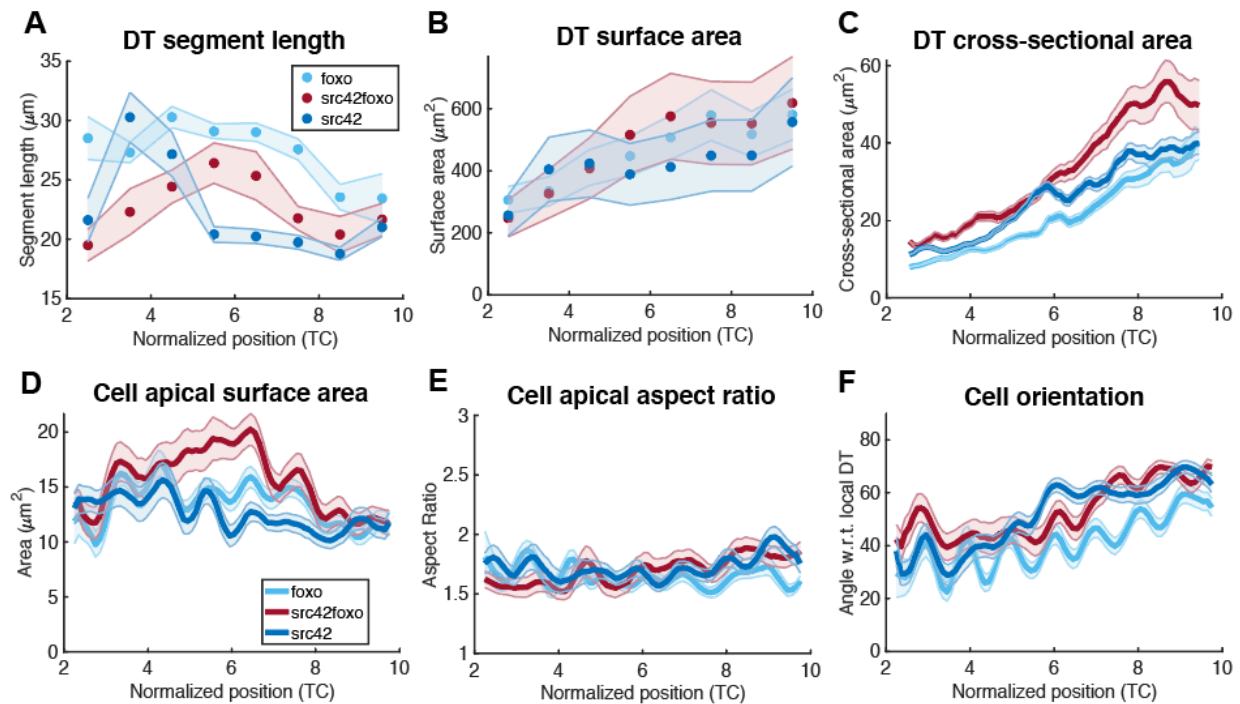


Fig. 5.3: FoxO,Src42 double mutant tube and cell measurements. (n=7 tubes). DT measurements of (A) segment length, (B) segment surface area, and (C) cross-sectional area relative to the A-P position on the tube axis. Apical cell surfaces were measured for their (D) surface area, (E) aspect ratio, and (F) orientations.

FoxO,Src42

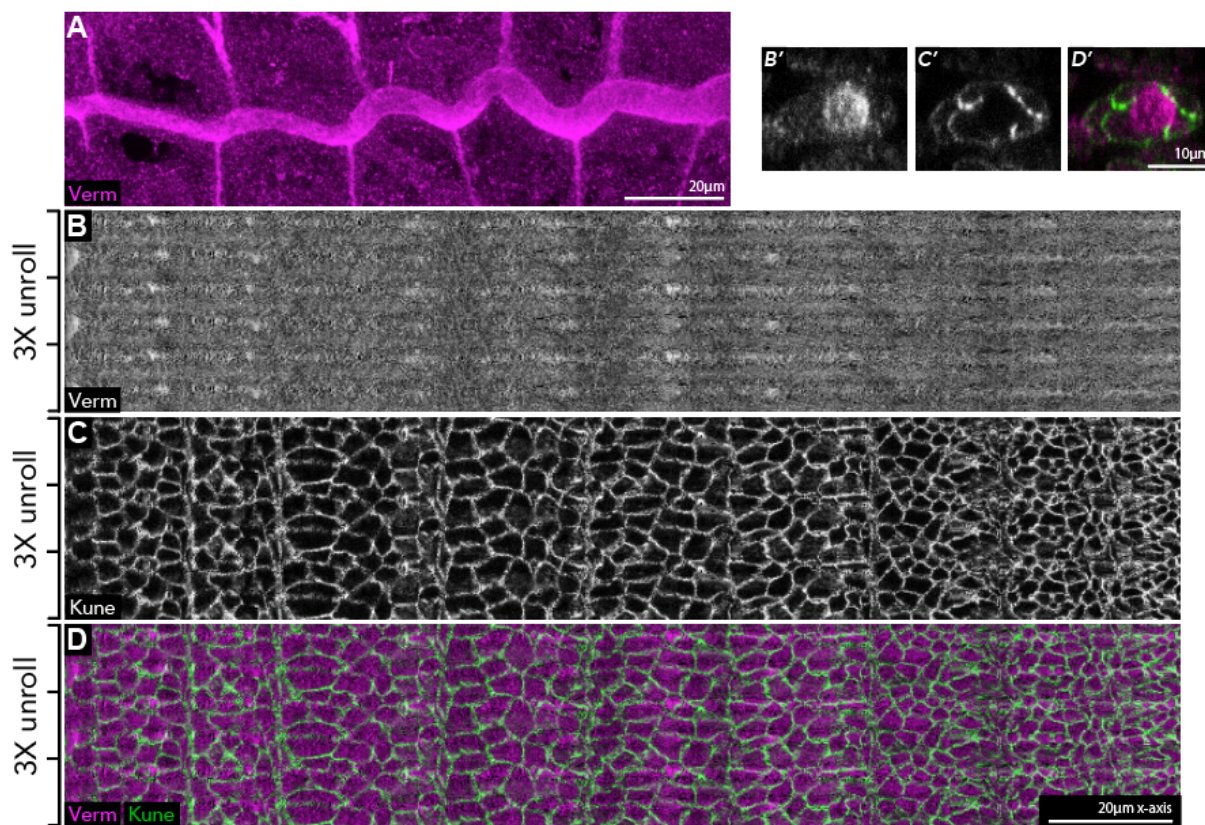


Fig. 5.4: Representative unrolled tube data for FoxO/Src42 (n=4 tubes; additional datasets are available but not analyzed). (A) Partial max projection of the DT. (B) Unrolled Uif channel at R=-1. (C) Unrolled Kune channel at R=+1. (D) Merge. (B'-D') Representative cross-sectional (Y-Z) slices of the confocal images of their respective channels.

Introduction to the Na⁺/K⁺ ATPase

The Na⁺/K⁺ ATPase is presented in many textbooks as a membrane-bound ion transporter that establishes electrochemical gradients that are essential to many biological processes (reviewed in (Skou and Esmann, 1992)). However, many recent studies have focused on its non-pumping functions, most notably the role of the ATPase alpha subunit in signal transduction via its interactions with Src in mammalian systems and cell cultures (reviewed in (Cui and Xie, 2017)), as evidenced by a 20-amino acid sequence on the ATPase that directly binds and inhibits the Src kinase domain and functions independently of the transporter (Lai et al., 2013). This “ATPase-Src receptor” is speculated to regulate Src-dependent GPCRs, with downstream effects on tubular systems such as kidney development (Dvela-Levitt et al., 2015; Li et al., 2011).

In *Drosophila*, the Na⁺/K⁺ ATPase has a non-pumping function in septate junction (SJ) formation (Paul et al., 2007) and a redundant role in apical/basal polarity (Laprise et al., 2010). Mutations in the alpha subunit of the ATPase (ATP α), along with other SJ components including Yurt, Coracle, and Neurexin-IV, restrict tracheal size through inhibition of Crumbs (Laprise et al., 2010). The ATPase beta subunit, which is essential for membrane targeting as well as overall functionality of the ATPase, appears to be just

as important for regulating tube development. In flies, mutations in the beta subunit (Nrv2) have also been reported to result in overelongated tracheae (Paul and Beitel, 2003; Paul et al., 2003).

The $ATP\alpha$ mutant disrupts localization of the apical marker Uif

I examined a previously uncharacterized CRISPR mutation in the Na^+/K^+ ATPase α -subunit, developed by my colleague in the lab, James Kwon. This new allele, $ATP\alpha^{LNFS}$, results from a frame-shift mutation in the exon encoding the long isoform of $ATP\alpha$, which is thought to contain the SJ activity (Paul et al., 2007). Confirming this hypothesis, SJs are disrupted in the $ATP\alpha^{LNFS}$ homozygotes, as evidenced by reduced Kune levels and failure of Kune to localize to the apical region of the lateral membrane (Fig. 5.6C,C'). As expected for a SJ mutation, $ATP\alpha^{LNFS}$ increases tracheal tube length up to 30% ($p < 0.01$, Fig. 5.5A), resulting in the tubes buckling and following a convoluted path between transverse connectives (Fig. 5.6A). Tube cross sectional area is generally increased compared to WT ($p = 0.01$), but the diameter at fusion cells is not increased, conferring a saw-tooth-like appearance to the cross-sectional area graph (Fig. 5.5C) that would be expected from the sausage-link appearance of many SJ mutant trachea, including $ATP\alpha$ and *wurst* (Paul and Beitel, 2003).

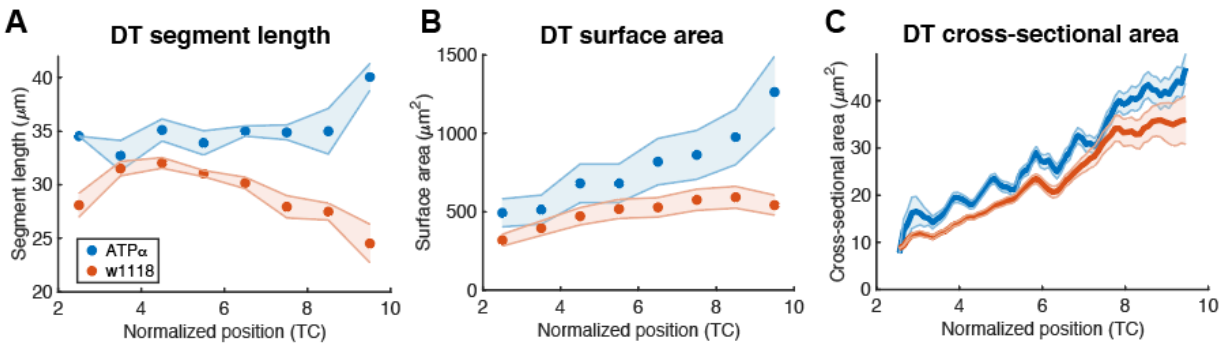


Fig. 5.5: $ATP\alpha$ tube data ($n=6$ tubes). DT measurements of (A) segment length, (B) segment surface area, and (C) cross-sectional area relative to the A-P position on the tube axis. Apical cell surfaces were measured for their (D) surface area, (E) aspect ratio, and (F) orientations. Due to disruption of septate junctions in these mutants, cell data is not available.

Unrolling of $ATP\alpha^{LNFS}$ mutant tubes reveals effects of Na^+/K^+ ATPase mutations that had not been previously observed. Uif staining in $ATP\alpha^{LNFS}$ mutants was markedly different than in WT: whereas in WT there are occasional areas where Uif is locally reduced, Uif-deficient regions in $ATP\alpha^{LNFS}$ mutants were larger and more frequent (Fig. 5.6B). Interestingly, these regions correspond to the surfaces of the trachea that are furthest away from the outer epidermis of the embryo and were notably confined to regions between the brighter Uif bands. The disruption of the apical surface marker Uif in an $ATP\alpha$ single mutant extends our previous results regarding the role of the Na^+/K^+

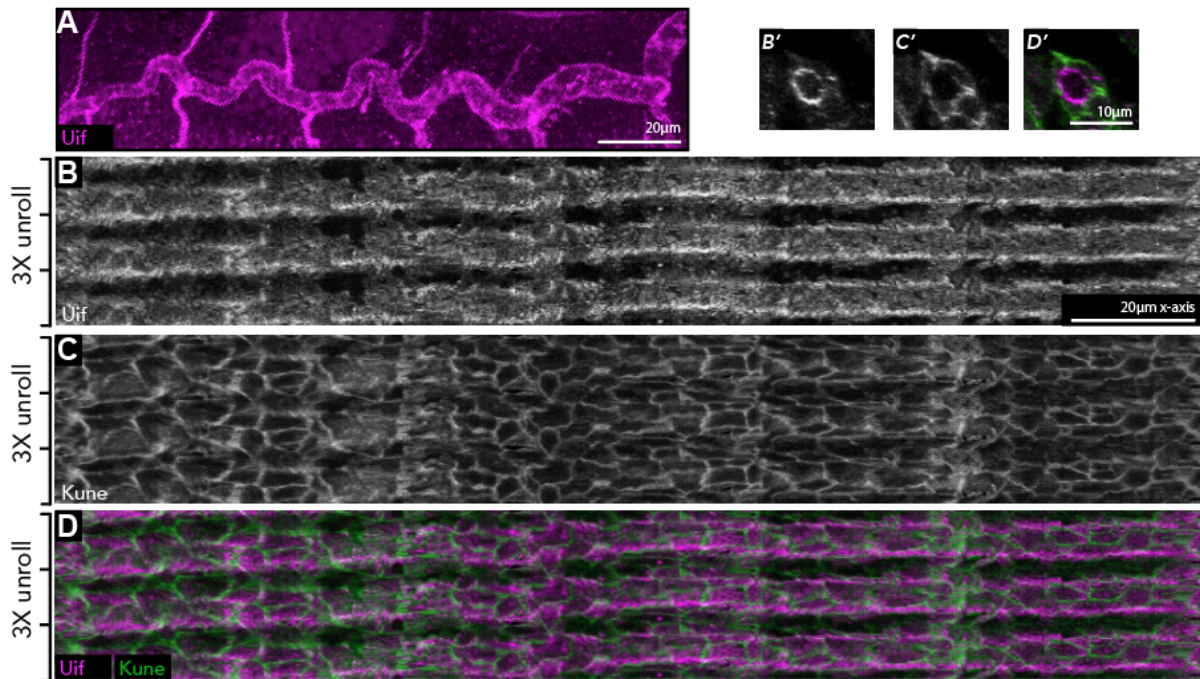
ATP α [LNFS]

Fig. 5.6: Representative unrolled tube data for ATP α [LNFS] (n=6 tubes). (A) Partial max projection of the DT. (B) Unrolled Uif channel at R=-1. (C) Unrolled Kune channel at R=+1. (D) Merge. (B'-D') Representative cross-sectional (Y-Z) slices of the confocal images of their respective channels.

ATPase in polarity (Laprise et al., 2009), and suggests that the polarity function of the Na⁺/K⁺ ATPase is not entirely redundant with that of Yurt. These findings also further illustrate that the tube unrolling function of QuBiT, a function not available in general epithelial analysis packages, can help identify patterns not readily evident from

conventional confocal slices or 3D projections and can function independently of 3D quantification modules.

Nrv2 tubes appear equally convoluted as ATP α tubes, but are much shorter

The ATPase beta subunit mutant predictably appears similar to the alpha subunit (compare Fig. 5.6A to 5.8A), but my quantitation results using QuBiT show a key difference. Although both ATP α and Nrv2 mutant tracheae appear convoluted and long, only the Nrv2 mutant has shorter DT length than wildtype (Fig. 5.7A), in direct contrast to previous results (Paul et al., 2003). However, it should be noted that these DT lengths were not normalized to embryo length, which may result in similar DT:embryo ratios. Nevertheless, in accordance with reduced DT length, DT surface area in Nrv2 mutants is also reduced to near wildtype levels (Fig. 5.7B). However, the cross-sectional area profile of Nrv2 remains strikingly similar to that of ATP α , with both the same periodicity that is absent in wildtype and a similar numerical difference of approximately 25% increase in area (Fig. 5.7C). Unrolling Nrv2 mutants yielded similar results as ATP α mutants, including loss of Uif in bands running parallel to the tube axis (Fig. 5.8B) and weak septate junction marker signals (Fig. 5.8C) that interfered with quantifying apical cell parameters.

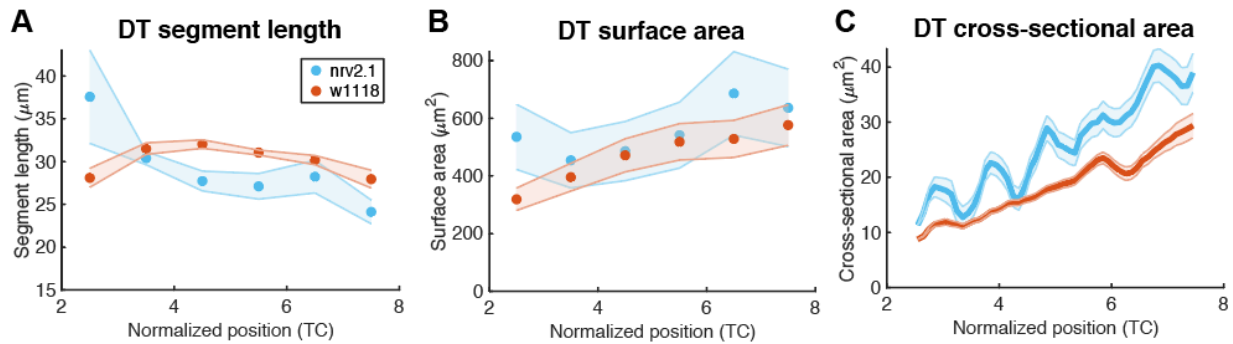


Fig. 5.7: Nrv2 tube data (n=6 tubes). DT measurements of (A) segment length, (B) segment surface area, and (C) cross-sectional area relative to the A-P position on the tube axis. Apical cell surfaces were measured for their (D) surface area, (E) aspect ratio, and (F) orientations. Due to disruption of septate junctions in these mutants, cell data is not available.

These results have several implications. First, since both ATP α and Nrv2 appear to have equally convoluted DTs, but only ATP α tubes are longer than wildtype, it is likely that tube length and tube shape (as determined by tortuosity) are not linked parameters. Second, the periodic nature of the cross-sectional area in both alpha and beta subunit mutants where the troughs coincide with fusion cell boundaries suggest fusion cells either play an important role in maintaining proper tube size or are simply inflexible structures that locally confine the shape and position of the DT. Finally, the difference in tube length suggests that the alpha and beta subunits of the Na⁺/K⁺ ATPase have differential roles in regulating tube and/or embryo size. As it is known that tube length

and diameter are two separately controlled parameters in the DT, it is possible that the alpha subunit behaves similarly to other known SJ components to control both length and diameter, while the downstream effectors of the beta subunit are likely to be other

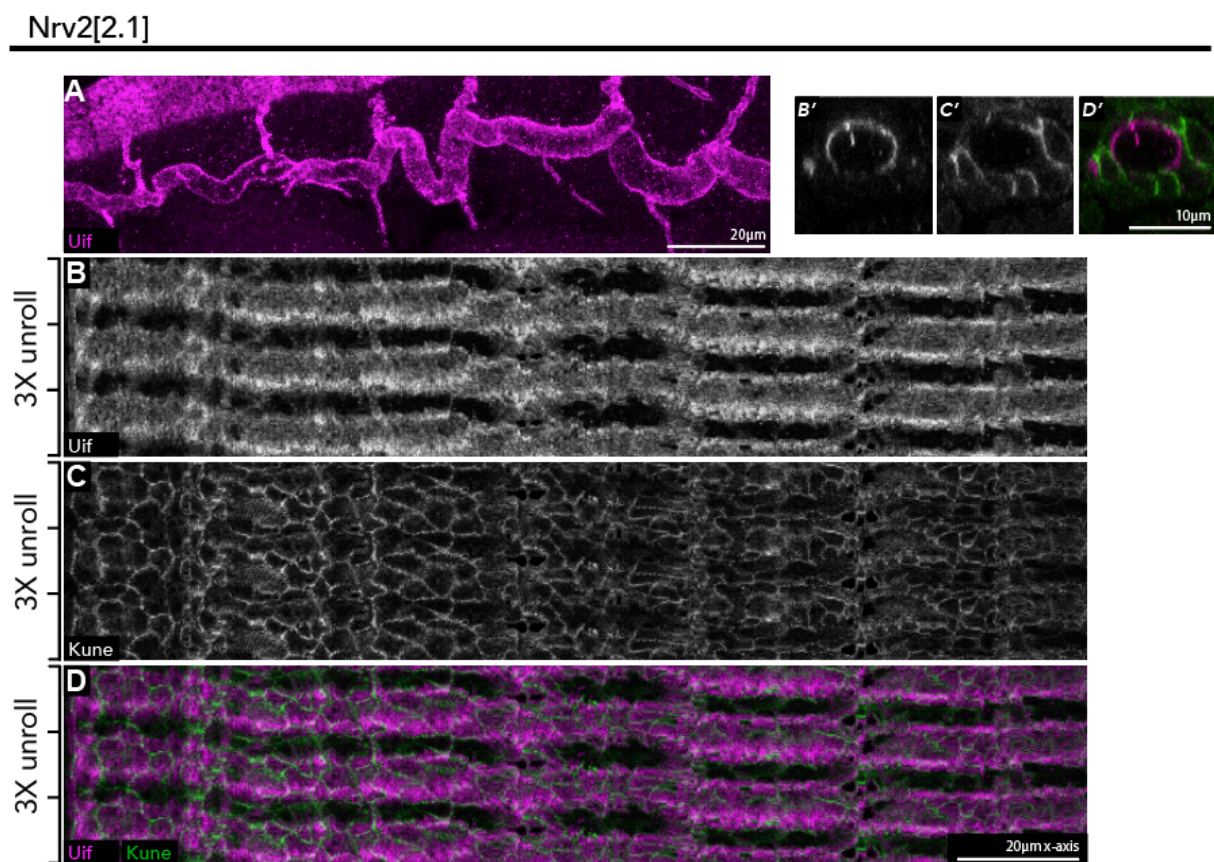


Fig. 5.8: Representative unrolled tube data for Nrv2[2.1] ($n=6$ tubes). (A) Partial max projection of the DT. (B) Unrolled Uif channel at $R=-1$. (C) Unrolled Kune channel at $R=+1$. (D) Merge. (B'-D') Representative cross-sectional (Y-Z) slices of the confocal images of their respective channels.

targets, such as chitin production, that only impact tube diameter but not length. This possibility aligns with the alpha subunit's known direct interaction in other organisms with Src42, which also modifies both tube length and diameter (Chapter 4).

Analysis of cells in the Nrv2,Src42 double mutant suggests Src42 is downstream of Nrv2

Like for FoxO,Src42, I analyzed Nrv2,Src42 double mutants to determine the epistatic interaction between Nrv2 and Src42 in tracheal size control. DT length in the double mutant appears to be an intermediate of either mutant alone, although it is more consistent with that of Src42 ($p = 0.035$ compared to Src42; $p < 0.01$ compared to Nrv2) (Fig. 5.9A). Additionally, the double mutant much more closely resembles Src42 in terms of both tube surface area ($p = 0.45$) (Fig. 5.9B) and cross-sectional area ($p = 0.08$) (Fig. 5.9C), which provides compelling evidence that Src42 functions downstream of Nrv2.

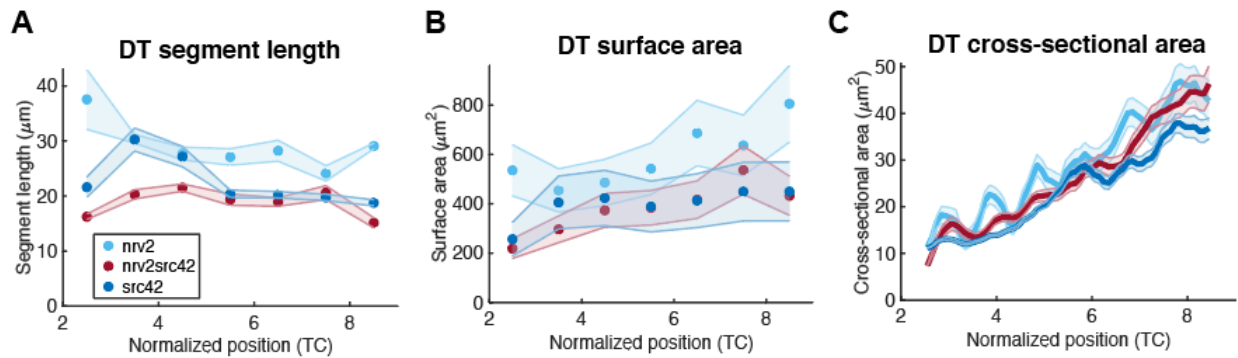


Fig. 5.9: Nrv2,Src42 tube measurements (n=8 tubes for Nrv2,Src42 and n=6 for others). DT measurements of (A) segment length, (B) segment surface area, and (C) cross-sectional area relative to the A-P position on the tube axis.

Although cells were difficult to recover in septate junction mutants such as Nrv2, I was able to segment a small amount of cells (20% recovery) from 6 Nrv2 mutant tubes and 8 Nrv2,Src42 double mutants. Anterior cells generally segmented worse than posterior cells due to the narrower tube magnifying any defects in the Kune marker. Despite the increased variation in apical surface area (Fig. 5.10A), the cell apical aspect ratio of Nrv2,Src42 mutants consistently showed disruption of the aforementioned A-P sinusoidal pattern and were elevated to Src42 single mutant levels (Fig. 5.10B). Likewise, while Nrv2 cell angles were generally larger than those of wildtype (data not shown), the Nrv2,Src42 cell angles were larger still, coinciding with Src42 single mutants (Fig.

5.10C). Although the data are not conclusive, preliminary Nrv2,Src42 double mutant data are in agreement that Src42 is a central regulator of tube size and that Src42 functions downstream of Nrv2 and potentially other SJ components.

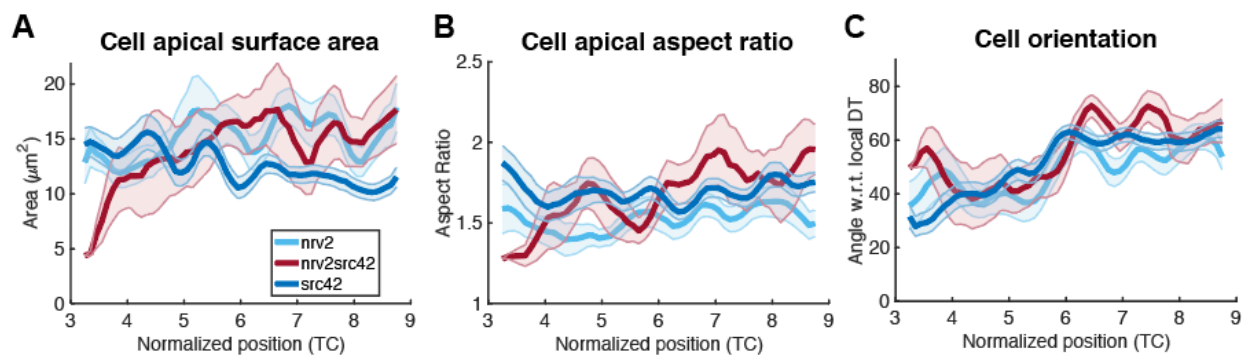


Fig. 5.10: Preliminary Nrv2,Src42 cell measurements. (n=8 tubes for Nrv2,Src42; n=6 tubes for others). Apical cell surfaces were measured for their (A) surface area, (B) aspect ratio, and (C) orientations. Due to disruption of septate junctions, the cell recovery counts in Nrv2 and Nrv2,Src42 were low (approximately 20% of all cells compared to 75% recovery in Src42).

Chapter 6: Discussion

I developed a Matlab-based computational program called QuBiT specifically targeted at measuring various physical properties of biological tubes. To demonstrate the functionality of QuBiT, I validated previously reported results in wildtype and Src42 tracheae, the only two conditions where this data were available. Analysis of the fly trachea using QuBiT also revealed many unexpected findings, including cell parameter gradients that oscillate with tracheal-segment periodicity, non-uniform and cell-autonomous localization of an apical signaling molecule, and further evidence of cell rearrangement during tracheal elongation. While many of these findings and their implications have been discussed above, this chapter includes some of the more speculative tube size control mechanisms that have arisen from this work.

Fusion cells restrict cell geometries and tube shape

Fusion cells appear to be regulated by a mechanism distinct from tube length and diameter control. This is evidenced by mutations where the rest of the DT expands in diameter, but the fusion regions do not, resulting in bulgy tubes that appear to be pinned down at fusion regions (Fig. 3.2). As the fusion cell regions are very close to DB and TC branch points, it is possible that these branches, which extend into surrounding tissues that are not disrupted by bulgy trachea mutants, anchor the DT in precise locations, perhaps even by anchoring fusion cells. However, if this anchoring theory were true, it would be very likely for cells intersecting the branch to adopt regular shapes, which is not the case, at least at the apical surface (Fig. 3.9B). This has implications on the geometries of its neighboring cells as well as the tube architecture.

Uif is an apical component whose localization also relies on D-V patterning

Tube unrolling at the apical surface revealed a non-uniform banding pattern of the apical transmembrane protein Uif (Fig 3.9B), which was increasingly disrupted in both Src42 (Fig. 4.2) and Na⁺/K⁺ ATPase mutants (5.6B, and 5.8B). Overlaying the Uif on a septate

junction marker, Kune, revealed that these bands were not simply an artifact of the unrolling algorithm, an observation confirmed in the raw orthogonal slice views of the corresponding image stacks. Interestingly, the bands of increased Uif did not necessarily coincide with individual cells, as would be expected if certain cells stochastically produced greater or lesser amounts of Uif (Fig. 3.9D, insets). Additionally, the elevated Uif bands were not randomly located: they were aligned with the DB and TC exits (Fig. 6.1). Bands of increased Uif are visible in the unrolled images of the hindgut (Fig. A.1B and B', yellow arrowheads) and do not coincide with the other visualized cellular landmark, the boundary cell region, which further supports apical Uif localization being both cell-autonomous and externally regulated.

As Uif levels remain constant along the A-P axis, it is likely that Uif localization is either regulated by the branch intersections themselves or by external proximal-distal polarity signals, two unprecedented hypotheses. However, there is no previously documented mechanism to describe branch points creating bands of elevated signal in a line between adjacent nodes, and it is unlikely that branches alone are sufficient to perform this function when even the local cell shapes appear largely unaffected. Given that the missing Uif bands are consistently occur on the proximal side of the DT, it is likely that proximal-distal polarity regulates Uif through an unknown mechanism. However, a more

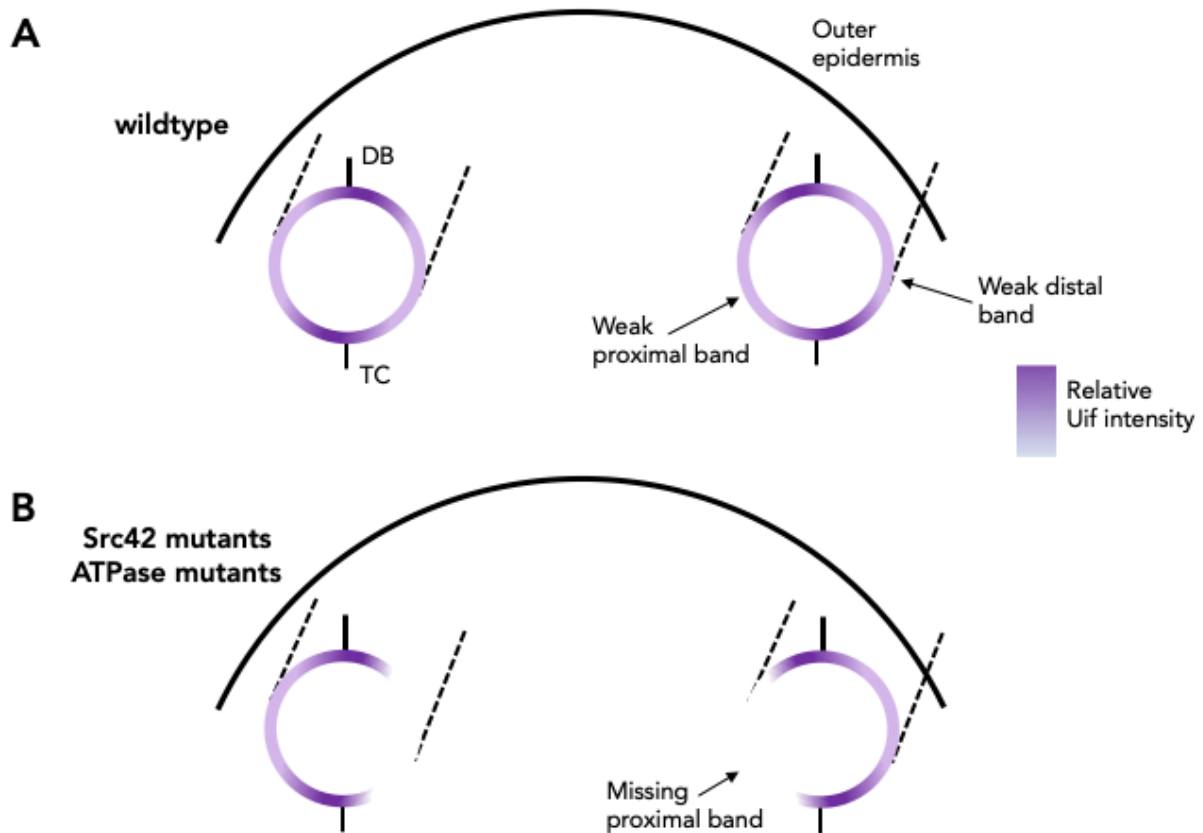


Fig. 6.1: Schematic of Uif banding in the DT. Purple rings denote Uif intensity on the apical surface. (A) Strong bands of Uif coincide with DB and TC branch points in wildtype embryos, whereas (B) only one of the background bands of Uif is missing in both ATPase and Src42 mutants. The directionality of the missing Uif bands in ATPase and Src42 mutants suggests that the transmembrane apical marker is regulated by proximal-distal patterning in a cell-autonomous manner. Up-down is dorsal-ventral; front-back is anterior-posterior.

complex hypothesis is required to account for the weak distal bands that are present in wildtype embryos and unaffected in ATPase and Src42 mutants (Fig. 6.1). While these data have illuminated a phenomenon that has not previously been recognized, further study is required to understand the mechanisms of its origin.

Apical cell surfaces are transiently reshaped due to the flow of the aECM / Tube expansion correlates with cell rearrangement

The simple expansion model (Fig. 3.3-3.4) of the DT showed that inflation of the tube without changing any other parameters was sufficient to predict the observed apical cell shape changes as determined by the quantifiable parameters of size, aspect ratio, and orientation (Fig. 3.5). Since the simple expansion model requires no cell migration and/or rearrangement, it was surprising when analysis by QuBiT found changes in the number of cells per cross-section from pre- to post-inflation, which can only be explained by cell rearrangement (Fig. 3.8). Additionally, since these cells retained the same shape parameters as predicted by simple expansion, at first glance it would seem that rearrangement is “extra” work for the tracheal system with little benefit.

In accordance with the minimum total potential energy principle, it would follow that this “extra” energy from cell movement must either be beneficial over stationary cells or be a result of a response to external forces. One possible explanation that supports the latter conjecture is that tracheal cells respond to the flow of the viscoelastic aECM during inflation, resulting in slightly different arrangements simply due to the lengthening of the tube. It would also imply a degree of inertia: cells prefer to retain their shapes and instead can be rearranged similar to floor tiling or bricks on a wall, in which various patterns of tiles yield the same overall result (conceptualized in Fig. 6.2). This idea is also in line with the relative absence of axial forces on DT cells, where cells appear to simply “sit” on the tube surface (Affolter and Caussinus, 2008). To further develop this idea of cell shapes transiently adhering to aECM flows to minimize energy, additional data on cell rearrangements in chitin mutants *Serp* and *Verm* are necessary, as well as live imaging to definitively show cell rearrangement occurs.

Src42 as a central regulator of tube size

Analysis using QuBiT has provided evidence of Src42 as a central regulator of tube size, but both its molecular signaling and/or force mechanisms of this regulatory function

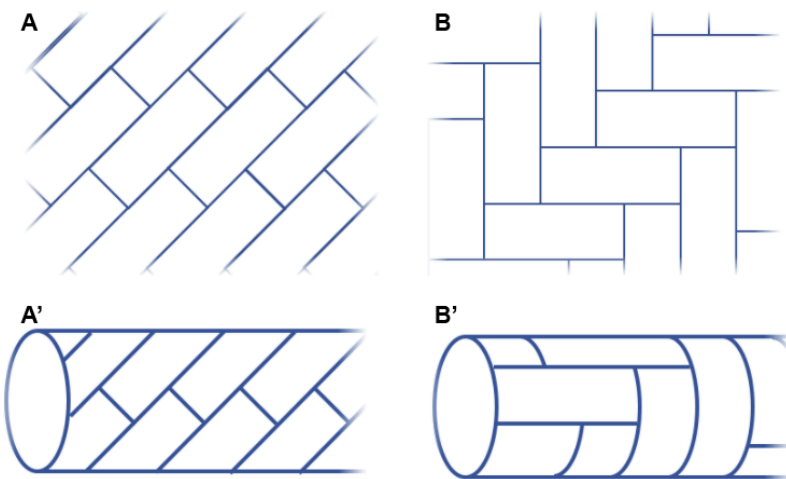


Fig. 6.2: Concept: Various arrangements of a set of building blocks can result in the same macroscopic structure. The same simple rectangular block models a cell surface in all diagrams. (A,B) Two different “cell” arrangements. While size, aspect ratio, and average orientation of these “cells” remain constant, the number of cells per cross-section changes, reflecting a difference in cellular arrangement. (A',B') A sheet of each pattern can be folded into a cylinder to model the DT while the relative cell parameters remain unchanged.

remain largely unexplored. Due to its known interactions with other highly conserved pathways, including FoxO and the Na^+/K^+ ATPase in other organisms, it is conceivable that its tube size regulation function is also conserved. Interestingly, while FoxO has been shown to regulate tube length, no previous studies have suggested that it follows

known tube length control mechanisms such as apical expansion or matrix modification, suggesting that FoxO, and by extension, Src42, has additional unknown means of regulating tube size.

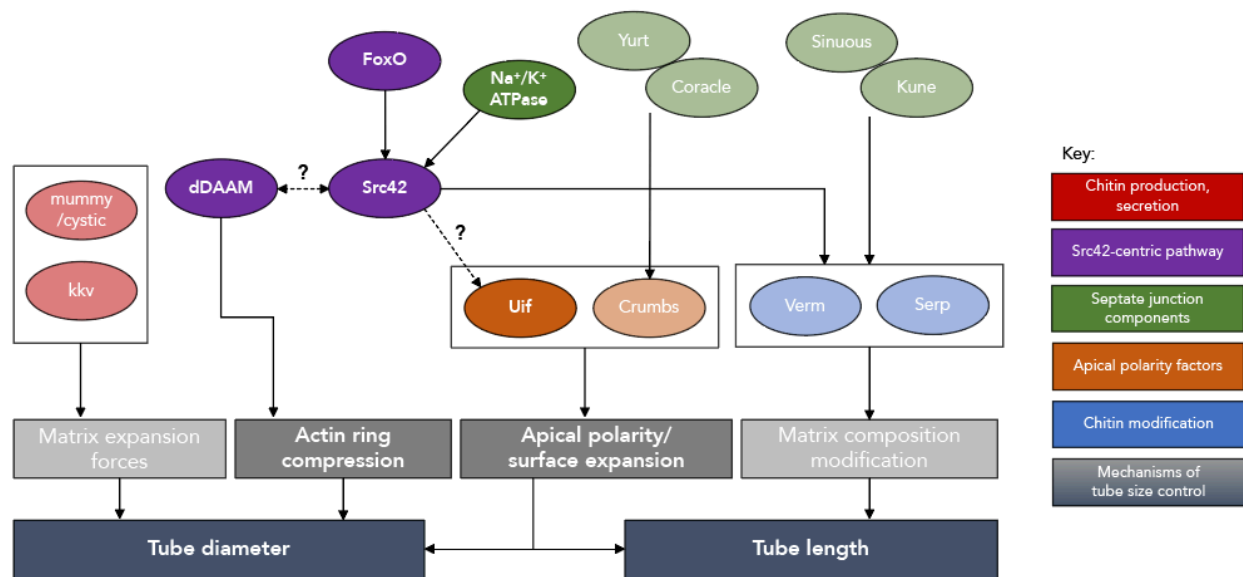


Fig. 6.3: Molecular pathways and mechanisms of tube size control. Src42 may have a more centralized role in tube size control given its many potential interactions with other known tube size control factors and functions. The primary contributions to the network from this study are darkened.

Significance and future directions

This work has highlighted important interactions between Src42 and FoxO and the Na⁺/K⁺ ATPase, which all have highly conserved roles in development. Src42 has only briefly and indirectly been suggested as a distant regulator of FoxO and has no prior known interaction with the ATPase to regulate tube size, which is also a testament to the utility of QuBiT to uncover novel molecular interactions. As the mechanisms that facilitate the Src42—FoxO and Src42—ATPase interactions are still under investigation, it would be useful to dissect the functional domains of each of these proteins and quantify their effects, as well as determine the intermediate pathway(s) by which they act. Additionally, as Src42 functions downstream of the Na⁺/K⁺ ATPase, it is likely that Src42 is epistatic to many other SJ components, and would be a logical intermediate to, for example, the Sinuous/Kune—Serp/Verm pathway. If this is the case, the specificity of Src42 actions in response to its upstream interaction partners would need to be explored.

Another unusual molecular interaction in tube size control involves Crumbs, an apical polarity determinant that has been shown to cause tube elongation despite being internally localized to Vps32 retromers at embryonic stages (Dong et al., 2014) and

Vps35 retromers at larval stages (Skouloudaki et al., 2019) in flies. The consistency in these observations has raised questions about the mechanism by which Crb influences tube size. The unrolling module of QuBiT offers the extensibility to model conical tubes as 3D planar cell sheets simply by stacking each unrolled image at increasing radii as a traditional image stack. When paired with live imaging data, this would be a tremendous asset in understanding the function of Crb by tracking its movement to and from the apical surface. As Crb also has many highly conserved functions in other species, it is likely that the findings will assist in understanding the conserved mechanisms of Crb or highlight key differences in which this apical component functions differently from others, as hinted by the differential localization of Uif and Crb in the fly hindgut.

The aforementioned results and future prospects would not have been possible without QuBiT. As the field of computational biology grows to address questions that neither computer science nor biology alone can answer, it is important that our computational tools remain extensible and adaptable. As QuBiT itself does not make any assumptions such as the size, shape, or network of the tubular system it is working on, it can easily be adapted for use in other fields, such as the more complex vascular systems in mammals, which greatly benefits future work involving highly conserved proteins that will be investigated in different model systems.

In addition to cellular level analysis, QuBiT also has the potential to aid in understanding of tissue level and higher order mechanics. Further improvements on computational modeling, including models of individual cell surfaces and their response to changing aECM parameters such as flow and molecular composition, can help to improve our broad understanding of the biomechanical forces that shape each organ. Integration of mechanical forces at these different levels will undoubtedly be essential to translating the effects of signaling molecules to physical forces, which has been poorly understood. An exciting possibility far into the future would be to reverse engineer the biochemical and biophysical conditions of a diseased organ based on observations of the altered characteristics, which would be a tremendous aid to understanding and preventing diseases and pose new biomechanical questions for further study.

References

Abrams, E.W., Cheng, Y.L., Andrew, D.J., 2013. Drosophila KDEL receptor function in the embryonic salivary gland and epidermis. PLoS One 8, e77618.

Affolter, M., Caussinus, E., 2008. Tracheal branching morphogenesis in Drosophila: new insights into cell behaviour and organ architecture. Development 135, 2055-2064.

Alvers, A.L., Ryan, S., Scherz, P.J., Huisken, J., Bagnat, M., 2014. Single continuous lumen formation in the zebrafish gut is mediated by smoothed-dependent tissue remodeling. Development 141, 1110-1119.

Araujo, S.J., Aslam, H., Tear, G., Casanova, J., 2005. mummy/cystic encodes an enzyme required for chitin and glycan synthesis, involved in trachea, embryonic cuticle and CNS development--analysis of its role in Drosophila tracheal morphogenesis. Dev Biol 288, 179-193.

Aspenstrom, P., Richnau, N., Johansson, A.S., 2006. The diaphanous-related formin DAAM1 collaborates with the Rho GTPases RhoA and Cdc42, CIP4 and Src in regulating cell morphogenesis and actin dynamics. Exp Cell Res 312, 2180-2194.

Barbier de Reuille, P., Routier-Kierzkowska, A.L., Kierzkowski, D., Bassel, G.W., Schupbach, T., Tauriello, G., Bajpai, N., Strauss, S., Weber, A., Kiss, A., Burian, A., Hofhuis, H., Sapala, A., Lipowczan, M., Heimlicher, M.B., Robinson, S., Bayer, E.M., Basler, K., Koumoutsakos, P., Roeder, A.H., Aegerter-Wilmsen, T., Nakayama, N., Tsiantis, M., Hay, A., Kwiatkowska, D., Xenarios, I., Kuhlemeier, C., Smith, R.S., 2015. MorphoGraphX: A platform for quantifying morphogenesis in 4D. Elife 4, 05864.

Behr, M., Riedel, D., Schuh, R., 2003. The claudin-like megatrachea is essential in septate junctions for the epithelial barrier function in Drosophila. Dev Cell 5, 611-620.

Behr, M., Wingen, C., Wolf, C., Schuh, R., Hoch, M., 2007. Wurst is essential for airway clearance and respiratory-tube size control. Nat Cell Biol 9, 847-853.

Beitel, G.J., Krasnow, M.A., 2000. Genetic control of epithelial tube size in the Drosophila tracheal system. Development 127, 3271-3282.

Blake, K.J., Myette, G., Jack, J., 1998. The products of ribbon and raw are necessary for proper cell shape and cellular localization of nonmuscle myosin in *Drosophila*. *Dev Biol* 203, 177-188.

Blake, K.J., Myette, G., Jack, J., 1999. ribbon, raw, and zipper have distinct functions in reshaping the *Drosophila* cytoskeleton. *Dev Genes Evol* 209, 555-559.

Blankenship, J.T., Backovic, S.T., Sanny, J.S., Weitz, O., Zallen, J.A., 2006. Multicellular rosette formation links planar cell polarity to tissue morphogenesis. *Dev Cell* 11, 459-470.

Bulow, M.H., Bulow, T.R., Hoch, M., Pankratz, M.J., Junger, M.A., 2014. Src tyrosine kinase signaling antagonizes nuclear localization of FOXO and inhibits its transcription factor activity. *Sci Rep* 4, 4048.

Burgering, B.M., Kops, G.J., 2002. Cell cycle and death control: long live Forkheads. *Trends Biochem Sci* 27, 352-360.

Campos-Ortega, J.A., Hartenstein, V., 1997. The embryonic development of *Drosophila melanogaster*, 2nd ed. Springer, Berlin ; New York.

Chihara, T., Hayashi, S., 2000. Control of tracheal tubulogenesis by Wingless signaling. *Development* 127, 4433-4442.

Chung, S., Vining, M.S., Bradley, P.L., Chan, C.C., Wharton, K.A., Jr., Andrew, D.J., 2009. Serrano (sano) functions with the planar cell polarity genes to control tracheal tube length. *PLoS Genet* 5, e1000746.

Cline, H.E., Dumoulin, C.L., Hart, H.R., Jr., Lorensen, W.E., Ludke, S., 1987. 3D reconstruction of the brain from magnetic resonance images using a connectivity algorithm. *Magn Reson Imaging* 5, 345-352.

Collinet, C., Rauzi, M., Lenne, P.F., Lecuit, T., 2015. Local and tissue-scale forces drive oriented junction growth during tissue extension. *Nat Cell Biol* 17, 1247-1258.

Costa, M., Wilson, E.T., Wieschaus, E., 1994. A putative cell signal encoded by the folded gastrulation gene coordinates cell shape changes during *Drosophila* gastrulation. *Cell* 76, 1075-1089.

Cross, M.J., Claesson-Welsh, L., 2001. FGF and VEGF function in angiogenesis: signalling pathways, biological responses and therapeutic inhibition. *Trends Pharmacol Sci* 22, 201-207.

Cui, X., Xie, Z., 2017. Protein Interaction and Na/K-ATPase-Mediated Signal Transduction. *Molecules* 22.

Devine, W.P., Lubarsky, B., Shaw, K., Luschnig, S., Messina, L., Krasnow, M.A., 2005. Requirement for chitin biosynthesis in epithelial tube morphogenesis. *Proc Natl Acad Sci U S A* 102, 17014-17019.

Dong, B., Hannezo, E., Hayashi, S., 2014. Balance between apical membrane growth and luminal matrix resistance determines epithelial tubule shape. *Cell Rep* 7, 941-950.

Du, L., Zhou, A., Patel, A., Rao, M., Anderson, K., Roy, S., 2017. Unique patterns of organization and migration of FGF-expressing cells during *Drosophila* morphogenesis. *Dev Biol* 427, 35-48.

Dvela-Levitt, M., Cohen-Ben Ami, H., Rosen, H., Ornoy, A., Hochner-Celnikier, D., Granat, M., Lichtstein, D., 2015. Reduction in maternal circulating ouabain impairs offspring growth and kidney development. *J Am Soc Nephrol* 26, 1103-1114.

Fanto, M., McNeill, H., 2004. Planar polarity from flies to vertebrates. *J Cell Sci* 117, 527-533.

Fernandez-Gonzalez, R., Simoes Sde, M., Roper, J.C., Eaton, S., Zallen, J.A., 2009. Myosin II dynamics are regulated by tension in intercalating cells. *Dev Cell* 17, 736-743.

Forster, D., Armbruster, K., Luschnig, S., 2010. Sec24-dependent secretion drives cell-autonomous expansion of tracheal tubes in *Drosophila*. *Curr Biol* 20, 62-68.

Forster, D., Luschnig, S., 2012. Src42A-dependent polarized cell shape changes mediate epithelial tube elongation in *Drosophila*. *Nat Cell Biol* 14, 526-534.

Fritz, R.D., Varga, Z., Radziwill, G., 2010. CNK1 is a novel Akt interaction partner that promotes cell proliferation through the Akt-FoxO signalling axis. *Oncogene* 29, 3575-3582.

Gao, Q., Zhang, J., Wang, X., Liu, Y., He, R., Liu, X., Wang, F., Feng, J., Yang, D., Wang, Z., Meng, A., Yan, X., 2017. The signalling receptor MCAM coordinates apical-basal polarity and planar cell polarity during morphogenesis. *Nat Commun* 8, 15279.

Genova, J.L., Fehon, R.G., 2003. Neuroglian, Gliotactin, and the Na⁺/K⁺ ATPase are essential for septate junction function in *Drosophila*. *J Cell Biol* 161, 979-989.

Ghabrial, A., Luschnig, S., Metzstein, M.M., Krasnow, M.A., 2003. Branching morphogenesis of the *Drosophila* tracheal system. *Annu Rev Cell Dev Biol* 19, 623-647.

Ghabrial, A.S., Krasnow, M.A., 2006. Social interactions among epithelial cells during tracheal branching morphogenesis. *Nature* 441, 746-749.

Grieder, N.C., Caussinus, E., Parker, D.S., Cadigan, K., Affolter, M., Luschnig, S., 2008. gammaCOP is required for apical protein secretion and epithelial morphogenesis in *Drosophila melanogaster*. *PLoS One* 3, e3241.

Hassouna, M.S., Farag, A.A., 2007. Multi-stencils fast marching methods: a highly accurate solution to the eikonal equation on cartesian domains. *IEEE Trans Pattern Anal Mach Intell* 29, 1563-1574.

Heisenberg, C.P., Tada, M., Rauch, G.J., Saude, L., Concha, M.L., Geisler, R., Stemple, D.L., Smith, J.C., Wilson, S.W., 2000. Silberblick/Wnt11 mediates convergent extension movements during zebrafish gastrulation. *Nature* 405, 76-81.

Henderson, K.D., Andrew, D.J., 2000. Regulation and function of Scr, exd, and hth in the *Drosophila* salivary gland. *Dev Biol* 217, 362-374.

Hughes, J., Ward, C.J., Peral, B., Aspinwall, R., Clark, K., San Millan, J.L., Gamble, V., Harris, P.C., 1995. The polycystic kidney disease 1 (PKD1) gene encodes a novel protein with multiple cell recognition domains. *Nat Genet* 10, 151-160.

Irvine, K.D., Wieschaus, E., 1994. Cell intercalation during *Drosophila* germband extension and its regulation by pair-rule segmentation genes. *Development* 120, 827-841.

Isaac, D.D., Andrew, D.J., 1996. Tubulogenesis in *Drosophila*: a requirement for the tracheless gene product. *Genes Dev* 10, 103-117.

Iwaki, D.D., Johansen, K.A., Singer, J.B., Lengyel, J.A., 2001. *drumstick*, *bowl*, and *lines* are required for patterning and cell rearrangement in the *Drosophila* embryonic hindgut. *Dev Biol* 240, 611-626.

Jiang, L., Crews, S.T., 2007. Transcriptional specificity of *Drosophila* *dysfusion* and the control of tracheal fusion cell gene expression. *J Biol Chem* 282, 28659-28668.

Kakihara, K., Shinmyozu, K., Kato, K., Wada, H., Hayashi, S., 2008. Conversion of plasma membrane topology during epithelial tube connection requires Arf-like 3 small GTPase in *Drosophila*. *Mech Dev* 125, 325-336.

Kato, K., Chihara, T., Hayashi, S., 2004. Hedgehog and Decapentaplegic instruct polarized growth of cell extensions in the *Drosophila* trachea. *Development* 131, 5253-5261.

Kato, K., Dong, B., Wada, H., Tanaka-Matakatsu, M., Yagi, Y., Hayashi, S., 2016. Microtubule-dependent balanced cell contraction and luminal-matrix modification accelerate epithelial tube fusion. *Nat Commun* 7, 11141.

Kayal, R.A., Siqueira, M., Alblowi, J., McLean, J., Krothapalli, N., Faibish, D., Einhorn, T.A., Gerstenfeld, L.C., Graves, D.T., 2010. TNF-alpha mediates diabetes-enhanced chondrocyte apoptosis during fracture healing and stimulates chondrocyte apoptosis through FOXO1. *J Bone Miner Res* 25, 1604-1615.

Keller, R., Shih, J., Sater, A.K., Moreno, C., 1992. Planar induction of convergence and extension of the neural plate by the organizer of *Xenopus*. *Dev Dyn* 193, 218-234.

Khan, Z., Wang, Y.C., Wieschaus, E.F., Kaschube, M., 2014. Quantitative 4D analyses of epithelial folding during *Drosophila* gastrulation. *Development* 141, 2895-2900.

Kim, D.J., Norden, P.R., Salvador, J., Barry, D.M., Bowers, S.L.K., Cleaver, O., Davis, G.E., 2017. Src- and Fyn-dependent apical membrane trafficking events control endothelial lumen formation during vascular tube morphogenesis. *PLoS One* 12, e0184461.

Kondo, T., Hashimoto, Y., Kato, K., Inagaki, S., Hayashi, S., Kageyama, Y., 2007. Small peptide regulators of actin-based cell morphogenesis encoded by a polycistronic mRNA. *Nat Cell Biol* 9, 660-665.

Kondo, T., Hayashi, S., 2013. Mitotic cell rounding accelerates epithelial invagination. *Nature* 494, 125-129.

Kreshuk, A., Straehle, C.N., Sommer, C., Koethe, U., Cantoni, M., Knott, G., Hamprecht, F.A., 2011. Automated detection and segmentation of synaptic contacts in nearly isotropic serial electron microscopy images. *PLoS One* 6, e24899.

Kumichel, A., Knust, E., 2014. Apical localisation of crumbs in the boundary cells of the *Drosophila* hindgut is independent of its canonical interaction partner stardust. *PLoS One* 9, e94038.

Laberge, G., Douziech, M., Therrien, M., 2005. Src42 binding activity regulates *Drosophila* RAF by a novel CNK-dependent derepression mechanism. *EMBO J* 24, 487-498.

Lai, F., Madan, N., Ye, Q., Duan, Q., Li, Z., Wang, S., Si, S., Xie, Z., 2013. Identification of a mutant alpha1 Na/K-ATPase that pumps but is defective in signal transduction. *J Biol Chem* 288, 13295-13304.

Laprise, P., Beronja, S., Silva-Gagliardi, N.F., Pellikka, M., Jensen, A.M., McGlade, C.J., Tepass, U., 2006. The FERM protein Yurt is a negative regulatory component of the

Crumbs complex that controls epithelial polarity and apical membrane size. *Dev Cell* 11, 363-374.

Laprise, P., Lau, K.M., Harris, K.P., Silva-Gagliardi, N.F., Paul, S.M., Beronja, S., Beitel, G.J., McGlade, C.J., Tepass, U., 2009. Yurt, Coracle, Neurexin IV and the Na(+),K(+)-ATPase form a novel group of epithelial polarity proteins. *Nature* 459, 1141-1145.

Laprise, P., Paul, S.M., Boulanger, J., Robbins, R.M., Beitel, G.J., Tepass, U., 2010. Epithelial polarity proteins regulate *Drosophila* tracheal tube size in parallel to the luminal matrix pathway. *Curr Biol* 20, 55-61.

Lebreton, G., Casanova, J., 2014. Specification of leading and trailing cell features during collective migration in the *Drosophila* trachea. *J Cell Sci* 127, 465-474.

Letizia, A., Sotillos, S., Campuzano, S., Llimargas, M., 2011. Regulated Crb accumulation controls apical constriction and invagination in *Drosophila* tracheal cells. *J Cell Sci* 124, 240-251.

Li, D., D'Angelo, L., Chavez, M., Woulfe, D.S., 2011. Arrestin-2 differentially regulates PAR4 and ADP receptor signaling in platelets. *J Biol Chem* 286, 3805-3814.

Lienkamp, S.S., Liu, K., Karner, C.M., Carroll, T.J., Ronneberger, O., Wallingford, J.B., Walz, G., 2012. Vertebrate kidney tubules elongate using a planar cell polarity-dependent, rosette-based mechanism of convergent extension. *Nat Genet* 44, 1382-1387.

Llimargas, M., 2000. Wingless and its signalling pathway have common and separable functions during tracheal development. *Development* 127, 4407-4417.

Lu, Q., Zhai, Y., Cheng, Q., Liu, Y., Gao, X., Zhang, T., Wei, Y., Zhang, F., Yin, X., 2013. The Akt-FoxO3a-manganese superoxide dismutase pathway is involved in the regulation of oxidative stress in diabetic nephropathy. *Exp Physiol* 98, 934-945.

Luschnig, S., Batz, T., Armbruster, K., Krasnow, M.A., 2006. serpentine and vermiform encode matrix proteins with chitin binding and deacetylation domains that limit tracheal tube length in *Drosophila*. *Curr Biol* 16, 186-194.

Manning, G.K., M.A., 1993. Development of the *Drosophila* tracheal system. Bate, Martinez Arias.

Martins, R., Lithgow, G.J., Link, W., 2016. Long live FOXO: unraveling the role of FOXO proteins in aging and longevity. *Aging Cell* 15, 196-207.

Marx, M., Warren, S.L., Madri, J.A., 2001. pp60(c-src) modulates microvascular endothelial phenotype and in vitro angiogenesis. *Exp Mol Pathol* 70, 201-213.

Matusek, T., Djiane, A., Jankovics, F., Brunner, D., Mlodzik, M., Mihaly, J., 2006. The *Drosophila* formin DAAM regulates the tracheal cuticle pattern through organizing the actin cytoskeleton. *Development* 133, 957-966.

Miao, G., Hayashi, S., 2016. Escargot controls the sequential specification of two tracheal tip cell types by suppressing FGF signaling in *Drosophila*. *Development* 143, 4261-4271.

Morize, P., Christiansen, A.E., Costa, M., Parks, S., Wieschaus, E., 1998. Hyperactivation of the folded gastrulation pathway induces specific cell shape changes. *Development* 125, 589-597.

Moussian, B., Schwarz, H., Bartoszewski, S., Nusslein-Volhard, C., 2005. Involvement of chitin in exoskeleton morphogenesis in *Drosophila melanogaster*. *J Morphol* 264, 117-130.

Munjal, A., Philippe, J.M., Munro, E., Lecuit, T., 2015. A self-organized biomechanical network drives shape changes during tissue morphogenesis. *Nature* 524, 351-355.

Myat, M.M., Andrew, D.J., 2002. Epithelial tube morphology is determined by the polarized growth and delivery of apical membrane. *Cell* 111, 879-891.

Navis, A., Bagnat, M., 2015. Loss of cfr function leads to pancreatic destruction in larval zebrafish. *Dev Biol* 399, 237-248.

Nelson, K.S., Furuse, M., Beitel, G.J., 2010. The *Drosophila* Claudin Kune-kune is required for septate junction organization and tracheal tube size control. *Genetics* 185, 831-839.

Nelson, K.S., Khan, Z., Molnar, I., Mihaly, J., Kaschube, M., Beitel, G.J., 2012. *Drosophila* Src regulates anisotropic apical surface growth to control epithelial tube size. *Nat Cell Biol* 14, 518-525.

Nikolopoulou, E., Galea, G.L., Rolo, A., Greene, N.D., Copp, A.J., 2017. Neural tube closure: cellular, molecular and biomechanical mechanisms. *Development* 144, 552-566.

Nishimura, M., Inoue, Y., Hayashi, S., 2007. A wave of EGFR signaling determines cell alignment and intercalation in the *Drosophila* tracheal placode. *Development* 134, 4273-4282.

Norum, M., Tang, E., Chavoshi, T., Schwarz, H., Linke, D., Uv, A., Moussian, B., 2010. Trafficking through COPII stabilises cell polarity and drives secretion during *Drosophila* epidermal differentiation. *PLoS One* 5, e10802.

Ohshiro, T., Emori, Y., Saigo, K., 2002. Ligand-dependent activation of breathless FGF receptor gene in *Drosophila* developing trachea. *Mech Dev* 114, 3-11.

Olivares-Castineira, I., Llimargas, M., 2017. EGFR controls *Drosophila* tracheal tube elongation by intracellular trafficking regulation. *PLoS Genet* 13, e1006882.

Ossipova, O., Kim, K., Lake, B.B., Itoh, K., Ioannou, A., Sokol, S.Y., 2014. Role of Rab11 in planar cell polarity and apical constriction during vertebrate neural tube closure. *Nat Commun* 5, 3734.

Ouko, L., Ziegler, T.R., Gu, L.H., Eisenberg, L.M., Yang, V.W., 2004. Wnt11 signaling promotes proliferation, transformation, and migration of IEC6 intestinal epithelial cells. *J Biol Chem* 279, 26707-26715.

Ozturk-Colak, A., Moussian, B., Araujo, S.J., Casanova, J., 2016. A feedback mechanism converts individual cell features into a supracellular ECM structure in *Drosophila* trachea. *Elife* 5.

Pare, A.C., Vichas, A., Fincher, C.T., Mirman, Z., Farrell, D.L., Mainieri, A., Zallen, J.A., 2014. A positional Toll receptor code directs convergent extension in *Drosophila*. *Nature* 515, 523-527.

Paul, S.M., Beitel, G.J., 2003. Developmental biology. Tubulogenesis CLICs into place. *Science* 302, 2077-2078.

Paul, S.M., Palladino, M.J., Beitel, G.J., 2007. A pump-independent function of the Na,K-ATPase is required for epithelial junction function and tracheal tube-size control. *Development* 134, 147-155.

Paul, S.M., Ternet, M., Salvaterra, P.M., Beitel, G.J., 2003. The Na⁺/K⁺ ATPase is required for septate junction function and epithelial tube-size control in the *Drosophila* tracheal system. *Development* 130, 4963-4974.

Pedraza, L.G., Stewart, R.A., Li, D.M., Xu, T., 2004. *Drosophila* Src-family kinases function with Csk to regulate cell proliferation and apoptosis. *Oncogene* 23, 4754-4762.

Pirraglia, C., Walters, J., Myat, M.M., 2010. Pak1 control of E-cadherin endocytosis regulates salivary gland lumen size and shape. *Development* 137, 4177-4189.

Poon, C.L.C., Brumby, A.M., Richardson, H.E., 2018. Src Cooperates with Oncogenic Ras in Tumorigenesis via the JNK and PI3K Pathways in *Drosophila* epithelial Tissue. *Int J Mol Sci* 19.

Robbins, R.M., Gbur, S.C., Beitel, G.J., 2014. Non-canonical roles for Yorkie and *Drosophila* Inhibitor of Apoptosis 1 in epithelial tube size control. *PLoS One* 9, e101609.

Roukens, M.G., Alloul-Ramdhani, M., Baan, B., Kobayashi, K., Peterson-Maduro, J., van Dam, H., Schulte-Merker, S., Baker, D.A., 2010. Control of endothelial sprouting by a Tel-CtBP complex. *Nat Cell Biol* 12, 933-942.

Samakovlis, C., Hacohen, N., Manning, G., Sutherland, D.C., Guillemin, K., Krasnow, M.A., 1996. Development of the *Drosophila* tracheal system occurs by a series of morphologically distinct but genetically coupled branching events. *Development* 122, 1395-1407.

Sepich, D.S., Myers, D.C., Short, R., Topczewski, J., Marlow, F., Solnica-Krezel, L., 2000. Role of the zebrafish trilobite locus in gastrulation movements of convergence and extension. *Genesis* 27, 159-173.

Simoes Sde, M., Mainieri, A., Zallen, J.A., 2014. Rho GTPase and Shroom direct planar polarized actomyosin contractility during convergent extension. *J Cell Biol* 204, 575-589.

Singer, J.B., Harbecke, R., Kusch, T., Reuter, R., Lengyel, J.A., 1996. *Drosophila* brachyenteron regulates gene activity and morphogenesis in the gut. *Development* 122, 3707-3718.

Sinha, T., Lin, L., Li, D., Davis, J., Evans, S., Wynshaw-Boris, A., Wang, J., 2015. Mapping the dynamic expression of Wnt11 and the lineage contribution of Wnt11-expressing cells during early mouse development. *Dev Biol* 398, 177-192.

Skou, J.C., Esmann, M., 1992. The Na,K-ATPase. *J Bioenerg Biomembr* 24, 249-261.

Skouloudaki, K., Papadopoulos, D.K., Tomancak, P., Knust, E., 2019. The apical protein Apnoia interacts with Crumbs to regulate tracheal growth and inflation. *PLoS Genet* 15, e1007852.

Smith, J.L., Schoenwolf, G.C., 1989. Notochordal induction of cell wedging in the chick neural plate and its role in neural tube formation. *J Exp Zool* 250, 49-62.

Sollier, K., Gaude, H.M., Chartier, F.J., Laprise, P., 2015. Rac1 controls epithelial tube length through the apical secretion and polarity pathways. *Biol Open* 5, 49-54.

Somogyi, K., Rorth, P., 2004. Cortactin modulates cell migration and ring canal morphogenesis during *Drosophila* oogenesis. *Mech Dev* 121, 57-64.

Sun, Y., Zhang, D., Guo, X., Li, W., Li, C., Luo, J., Zhou, M., Xue, L., 2019. MKK3 modulates JNK-dependent cell migration and invasion. *Cell Death Dis* 10, 149.

Sutherland, D., Samakovlis, C., Krasnow, M.A., 1996. *branchless* encodes a Drosophila FGF homolog that controls tracheal cell migration and the pattern of branching. *Cell* 87, 1091-1101.

Syed, Z.A., Bouge, A.L., Byri, S., Chavoshi, T.M., Tang, E., Bouhin, H., van Dijk-Hard, I.F., Uv, A., 2012. A luminal glycoprotein drives dose-dependent diameter expansion of the *Drosophila melanogaster* hindgut tube. *PLoS Genet* 8, e1002850.

Tada, M., Heisenberg, C.P., 2012. Convergent extension: using collective cell migration and cell intercalation to shape embryos. *Development* 139, 3897-3904.

Tanaka-Matakatsu, M., Uemura, T., Oda, H., Takeichi, M., Hayashi, S., 1996. Cadherin-mediated cell adhesion and cell motility in *Drosophila* trachea regulated by the transcription factor *Escargot*. *Development* 122, 3697-3705.

Tonning, A., Hemphala, J., Tang, E., Nannmark, U., Samakovlis, C., Uv, A., 2005. A transient luminal chitinous matrix is required to model epithelial tube diameter in the *Drosophila* trachea. *Dev Cell* 9, 423-430.

Torres, V.E., Harris, P.C., Pirson, Y., 2007. Autosomal dominant polycystic kidney disease. *Lancet* 369, 1287-1301.

Tsarouhas, V., Senti, K.A., Jayaram, S.A., Tiklova, K., Hemphala, J., Adler, J., Samakovlis, C., 2007. Sequential pulses of apical epithelial secretion and endocytosis drive airway maturation in *Drosophila*. *Dev Cell* 13, 214-225.

Wang, S., Jayaram, S.A., Hemphala, J., Senti, K.A., Tsarouhas, V., Jin, H., Samakovlis, C., 2006. Septate-junction-dependent luminal deposition of chitin deacetylases restricts tube elongation in the *Drosophila* trachea. *Curr Biol* 16, 180-185.

Werdich, X.Q., Penn, J.S., 2005. *Src*, *Fyn* and *Yes* play differential roles in VEGF-mediated endothelial cell events. *Angiogenesis* 8, 315-326.

Wilk, R., Weizman, I., Shilo, B.Z., 1996. *trachealess* encodes a bHLH-PAS protein that is an inducer of tracheal cell fates in *Drosophila*. *Genes Dev* 10, 93-102.

Wodarz, A., Hinz, U., Engelbert, M., Knust, E., 1995. Expression of crumbs confers apical character on plasma membrane domains of ectodermal epithelia of *Drosophila*. *Cell* 82, 67-76.

Wu, V.M., Schulte, J., Hirschi, A., Tepass, U., Beitel, G.J., 2004. Sinuous is a *Drosophila* claudin required for septate junction organization and epithelial tube size control. *J Cell Biol* 164, 313-323.

Xu, N., Bagumian, G., Galiano, M., Myat, M.M., 2011. Rho GTPase controls *Drosophila* salivary gland lumen size through regulation of the actin cytoskeleton and Moesin. *Development* 138, 5415-5427.

Yamamura, Y., Lee, W.L., Inoue, K., Ida, H., Ito, Y., 2006. RUNX3 cooperates with FoxO3a to induce apoptosis in gastric cancer cells. *J Biol Chem* 281, 5267-5276.

Yang, P., Li, X., Xu, C., Eckert, R.L., Reece, E.A., Zielke, H.R., Wang, F., 2013. Maternal hyperglycemia activates an ASK1-FoxO3a-caspase 8 pathway that leads to embryonic neural tube defects. *Sci Signal* 6, ra74.

Yoo, S.Y., Kwon, S.M., 2013. Angiogenesis and its therapeutic opportunities. *Mediators Inflamm* 2013, 127170.

Zallen, J.A., Wieschaus, E., 2004. Patterned gene expression directs bipolar planar polarity in *Drosophila*. *Dev Cell* 6, 343-355.

Zhang, L., Ward, R.E.t., 2009. uninflatable encodes a novel ectodermal apical surface protein required for tracheal inflation in *Drosophila*. *Dev Biol* 336, 201-212.

Appendix

Validation of QuBiT functions and methods in other tubular systems: the hindgut and salivary gland

To demonstrate that QuBiT can analyze tubes of different sizes, shapes, and architectures, I examined the *Drosophila* embryonic stage 16 hindgut (partial max projection in Fig. A.1A; 3D reconstruction in Fig. A.1A'), which consists of a monolayer of cells like the trachea but can have a larger diameter (up to 14 μm and 18 cells per cross-section vs 5 μm and 4 cells respectively). As with the trachea, I observed banding of Uif (Fig. A.1B, yellow arrowheads), which is also visible in the tube cross-section (Fig. A.1B', yellow arrowheads). However, unlike the trachea, the intensity of the banding varied strongly along the tube length. In addition to the banding, the unrolled projection revealed two narrow stripes of missing Uif (white arrowheads in Fig. A.1B-D) that coincide with boundary cells (red boxes in Fig. A.1B-D, A.1D inset). The absence of Uif in boundary cells is unexpected given that boundary cells show elevated levels of the apical marker Crumbs (Kumichel and Knust, 2014). Thus, QuBiT can analyze both small

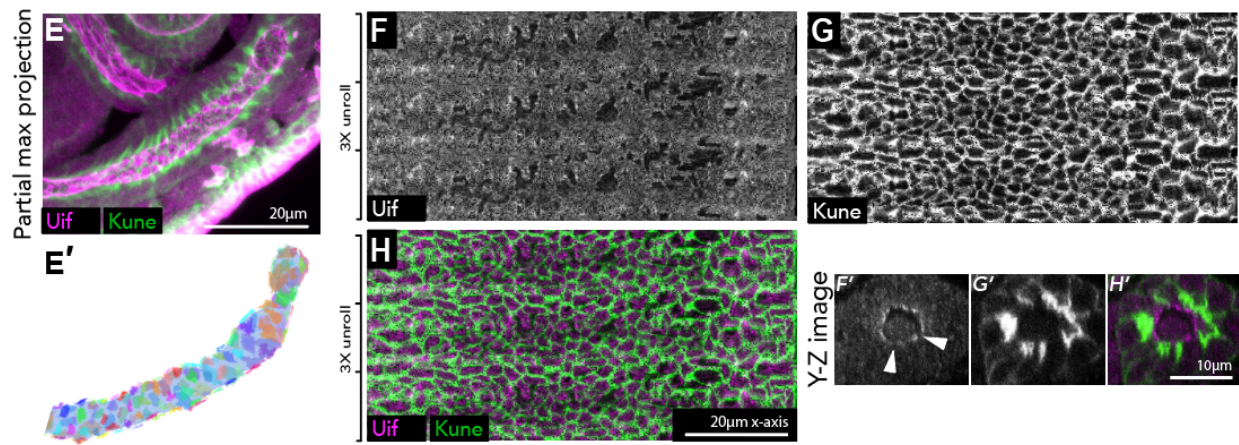
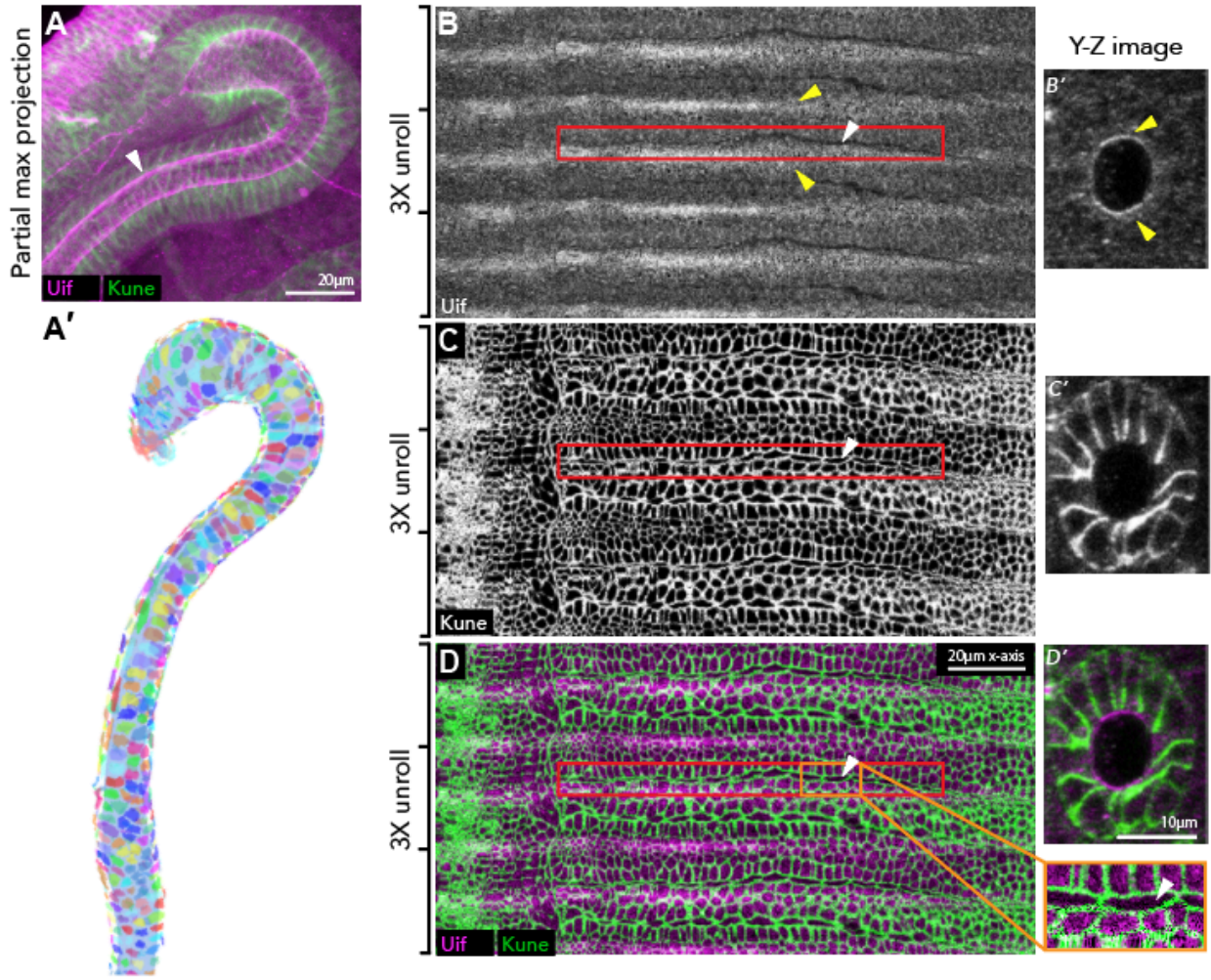


Fig. A.1 (on previous page): Processing of other tubes in the fly embryo. (A-D) Wildtype hindgut (w^{1118}). (A) Partial projection view. White arrowhead points to boundary cells, which span the length of the hindgut. (A') 3D reconstruction. Apical cell surfaces are individually colored and slightly elevated to show the underlying tube surface (translucent blue). (B) Unrolled Uif channel, repeated three times. Left is anterior. Yellow arrowheads indicate bands of increased Uif. The red box encloses boundary cells and is located in the same relative position in subsequent images. White arrowhead denotes boundary cells, which are located in the same positions in C and D and coincide with the stripes of reduced Uif. (B') Sample cross-section. Yellow arrowheads indicate regions of elevated Uif. (C,C') Unrolled Kune channel and cross-section. (D,D') Merged channels. Orange-framed inset shows a magnification of the boundary cells that, unlike the adjoining cells, do not express Uif. (E-H) WT salivary gland (w^{1118}). Color schemes are the same as for the corresponding panels in A-D. (E) Partial projection view. (E') 3D reconstruction. (F-H) Unrolled Uif (F), Kune (G), and merged channels (H), repeated three times for clarity. (F'-H') Corresponding representative cross-sections.

and larger diameter tubes, and the use of QuBiT again revealed unexpected expression patterns of an apical marker.

To test the ability of QuBiT to process low-quality data such as might be present in mutant or diseased tissue, I analyzed the *Drosophila* salivary gland (partial max projection in Fig. A.1E; 3D reconstruction in Fig. A.1E'). Uif staining of the salivary gland

apical surface is more sparse and patchy (Fig. A.1F) than in the trachea, with significant sections of the circumference nearing background levels of Uif (Fig. A.1F', white arrowheads), but QuBiT is nonetheless able to render the apical surface and junctions (Fig. A.1G). Thus, QuBiT can process sub-optimal image data that either has poor or incomplete signal.

Cell structures in the DT are similar to those seen in known cell rearrangement paradigms

As an example of the post-processing compatibility of QuBiT, I mapped the unrolled cells of wildtype tubes using a Voronoi diagram, which uses the centers of cells to create cell boundaries and predict neighbors. Preliminary analysis of the Voronoi diagrams in wildtype embryos revealed cell structures that resembled previously identified motifs: rosettes and T1-T2-T3 transitions (Fig. A.2). Although it is uncertain whether these motifs exist on a highly curved surface such as the trachea, it would nevertheless be in agreement with cell rearrangement events that have been postulated to occur during tracheal expansion.

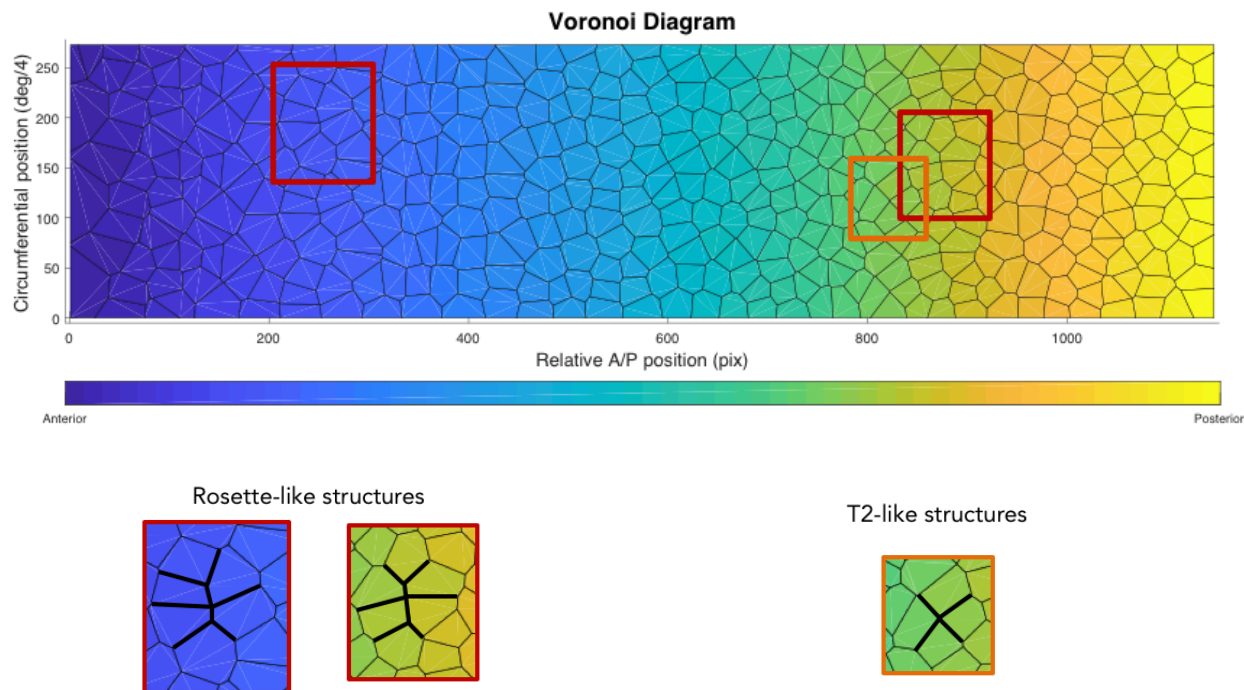


Fig. A.2: Voronoi diagram of a w^{1118} unrolled embryo. Unlike the watershed algorithm, a Voronoi diagram uses straight lines to draw cell junctions, which results in nearly identical cell neighbors, but also predicts higher order structures such as rosettes and T1-T2-T3 transitions. Examples in the sample diagram are outlined in dark red and dark orange respectively.

Preliminary analyses of Crumbs in tube size control

Both this and previous work (Tepass et al., 1990; Laprise et al., 2006; Laprise et al., 2010; Dong et al., 2014; Olivares-Castiñeira and Llimargas, 2017) has suggested the importance of Crumbs (Crb), an apical determinant and intracellular signaling molecule

(Fig. A.3A), in regulating tracheal development. Increased expression of Crb is sufficient to drive tracheal elongation and vice versa, though it is unclear why removal of Crb from the apical cell domain to cytosolic vesicles results in an increase of apical surface area (Fig. A.4). While Crb is proposed to have a mechanism of action via the Hippo network (Fig. A.3B) (Ling et al., 2010; Chen et al., 2010; Ribiero et al., 2014; McSharry and Beitel, 2019), the functional domain(s) within Crb that confer its tube size control function have not been explored and the intracellular localization necessary for Crb to carry out this function are under dispute.

To test the functional domains and localization of Crb that are necessary to regulate tube size, I created Crb constructs with modified protein domains (Fig. A.5). The original “Crb-intra” construct that was shown to be sufficient to confer apical character and rescue Crb loss-of-function mutants (Wodarz et al., 1995) was recreated and served as the basis of the remaining constructs. To truly isolate the tube size function to the intracellular domain (ICD), I created a true “Crb-intra” by removing the entire extracellular domain (ECD) and replacing the transmembrane domain (TMD) with a myristoylation tag. I also systematically substituted other domains, such as by replacing the Crb TMD with a Sevenless (Sev) TMD and the Crb 3’UTR with that of a ubiquitous

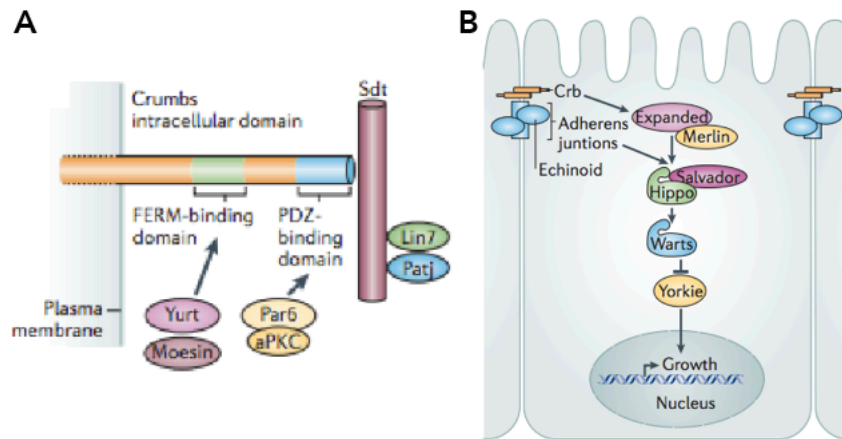


Fig. A.3: A basic overview of Crb and its potential target, the Hippo network, for regulating tube size. (A) Most of the polarity function of Crb is in its short 37-amino acid intracellular domain, which contains FERM- and PDZ-binding domains that interact with other known apical polarity factors including PAR6, aPKC, and Stardust (Sdt). (B) Although Crb localizes to the apical surface, its mechanism of action likely requires signal transduction to the nucleus via the Hippo network, where it promotes transcription of additional growth factors. Adapted from Thompson et al., 2013.

ribosomal protein, RpL29. Finally, I moved the ECD myc tag that was initially used to track the Wodarz et al., 1995 Crb construct to the ICD to create distance between the remaining Crb ICD and the apical cell surface.

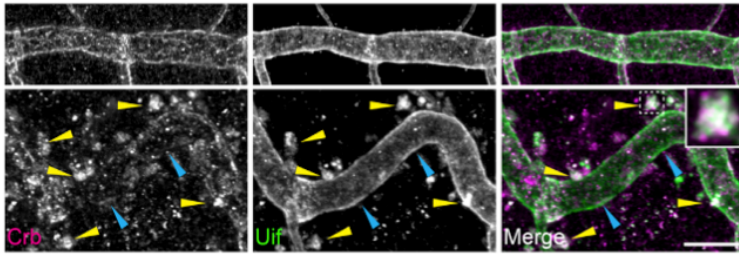


Fig. A.4: Mislocalization of Crb in the shrub mutant causes tube elongation. Despite Crb conferring apical character, tube expansion occurs while Crb occupies vesicles in the cytosol. Removal of a single copy of Crb is sufficient to restore the tracheal length defect of the shrub mutant, suggesting shrub and Crb function in the same pathway. From Dong et al., 2014.

Preliminary analysis of these Crb constructs driven in the trachea show that most of them increase tube length as expected (Fig. A.5B), suggesting that the TMD, myc tag location, and the 3'UTR did not affect the tube size control function of Crb. The outlier was the myristoylated Crb ICD, which had no significant effect compared to the trachea-specific driver alone. As I had no traceable marker for this construct, I was unable to verify whether myr-Crb localized to the apical surface. Additional constructs were created with myc-tagged myr-Crb, but they were not analyzed. Quantification of tube cross-sections (Fig. A.6) showed that all of the Crb constructs, including myr-Crb, had similar area and perimeter profiles along the tube axis. These results are in agreement

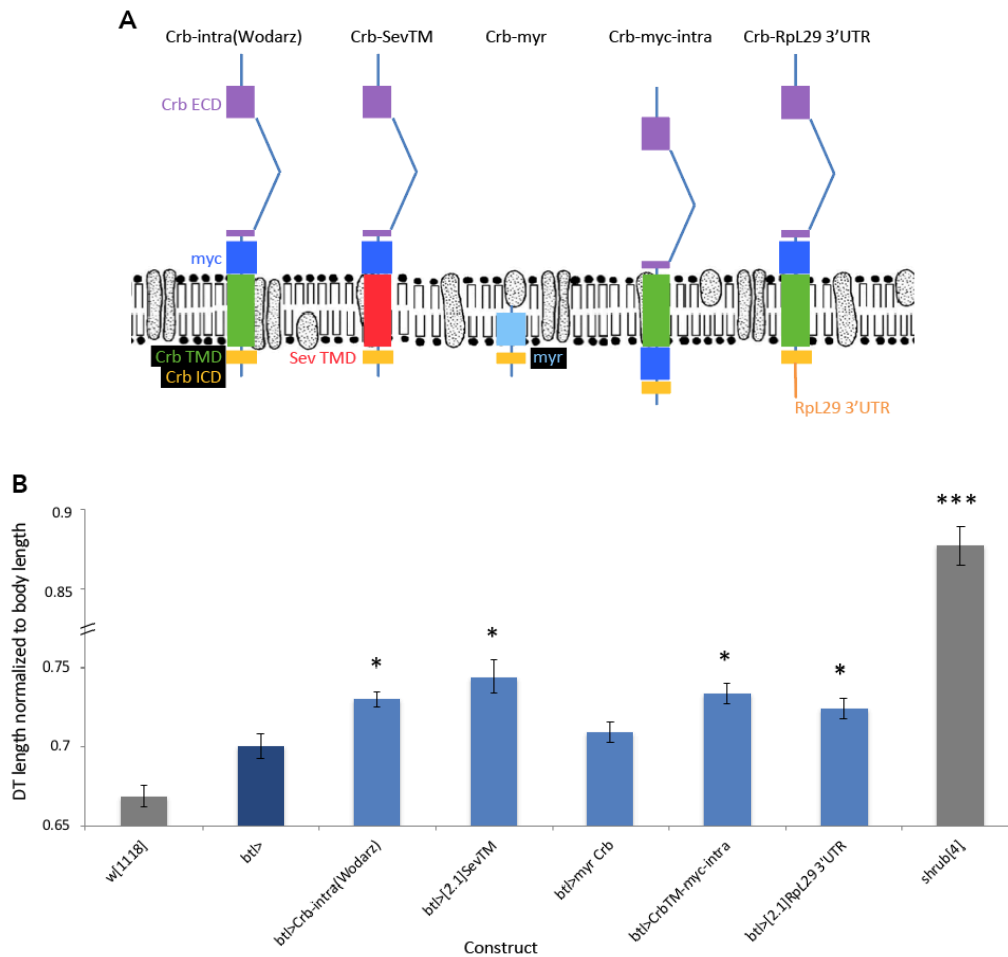


Fig. A.5: Crb constructs and tube length measurements ($n = 6$ tubes each except for shrub, where $n = 3$ tubes). (A) The reconstruction of “Crb-intra” used in (Wodarz et al., 1995) was used as the basis for the remaining constructs. Various domains of Crb were systematically replaced to isolate the source of its tube length regulation. A myristoylation tagged Crb ICD represents the “true” Crb-intra. ECD = extracellular domain; TMD = transmembrane domain; ICD = intracellular domain; myc = myc tag; myr = myristoylation tag. (B) Preliminary measurements of DT length normalized to whole embryo length. The trachea-specific driver *breathless* (*btl*) alone is slightly longer than wildtype. All comparisons were done relative to the *btl* driver. * = $p < 0.05$; *** = $p < 10^{-3}$.

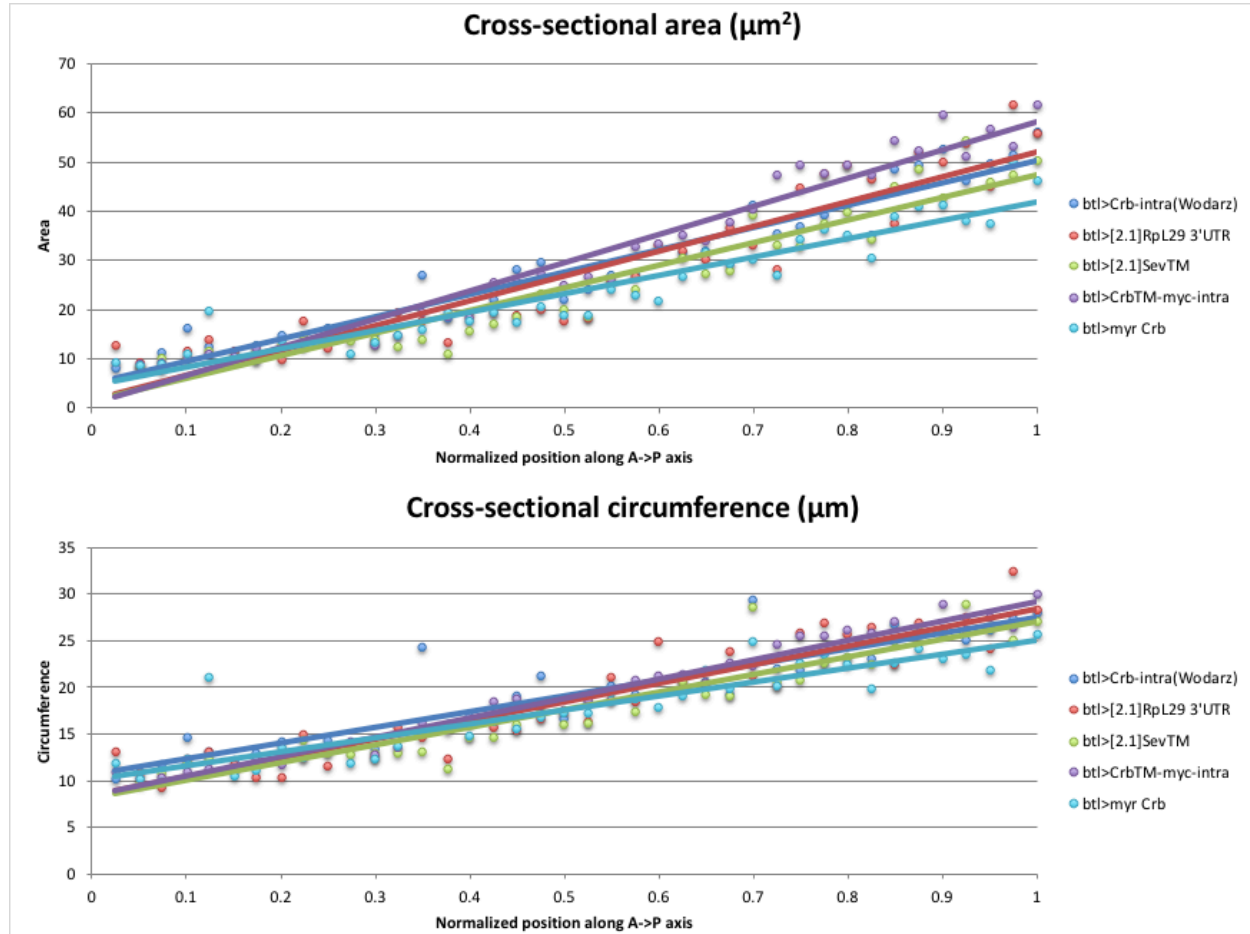


Fig. A.6: Crb tube cross-section measurements. 40 equally spaced cross-sections along the length of the DT were used. Average values for each construct were plotted and lines of best fit were overlaid. As for tube length, the cross-sectional areas and circumferences of most Crb constructs were similar.

with other work that the Crb ICD plays an important role in tube size control, and additional work is required to dissect the signaling domain(s) and their downstream components and mechanisms that allow Crb to perform its tube size control function.

Laser ablation experiments suggest the trachea is under tension during early development, but not as the tube grows

In order to understand the mechanical forces that present on the trachea that may enforce and/or restrict tube and cell geometries, I performed laser ablation experiments on stage 14 and 16 wildtype tubes and measured the retraction of severed tracheal segments and their neighbors. Preliminary analysis of stage 14 tubes that were entirely severed at a single point on the DT showed retraction as measured by distance between two landmarks (Fig. A.7A). However, neighboring segments were unaffected, which suggests that the tension in the DT at stage 14 is localized within each segment rather than on the entire length of the DT. The tension disappears after the tube inflates and elongates (stage 16, Fig. A.7B), in agreement with the tube's transition from a taut appearance to a wavy one. Ablation of individual cell junctions at this stage also had no effect on the DT (Fig. A.7C). These results imply that inflation and/or elongation of the trachea counteracts the tension forces present in early stages such that DT cells are "relaxed" on the tube surface by stage 16 and supports the model of cell shape changes being dependent on underlying tube shape changes (see main text).

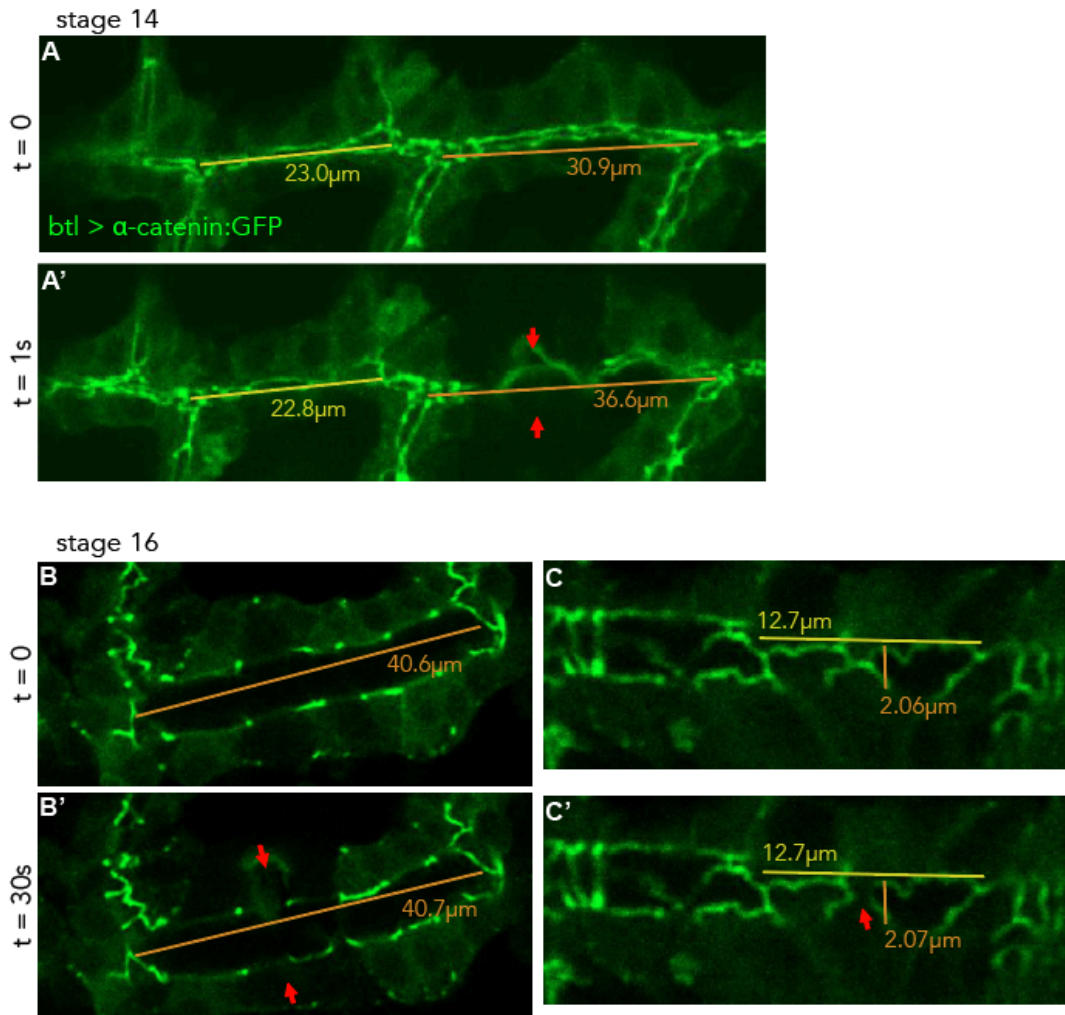


Fig. A.7: Laser ablation of wildtype trachea suggests the DT is under tension early in development. Red arrows indicate location of laser ablation. Yellow and orange lines and measurements indicate length. (A,A') A stage 14 embryo. Ablation causes the local DT to retract (orange line), but not nearby segments (yellow line) suggesting each individual segment is under its own tension forces. (B,B') A stage 16 embryo. Ablation across the entire DT does not change the measured distance between landmarks. (C,C') Another stage 16 embryo. Ablation of individual cell junctions has no effect on either tube length or width as measured by distance between landmarks.